Fall 1-11-2018

Development of a Design Guideline for Bridge Pile Foundations Subjected to Liquefaction Induced Lateral Spreading

Jonathan A. Nasr
Portland State University

Recommended Citation

Nasr, Jonathan A., "Development of a Design Guideline for Bridge Pile Foundations Subjected to Liquefaction Induced Lateral Spreading" (2018). *Dissertations and Theses.* Paper 4160.
https://doi.org/10.15760/etd.6048

Development of a Design Guideline for Bridge Pile Foundations Subjected to Liquefaction Induced Lateral Spreading

by

Jonathan A. Nasr

A thesis submitted in partial fulfillment of the
requirements for the degree of

Master of Science
in
Civil and Environmental Engineering

Thesis Committee:
Arash Khosravifar, Chair
Franz Rad
Thomas Schumacher

Portland State University
2017

ABSTRACT

Effective-stress nonlinear dynamic analyses (NDA) were performed for piles in liquefiable sloped ground to assess how inertia and liquefaction-induced lateral spreading combine in long-duration vs. short-duration earthquakes. A parametric study was performed using input motions from subduction and crustal earthquakes covering a wide range of earthquake durations. The NDA results were used to evaluate the accuracy of the equivalent static analysis (ESA) recommended by Caltrans/ODOT for estimating pile demands. Finally, the NDA results were used to develop new ESA methods to combine inertial and lateral spreading loads for estimating elastic and inelastic pile demands.

The NDA results showed that pile demands increase in liquefied conditions compared to nonliquefied conditions due to the interaction of inertia (from superstructure) and kinematics (from liquefaction-induced lateral spreading). Comparing pile demands estimated from ESA recommended by Caltrans/ODOT with those computed from NDA showed that the guidelines by Caltrans/ODOT (100% kinematic combined with 50% inertia) slightly underestimates demands for subduction earthquakes with long durations. A revised ESA method was developed to extend the application of the Caltrans/ODOT method to subduction earthquakes. The inertia multiplier was back-calculated from the NDA results and new multipliers were proposed: 100% Kinematic + 60% Inertia for crustal earthquakes and 100% Kinematic + 75% Inertia for subduction earthquakes. The proposed ESA compared reasonably well against the NDA results for elastic piles. The revised method also made it possible to estimate demands in piles that performed well in the dynamic analyses but could not be analyzed using Caltrans/ODOT method (i.e. inelastic piles that remained below F_{ult} on the liq pushover curve). However, it was observed that the pile demands became unpredictable for cases where the pile head displacement exceeded the displacement corresponding to the ultimate pushover force in liquefied conditions. Nonlinear dynamic analysis is required for these cases to adequately estimate pile demands.

DEDICATION

To my loving family, whose support and encouragement made this possible

ACKNOWLEDGEMENTS

First and foremost, I would like to express my deepest gratitude to Dr. Arash Khosravifar for serving as my advisor during the course of this project. Of course, his technical knowledge was invaluable for navigating the many obstacles I encountered throughout the research process. His impact, though, extended far beyond this research endeavor. I consider myself lucky for having been able to witness the level of passion and preparedness with which Arash approaches his work, and I'm grateful for all of the kind words and encouragement he provided throughout my time as a graduate student.

My interest in geotechnical engineering began with the undergraduate courses I took from Professor Emeritus, Dr. Trevor Smith. His unique teaching style and practice oriented approach sparked my interest in the subject. For that, I would like to thank him.

I would also like to thank my other thesis committee members, Dr. Franz Rad and Dr. Thomas Schumacher of Portland State University, as well as Jason Bock, of Geotechnical Resources Inc., for reviewing the manuscript and providing valuable feedback.

Lastly, I'd like to thank the Deep Foundations Institute (DFI) and their Seismic and Lateral Loads Committee for providing the funding that enabled me to undertake this research project. Their generosity is greatly appreciated.

TABLE OF CONTENTS

LIST OF TABLES

LIST OF FIGURES

LIST OF ABBREVIATIONS AND ACRONYMS

A_g	Gross cross-sectional area
API	American Petroleum Institute
ARS	Acceleration response spectrum(a)
CSZ	Cascadia Subduction Zone
DSHSA	Deterministic seismic hazard analysis
ESA	Equivalent static analysis
F_{ult}	Ultimate pushover force
FE	Finite element
GMM	Ground motion model
M_{max}	Maximum bending moment
NDA	Nonlinear dynamic analysis
PBEE	Performance based earthquake engineering
PHF	Portland Hills Fault
PNW	Pacific Northwest
PSHA	Probabilistic seismic hazard analysis
RC	Reinforced Concrete
SAR	Spectral acceleration ratio

SFSI	Soil Foundation Structure Interaction
SSP	Site Specific Procedure
UHRS	Uniform Hazard Response Spectrum

1 INTRODUCTION

1.1 Background

Experience has shown that the effects of liquefaction-induced lateral spreading can be disastrous for bridge foundations (e.g. JGS 1996, Boulanger at al. 2007, Franke and Rollins 2017). At the conceptual level, our understanding of the mechanics underlying liquefaction and lateral spreading have been sufficient for quite some time; however, a similar degree of understanding regarding the interaction between laterally spreading soil and structure has been more evasive. Within the last few decades, researchers have made use of numerical models, physical tests and case histories to better understand the mechanisms involved in the soil-structure interaction problem posed by lateral spreading (e.g. Tokimatsu and Boulanger, 2006).

In areas with potentially liquefiable soils and either sloping ground or free-face conditions, the lateral load imposed by the horizontal displacement of soil can be significant and must be explicitly accounted for in the design of the foundation systems. Large diameter reinforced concrete (RC) extended pile shafts (or cast-in-place drilled holes, CIDH) can be an effective foundation choice in these areas because of the large stiffness they offer relative to the magnitude of kinematic forces that can develop against them. Unfortunately, the guidance on how to combine inertial and kinematic loads for piles foundations subjected to lateral spreading is still quite varied. Complicating the issue further is the fact that much of the work that serves as a basis for current design recommendations focused on elastic pile behavior and short duration motions (i.e. non-subduction ground motions). A majority of the Pacific Northwest (PNW) is faced with a moderate to high seismic hazard levels (Figure 1-1), with a sizeable portion of the hazard stemming from the Cascadia Subduction Zone (CSZ). This means that for practitioners in the PNW, the effects of inelasticity and long duration ground motions are of particular concern. With the emergence of performance-based earthquake engineering, the shortcomings in the current recommendations are emphasized because of the increased emphasis that performance based earthquake engineering places on estimates of deformation (Bozorgnia and Bertero 2004). It is essential that the displacement demands computed from simplified procedures, such as equivalent static analysis (ESA), are consistent with the demands obtained from more refined analysis methods, such as nonlinear dynamic analysis (NDA).

1.2 Literature review

Since the early 1990's research regarding lateral spreading and soil foundation structure interaction (SFSI) has seen a sharp uptick. As the field continues to evolve, new papers and recommendations will accompany our increasing knowledge of the subject. The discussion in this section only serves to introduce some of the most relevant or seminal papers on the topic covered in this research.

Early recommendations regarding the combination of inertial and kinematic loads in piles were provided by Martin et al. (2002), who recommended that the two load cases be considered independently. This recommendation was based on the idea that the two loads are unlikely to peak simultaneously. Therefore, it was believed that designers could simply analyze the two cases separately and envelope the pile response; however, the authors of the study recognized the fact that our understanding of the mechanisms involved in this particular SFSI problem was limited. Furthermore, they acknowledged the notion that long duration motions may increase the probability that these two forces could interact constructively.

Chang et al. (2006), Tokimatsu et al. (2005) and Brandenberg et al. (2005) showed that the interaction between inertial and kinematic loads could act in or out of phase. Boulanger et al. (2007) showed that inertial demands from the superstructure on elastic piles in the liquefied case (i.e. with lateral spreading) ranged from about 30% to 50% of the inertial demands in nonliquefied conditions, depending on the frequency content of the input motion. Ashford et al. (2011) synthesized a decade's worth of research on the topic and presented a design recommendation for bridge pile foundations in the same combination of inertial and kinematic loading recommended by Boulanger (2007) was adopted. This design recommendation eventually served as the primary basis for the development of the Caltrans (2012) 50% inertia recommendation. Khosravifar (2011) explored the interaction between kinematic and inertial loads for inelastic piles using nonlinear dynamic analysis (NDA) methods, including a rather expansive parametric study. He found that the equivalent static analysis (ESA) procedure resulted in more accurate estimates of pile head displacements (relative to NDA analysis) when 100% of the inertial displacement demands are combined with the kinematic loading.

The Oregon Department of Transportation Geotechnical Design Manual (2014) currently defers to the Ashford et al. (2012) guideline of combining 50% of the nonliquefied inertial load with 100% of the liquefied kinematic load. The Washington State Department of Transportation (WSDOT 2015) differs from its two neighboring west coast states regarding the combination of inertial and kinematic loading. WSDOT currently recommends 25% of the nonliquefied inertial force in combination with 100% of the liquefied kinematic force.

The discrepancy between current design guidelines is a proverbial “red flag” for practitioners involved in the design of inelastic piles. The issue is exacerbated by the fact that Oregon practitioners are faced with a seismogenic source capable of generating long duration ground motions, a factor that was not considered in the codified kinematic and inertial loading combination factors. There is a need to investigate the effects of long-duration ground motions and pile inelasticity on the adequacy of Caltrans' simplified ESA procedure.

1.3 Research objective

The primary objective of this research is to develop a design guideline for the inelastic behavior of piles due to liquefaction-induced lateral spreading and superstructure inertia. The revised guideline will include the effects of pile inelasticity and long duration ground motions by utilizing a site-specific ground motion analysis framework that is in general accordance with the current state of practice in Oregon.

1.4 Structure of thesis

One of the aims of this paper is to present the research findings in a manner that is most useful to geotechnical practitioners in the region. As such, the structure of this thesis attempts to mirror the workflow involved in a typical site specific seismic hazard analysis. The organization of the thesis is as follows:

- Chapter 2 discusses the site-specific hazard analysis for two sites selected in Oregon. This includes a discussion of the relevant seismogenic sources, probabilistic seismic hazard analysis (PSHA), deterministic seismic hazard analysis (DSHA), and target spectra development.

- Chapter 3 includes discussion of the ground motion selection process for each site, along with the ground motion scaling and matching processes that were used to modify the original ground motion response spectra.
- Chapter 4 presents an overview of the finite element (FE) model used in the study. The discussion includes various components of the NDA model such as the soil elements, structural elements, and p-y springs. Furthermore, an example dynamic response of the NDA model and the relevant results is provided in this chapter.
- Chapter 5 presents an overview of the ESA model and the results of ESA in accordance with Caltrans and ODOT. The results from the ESA are compared to the those of the NDA The comparison between the methods serves as the basis for the proposed revision to Caltrans' guidance, which is also presented in this chapter.
- Chapter 6 presents a discussion regarding the results of the study and provides a summary of the key findings. In addition, limitations in the work are identified and recommendations for future research are provided.

1.5 Tables and Figures

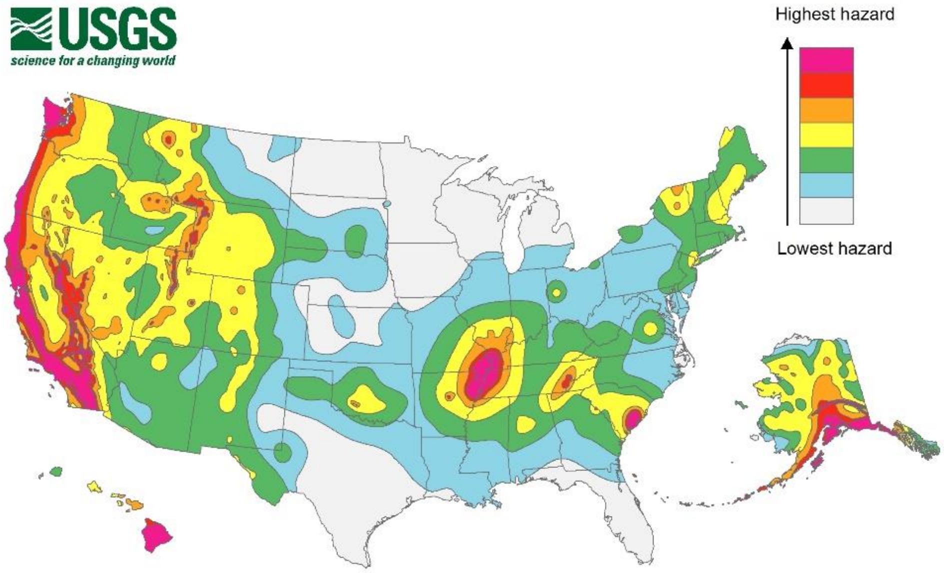

Figure 1-1: Levels of seismic hazard across the U.S. based on the USGS 2014 source model (USGS 2014)

2 SITE-SPECIFIC SEISMIC HAZARD ANALYSIS

2.1 Background

Oregon’s seismicity presents interesting challenges for local practitioners. Much of Oregon’s more heavily populated western half faces some level of threat from either shallow crustal Quaternary faults or the Cascadia Subduction Zone (CSZ). Wong (1995) presented a strong case for Oregonians to increase their awareness of the seismic hazard in this region, while alluding to the fact that Oregon is sometimes overlooked in terms of its seismic hazard. The state contains crustal faults capable of generating M_w=7.0 or greater earthquakes in Portland and other areas in eastern Oregon, as well as the offshore CSZ that can generate earthquakes up to M_w=9.2 (USGS 2008).

While a characteristic earthquake on the PFH would likely cause more severe damage around the Portland-Metro region (Wong 1995), the mega earthquake potential of the CSZ has managed to capture the attention of the public and state officials alike. In 2013 the Oregon Seismic Safety Policy Advisory Committee (OSSPAC) presented the *Oregon Resilience Plan* to the state legislature. The OSSPAC is made up of 18 individuals from across the state that represent a wide variety of interests regarding public policy related to earthquakes. Their plan, the *Oregon Resilience Plan,* was the culmination of a two-year-long effort to present recommendations regarding the state-wide impact of a large earthquake and how best to mitigate and prepare for the dire consequences that would likely follow. Their study estimated tens of billions of dollars in damage to property and infrastructure alone (i.e. economic impacts were not included in the estimate) for a potential CSZ earthquake. Figure 2-1 shows a map of damage potential that was generated for a moment-magnitude 9.0 CSZ earthquake (OSSPAC 2013). Nearly a quarter of the state, stretching from the Oregon coast as far east as Portland, is expected to be moderately to heavily damaged. It is clear that the seismic hazard in Oregon presents some unique considerations due to its seismogenic setting and the tremendous social and economic costs associated with a characteristic event for either of these two sources.

Under severe levels of ground shaking that have the potential to occur across the state, liquefaction and lateral spreading will undoubtedly affect some portion of our existing infrastructure. For these cases, AASHTO (2014) and ASCE 7-10 require site specific site response analysis, which will be referred to from here on out as site-specific procedure (SSP). The goal of any SSP is to more accurately estimate the propagation of ground motions up a soil column to some point of interest, usually taken as the ground surface. An SSP with thoughtful input parameters can provide the engineer with more confidence in the soil response and subsequently, the demands on the structure.

This chapter begins by discussing the site selection process for the study and the seismogenic setting of the chosen sites. The remainder of the chapter is devoted to discussion of the PSHA (probabilistic seismic hazard analysis), DSHA (deterministic seismic hazard analysis), development of the requisite target spectra, and finally the governing spectra for design.

2.2 Site selection

While geotechnical practitioners are often constrained to analyzing sites that are presented to them by clients or contractors, this study provided an opportunity select the hypothetical project sites. Recognizing that the effect of strong motion duration on the interaction of kinematic and inertial loading was of primary importance, it was essential that the chosen sites provide response data across a spectrum of potential earthquake durations.

The first site that was chosen was is in Oregon’s most heavily populated city, Portland (U.S. Census 2010). Portland is also Oregon’s most seismically active region (Wong 1995). Table 2-1 provides the latitude and longitude of the hypothetical project site. The site is located just west of the Willamette River, which is a north/south trending river and is the major tributary of the Columbia River. Very generally speaking, the geologic conditions in this area can be described as recent Quaternary sand, silt, and gravel deposits overlying older Quaternary sedimentary and volcanic rock deposits, in turn overlying Tertiary volcanic rock (Trimble 1963). The fact that the city is split by the Willamette River and has numerous bridges linking its eastern and western halves, in combination with the moderately-high seismicity in the area, means the findings of this study may be directly applicable to existing, or future, structures located in Portland.

The second hypothetical site was chosen in Astoria, Oregon. Astoria is one of Oregon's most populous coastal cities, with nearly 10,000 inhabitants (U.S. Census 2010). The city is located near the mouth of the Columbia River and is home to two bridges that allow US Highway 101 to pass over Young's Bay and the Columbia River. The near-surface geologic deposits in the area are mostly unconsolidated alluvial deposits or lower to middle-aged Miocene mudstone deposits from the Astoria formation (Niem and Niem 1985). The site coordinates are provided in Table 2-1.

2.3 Seismicity

2.3.1 Cascadia Subduction Zone

At approximately 700 miles long, the CSZ zone stretches along the Pacific Coast from British Columbia to northern California. It occurs at a convergent boundary between the North American plate and several smaller plates. More specifically, off the coast of Oregon and Washington it is the Juan DeFuca plate that is subducting beneath the North American plate at an average rate of 1.6-inches per year (CREW 2013). This build-up and eventual release of strain energy will cause the next great Cascadia earthquake.

Figure 2-2 shows a combined plan and cross-sectional view of the boundary between the plates in the CSZ. It is clear that a portion of the Juan De Fuca plate has already descended beneath the overriding North American plate and subsequently, the state of Oregon. Off the coast of the Pacific Ocean, though, where the North American Plate and the Juan De Fuca come together, exists a “locked zone.” The “locked zone” can be thought of as the region where the colliding plates are stuck together, constantly accumulating strain (CREW 2013). The distinction between the locked zone and the portion of the Juan De Fuca that has already subducted beneath the North American plate is an important one because it gives rise to very different potentials for ground motion intensity.

Investigators have categorized potential CSZ earthquakes by the depth at which they are likely to occur. Shallow, or “interface,” earthquakes occur at a depth up of 20 to 40 miles (depending on site location) below the surface of the earth, which corresponds to a rupture within the locked portion of the CSZ. The magnitude 9 scenario is usually attributed to this type of shallow rupture. On the other hand, deeper and less intense earthquakes can occur in the portion of the CSZ where the Juan De Fuca slab has already subducted; these types of earthquakes are known as “intraslab” earthquakes, and they occur at depths below the interface zone. Figure 2-3 provides the logic tree used to model a CSZ rupture for the 2008 USGS source model.

2.3.2 Shallow crustal

Since ground motion intensity dissipates with increased distance between the source and the receiver, smaller magnitude crustal earthquakes at shorter source-to-site distances are capable of producing intense shaking in areas near the rupture. The downtown Portland area is thought to contain three active faults: the Oatfield Fault, the Eastbank Fault, and the Portland Hills Fault (PHF). Wong et al. (2001) provide a thorough discussion regarding the characterization of the PHF and to some extent, the Eastbank and Oatfield Faults. However, the East Bank and Oatfield faults were not explicitly included in the 2008 or 2014 USGS probabilistic seismic hazard studies; instead, these faults are considered as part of the Portland Hills Fault zone.

Based on the USGS Seismic Hazard Map Documentation (2008), there are three active faults located within 10 miles of Portland. The three faults and their respective parameters are shown in Table 2-2. Only the PHF was considered for further analysis because it can produce the largest earthquake at the shortest distance from the site.

2.4 PSHA and DSHA

The target design spectra were developed based on site-specific procedures outlined in ASCE 7-10 (MCE_R) and AASHTO (975-year return period). These procedures require performing probabilistic seismic hazard analysis (PSHA) and deterministic seismic hazard analysis (DSHA) as described in the next sections. The target spectra were developed for Site Class B/C (Vs = 760 m/s) and were later used in site-response analysis described in Chapter 4.

2.4.1 PSHA

Probabilistic seismic hazard analyses (PSHA) were conducted at two different return periods for each site: a 2475-year return period (ASCE 7-10) and a 975-year return period (AASHTO). The PSHA was performed for Site Class B/C (Vs=760 m/s). The analyses were conducted with the software EZ-FRISK (Fugro 2016), which utilized the USGS 2014 seismic source model. The choice of ground motion models (GMM) implemented in the USGS 2014 source model varies depending on the seismicity source. Tables 2-3 and 2-4 show the GMM's and weightings that were used during the PSHA to model the PHF and CSZ.

The spectra that result from PSHA are known as uniform hazard response spectra (UHRS), meaning that any single spectral acceleration value on the curve has an equal probability of being exceeded within the specified exposure period.

An inherent property of PSHA methodology is that it effectively combines the hazard contributions from various sources into a single value of spectral acceleration. Often times, the individual contributions from various sources to the overall hazard are of significant interest (Table 2-5). Figures 2-4 to 2-7 show the USGS (2008) seismic hazard deaggreation for the two different sites and return periods at PGA and at 1.0 second. The following observations can be made from the hazard deaggregation:

1. The geographic distribution of mean hazard and modal hazard values are relatively consistent between PGA and Sa(1.0s) for both sites.

2. The hazard to the Portland site is predominantly coming from two distinct regions.
3. A substantial portion of the hazard to the Astoria site can be attributed to a single region.

In Astoria, the seismic hazard is dominated by the CSZ (corresponding to earthquake magnitude Mw = ~9 at source-to-site distance of ~19 km), which is represented by the large cluster of bars at short distance in the geographic deaggregation. In this case, the mean hazard and the modal hazard are nearly identical because they are essentially coming from a single source, with the only differences stemming from the different fault rupture schemes that the USGS considered for the CSZ.

For the Portland site, the hazard has a bi-modal distribution as shown by the two large clusters of bars on the deaggregation figures (corresponding to Mw= 9 and source-to-site distance~90 km for the CSZ and Mw=7 and source-to-site distance of ~1 km).

2.4.2 DSHA

A deterministic seismic hazard analysis (DSHA) is an alternate method of quantifying the seismic hazard at a site, wherein specific earthquake scenarios are explicitly considered. The resulting envelope of spectral acceleration ordinates, for the different scenarios, is usually adopted as the target response spectrum. Selection of the earthquake scenarios for consideration involves the selection of magnitude, distance, and ground motion level (Abrahamson 2006).

The CSZ and PHF (for the Portland site) and the CSZ (for the Astoria site) were selected for deterministic analyses at the magnitude-distance pairs shown in Table 2-6. The ground motion level was specified by the relevant design code, which was median+1 sigma per ASCE 7-10. AASHTO (2014) does not require practitioners to perform DSHA, but leaves the option available for where a DSHA may result in a reduction of spectral acceleration values. This study did not consider deterministic spectra for the development of the AASHTO target spectra.

A final piece of the DSHA that was required to generate the response spectra was the selection of the ground motion models (GMM). In the case of the PHF, the NGA WEST-2 GMM (Bozorgnia et al. 2014) were used with the same weighting scheme recommended by USGS (2014), as shown in Table 2-3. In the case of the CSZ, the selection of GMM differed slightly from that of USGS. Namely, the Atkinson and Boore (2003) model was not included, and the weight of this GMM was equally divided amongst the remaining three. The exclusion of this GMM did not affect the final target spectra because the Atkinson and Boore model tends to predict larger acceleration values than the other three GMM and our target spectra was controlled by PSHA, as will be shown in the subsequent sections. Table 2-7 shows the GMM’s and weighting used to model the CSZ for the DSHA.

The resulting spectra and their weighted geometric means are shown in Figures 2-8 to 2-10. Figure 2-11 shows the weighted geometric mean spectra for the two sources in Portland. For a 2475-year return period and the chosen weighting scheme, the PHF controls the spectral response up to a period of approximately 3 seconds, at which point the CSZ controls.

2.5 Target spectra development

The spectra that were obtained from the PSHA and DSHA were adjusted in accordance with ASCE 7-10 and AASHTO (2014) in order to generate the final target spectra for each scenario. This means that the 2475-year return period UHRS and the median+1 sigma DSHA spectra were adjusted and checked against minimum values in accordance with ASCE 7-10 guidelines, while the 975-year return period UHRS were modified and compared against AASHTO (2014) minimum values.

The Risk-Targeted Maximum Considered (MCE_R) response spectra were developed based on ASCE 7-10 in the general sequence described below:

1. The UHRS spectral acceleration values were scaled by the USGS risk coefficients to yield the risk targeted response spectra for a 1% probability of collapse within a 50-year period. Table 2-8 shows the risk coefficients that were extracted from the USGS seismic design application (https://earthquake.usgs.gov/designmaps/us/application.php) and used in the analysis.

    a. The risk-targeted acceleration values were scaled by the maximum rotated component factors presented in ASCE 7-10 Supplement 1 (2013) to account for the fact that the GMM’s report the geometric mean of the horizontal response. Table 2-8 shows the maximum rotation factors that were used.

2. The DSHA spectral values were scaled by the same maximum rotation factors
    a. The maximum rotated deterministic spectra were checked against the deterministic limit per ASCE 7-10 and the larger of the spectral acceleration values at any given period was used
3. The resulting maximum rotated deterministic spectrum was compared against the maximum rotated risk targeted probabilistic spectrum and the lesser of the spectral acceleration values at any given period was selected (Figures 2-12 and 2-13).

The development of the AASHTO target spectra was less complex, as the code does not require any a risk or directionality adjustments. In this case, each of the 975-year UHRS was simply checked against its respective code-based minimum spectrum. The code-based minimum spectrum was taken as 2/3 of the spectrum generated by the USGS Seismic Design Tool (2008) (without risk or rotation factors), adjusted for site effects. The relevant spectra from this process are shown in Figures 2-14 and 2-15.

2.5.1 Final target spectra

The final result was four target spectra, an MCE_R and an AASHTO spectrum for each site. Figure 2-16 shows all four spectra on a single plot and Table 2-9 provides the spectral ordinates in tabulated form. The MCE_R spectra for Portland and Astoria were governed by PSHA across all periods. In fact, the deterministic spectral acceleration values were substantially larger across the entire period range of interest. In the case of the AASHTO target spectra, the probabilistic spectra controlled across all but very long periods (T <6 seconds), beyond which the 2/3 code based spectra controlled.

2.6 Tables and figures

Table 2-1: Coordinates of the sites selected for this study

Site	Latitude (degrees)	Longitude (degrees)
1 (Portland)	45.519 N	122.672 W
2 (Astoria)	46.174 N	123.870 W

Table 2-2: Parameters for the three faults within 10 miles of the Portland site (USGS 2014)

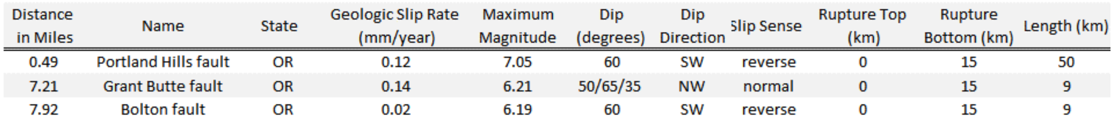

Distance in Miles	Name	State	Geologic Slip Rate (mm/year)	Maximum Magnitude	Dip (degrees)	Dip Direction	Slip Sense	Rupture Top (km)	Rupture Bottom (km)	Length (km)
0.49	Portland Hills fault	OR	0.12	7.05	60	SW	reverse	0	15	50
7.21	Grant Butte fault	OR	0.14	6.21	50/65/35	NW	normal	0	15	9
7.92	Bolton fault	OR	0.02	6.19	60	SW	reverse	0	15	9

Table 2-3: Ground motion models (GMM) and weightings used for the shallow crustal sources in the probabilistic seismic hazard analysis

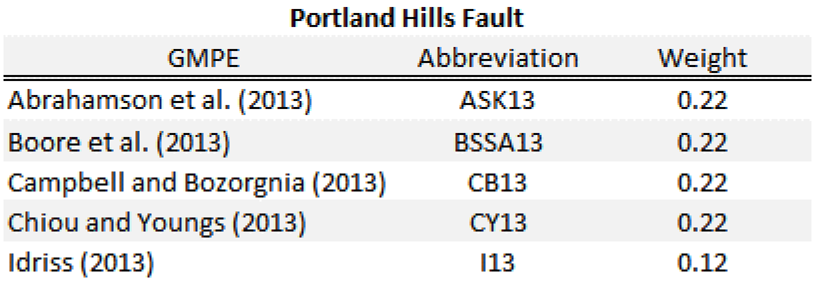

Portland Hills Fault

GMPE	Abbreviation	Weight
Abrahamson et al. (2013)	ASK13	0.22
Boore et al. (2013)	BSSA13	0.22
Campbell and Bozorgnia (2013)	CB13	0.22
Chiou and Youngs (2013)	CY13	0.22
Idriss (2013)	I13	0.12

Table 2-4: Ground Motion Models (GMM) and weightings used to model the Cascadia Subduction Zone in the probabilistic seismic hazard analysis

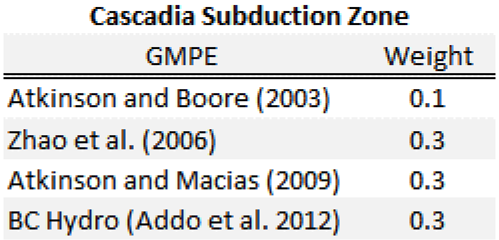

Cascadia Subduction Zone

GMPE	Weight
Atkinson and Boore (2003)	0.1
Zhao et al. (2006)	0.3
Atkinson and Macias (2009)	0.3
BC Hydro (Addo et al. 2012)	0.3

Table 2-5: Summary of hazard deaggregation results

		Hazard Contribution (rounded to nearest percent) *			
PSHA Scenario	Structural Period	CSZ (interface)**	CSZ (intraslab)**	PHF	All Other Sources
Portland 2475-year	PGA	32%	19%	21%	28%
	T=1 sec	61%	13%	16%	10%
Portland 975-year	PGA	33%	22%	11%	34%
	T=1 sec	57%	18%	9%	16%
Astoria 2475-year	PGA	98%	2%	0%	0%
	T=1 sec	98%	0%	0%	2%
	PGA	91%	9%	0%	0%

Astoria 975-year	T=1 sec	95%	5%	0%	0%

*based on USGS 2008 deaggregation (v3.3.1), rounded to nearest whole percent

**summation of contribution from different rupture/faulting scenarios

Table 2-6: Magnitude and distance pairs used for deterministic seismic hazard analyses

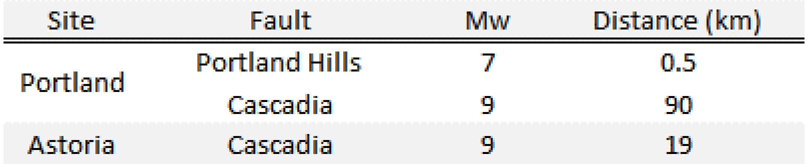

Site	Fault	Mw	Distance (km)
Portland	Portland Hills	7	0.5
	Cascadia	9	90
Astoria	Cascadia	9	19

Table 2-7: GMM's and weighting used to model the Cascadia Subduction Zone in the deterministic seismic hazard analysis

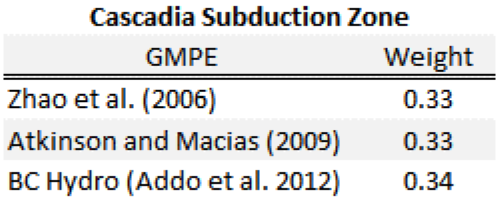

Cascadia Subduction Zone

GMPE	Weight
Zhao et al. (2006)	0.33
Atkinson and Macias (2009)	0.33
BC Hydro (Addo et al. 2012)	0.34

Table 2-8: Risk and maximum rotation coefficients, per ASCE 7-10, for the two sites

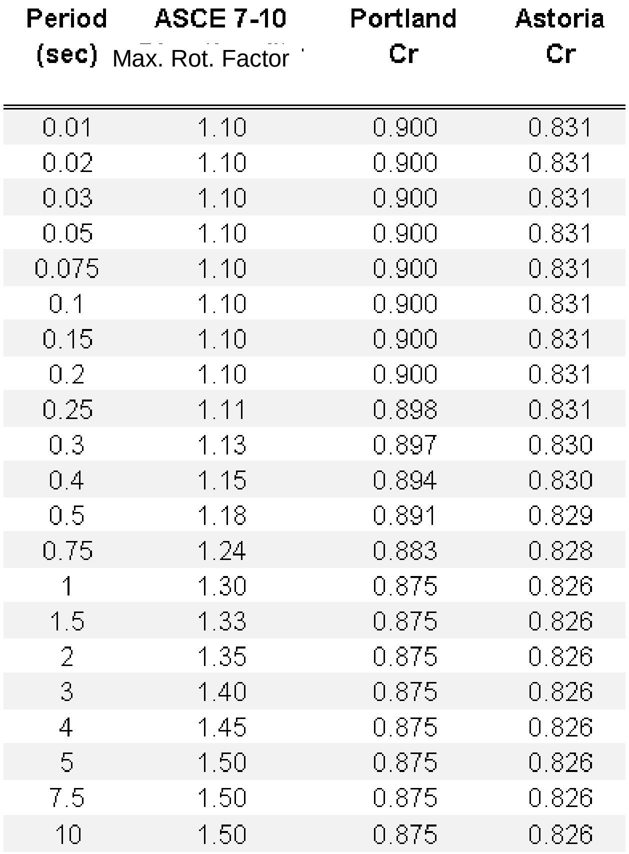

Period (sec)	ASCE 7-10 Max. Rot. Factor	Portland Cr	Astoria Cr
0.01	1.10	0.900	0.831
0.02	1.10	0.900	0.831
0.03	1.10	0.900	0.831
0.05	1.10	0.900	0.831
0.075	1.10	0.900	0.831
0.1	1.10	0.900	0.831
0.15	1.10	0.900	0.831
0.2	1.10	0.900	0.831
0.25	1.11	0.898	0.831
0.3	1.13	0.897	0.830
0.4	1.15	0.894	0.830
0.5	1.18	0.891	0.829
0.75	1.24	0.883	0.828
1	1.30	0.875	0.826
1.5	1.33	0.875	0.826
2	1.35	0.875	0.826
3	1.40	0.875	0.826
4	1.45	0.875	0.826
5	1.50	0.875	0.826
7.5	1.50	0.875	0.826
10	1.50	0.875	0.826

Table 2-9: Target spectra per ASCE 7-10 and AASHTO LRFD (2014)

	Site 1 (Portland)		Site 2 (Astoria)	
Period (sec)	**MCEr Target (g)**	**AASHTO Target (g)**	**MCEr Target (g)**	**AASHTO Target (g)**
0.01	0.411	0.270	0.779	0.490
0.02	0.439	0.290	0.866	0.544
0.03	0.477	0.313	0.934	0.586
0.05	0.559	0.364	1.026	0.643
0.075	0.731	0.472	1.336	0.820
0.1	0.868	0.557	1.573	0.958
0.15	0.948	0.609	1.716	1.032
0.2	0.905	0.588	1.649	0.997
0.25	0.833	0.538	1.547	0.933
0.3	0.778	0.500	1.466	0.882
0.4	0.690	0.435	1.303	0.780
0.5	0.605	0.374	1.129	0.669
0.75	0.477	0.281	0.919	0.510
1	0.404	0.226	0.777	0.410
1.5	0.283	0.150	0.566	0.287
2	0.221	0.114	0.439	0.214
3	0.145	0.073	0.283	0.128
4	0.112	0.052	0.197	0.093
5	0.089	0.039	0.144	0.064
7.5	0.053	0.021	0.085	0.038
10	0.040	0.015	0.062	0.029

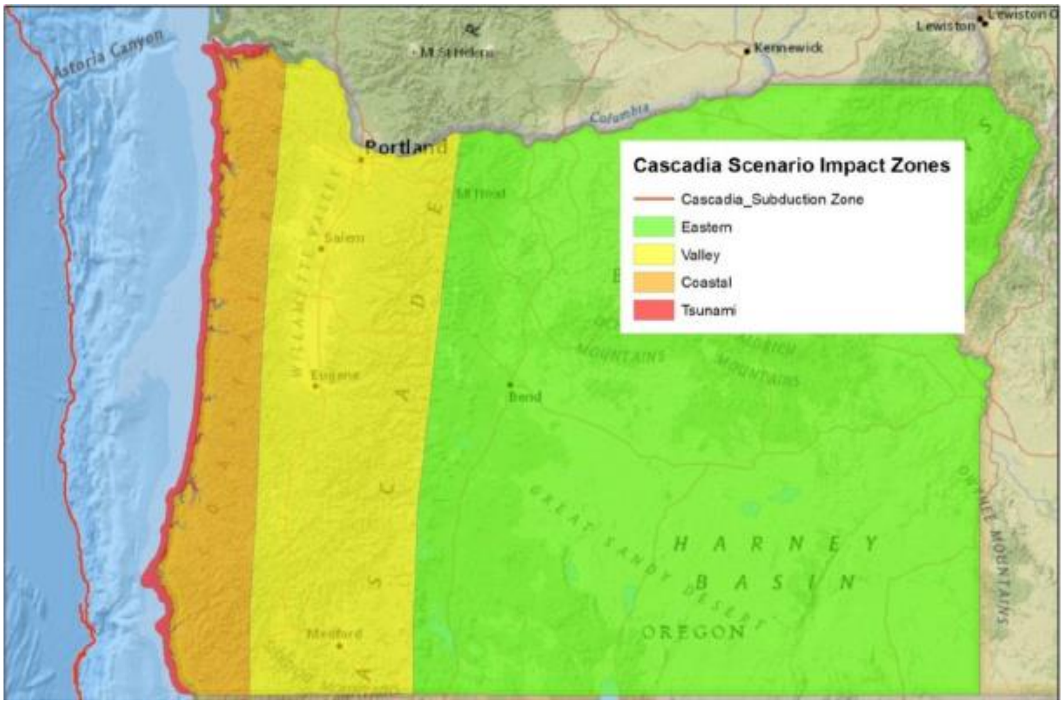

Figure 2-1: Estimated impact zones within Oregon for a characteristic CSZ event -damage will be extreme in the Tsunami zone, heavy in the Coastal zone, moderate in the Valley zone, and light in the Eastern zone (OSSPAC 2013)

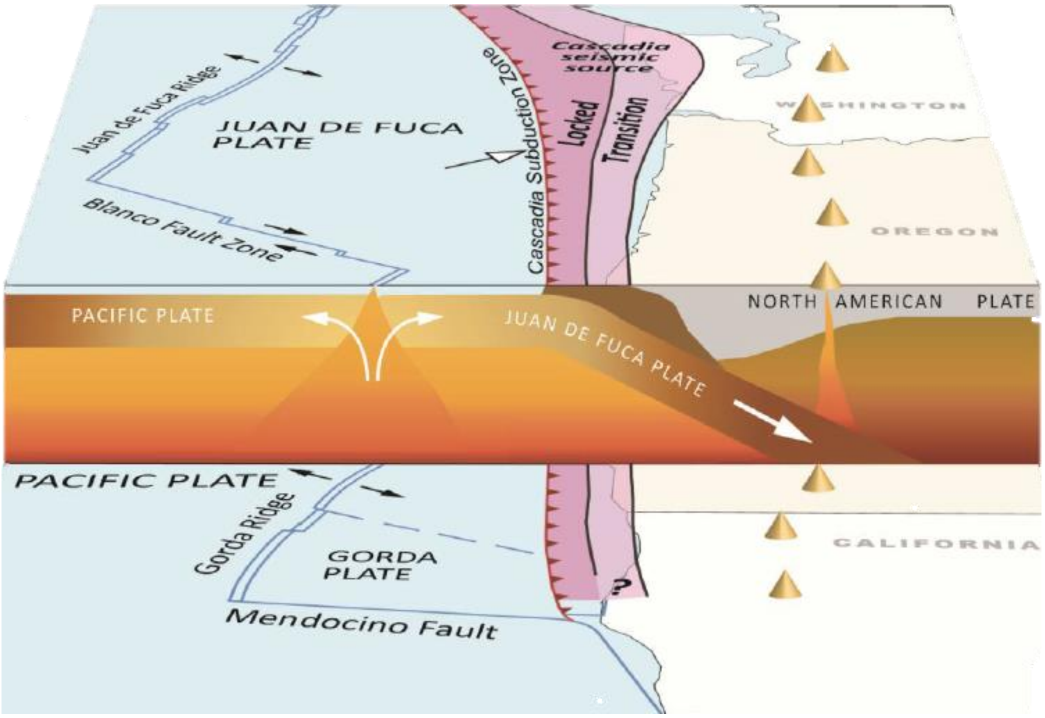

Figure 2-2: Cross section and plan view of the Cascadia Subduction Zone (CREW 2013)

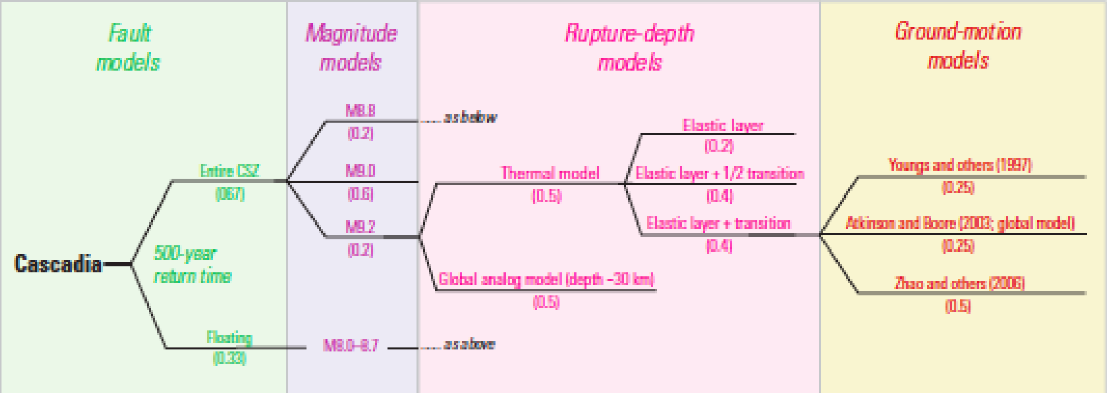

Figure 2-3: Logic tree for the characteristic CSZ earthquake (USGS 2008)

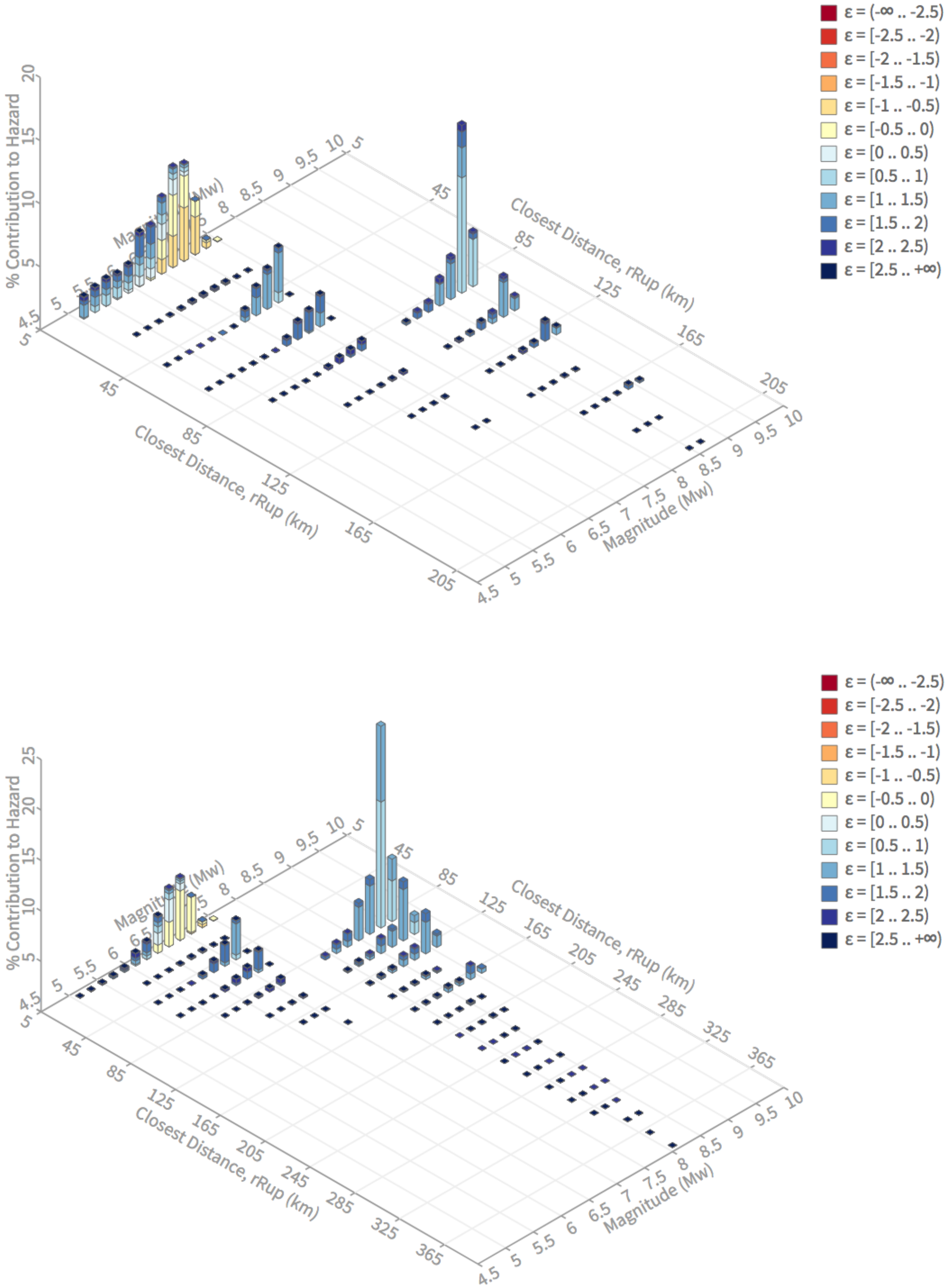

Figure 2-4: Portland seismic hazard deaggregation for the 2475-year return period at PGA (top) and T=1.0 second (bottom) (USGS 2008)

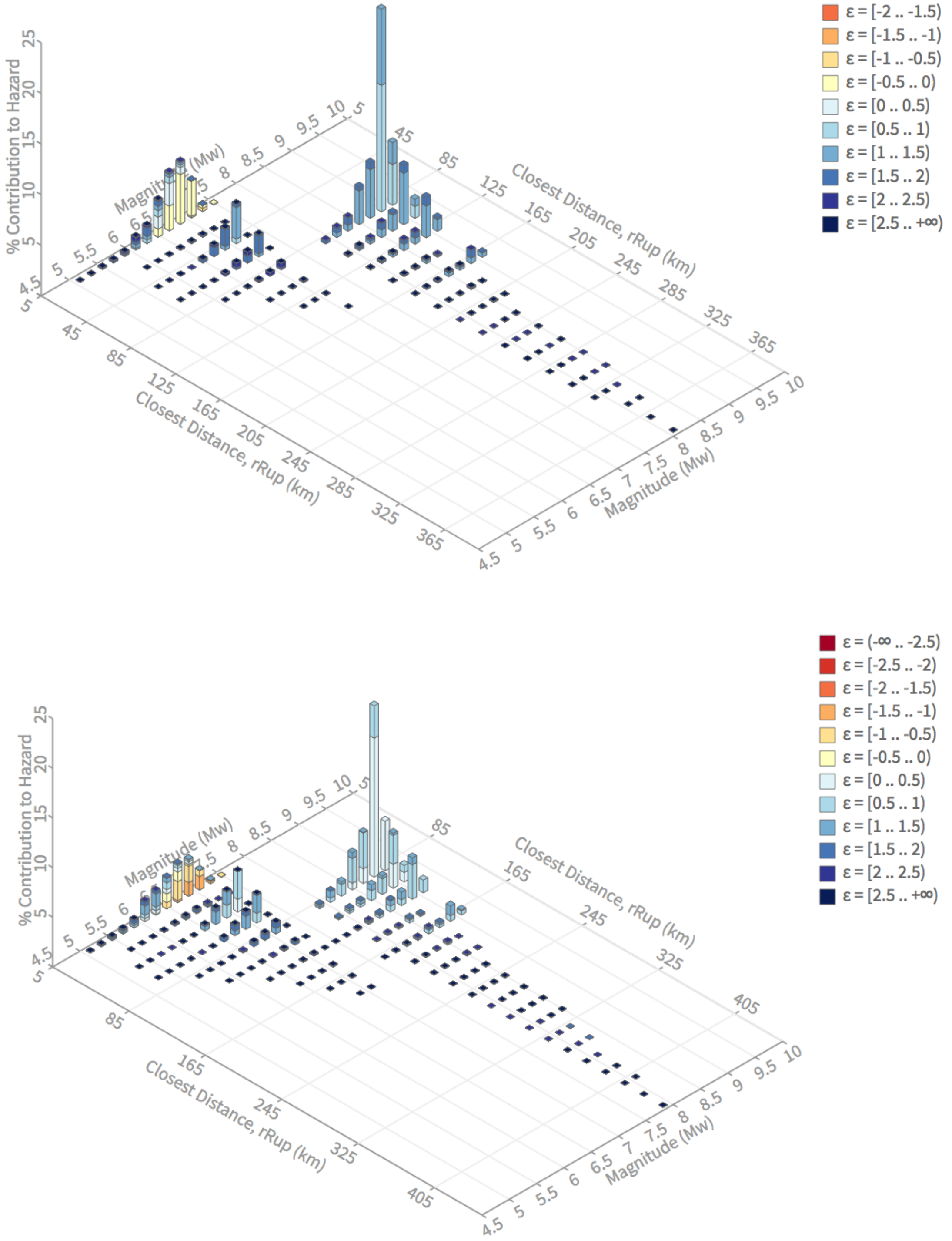

Figure 2-5: Portland seismic hazard deaggregation for the 975-year return period at PGA (top) and T=1.0 second (bottom) (USGS 2008

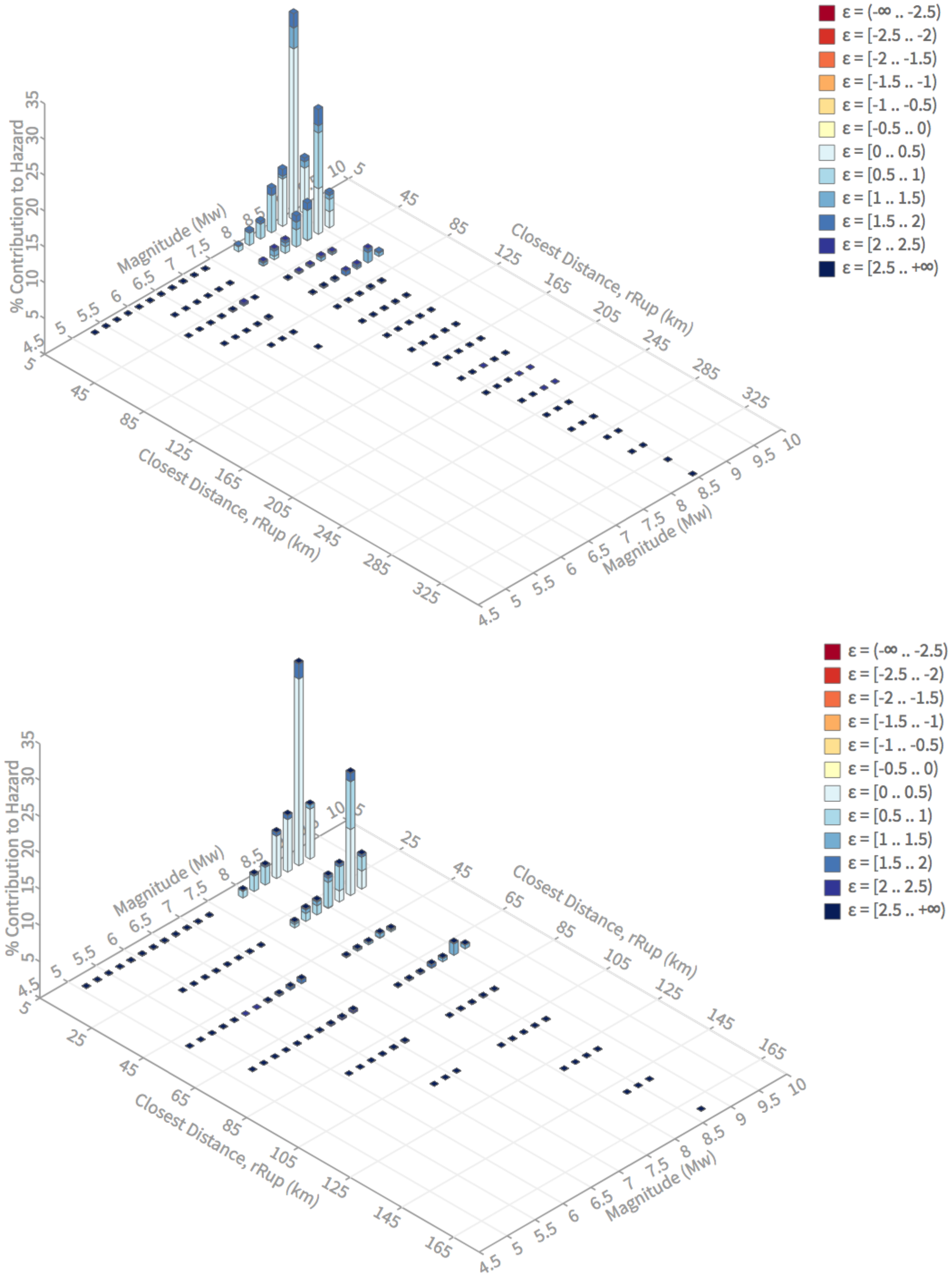

Figure 2-6: Astoria seismic hazard deaggregation for the 2475-year return period at PGA (top) and T=1.0 second (bottom) (USGS 2008)

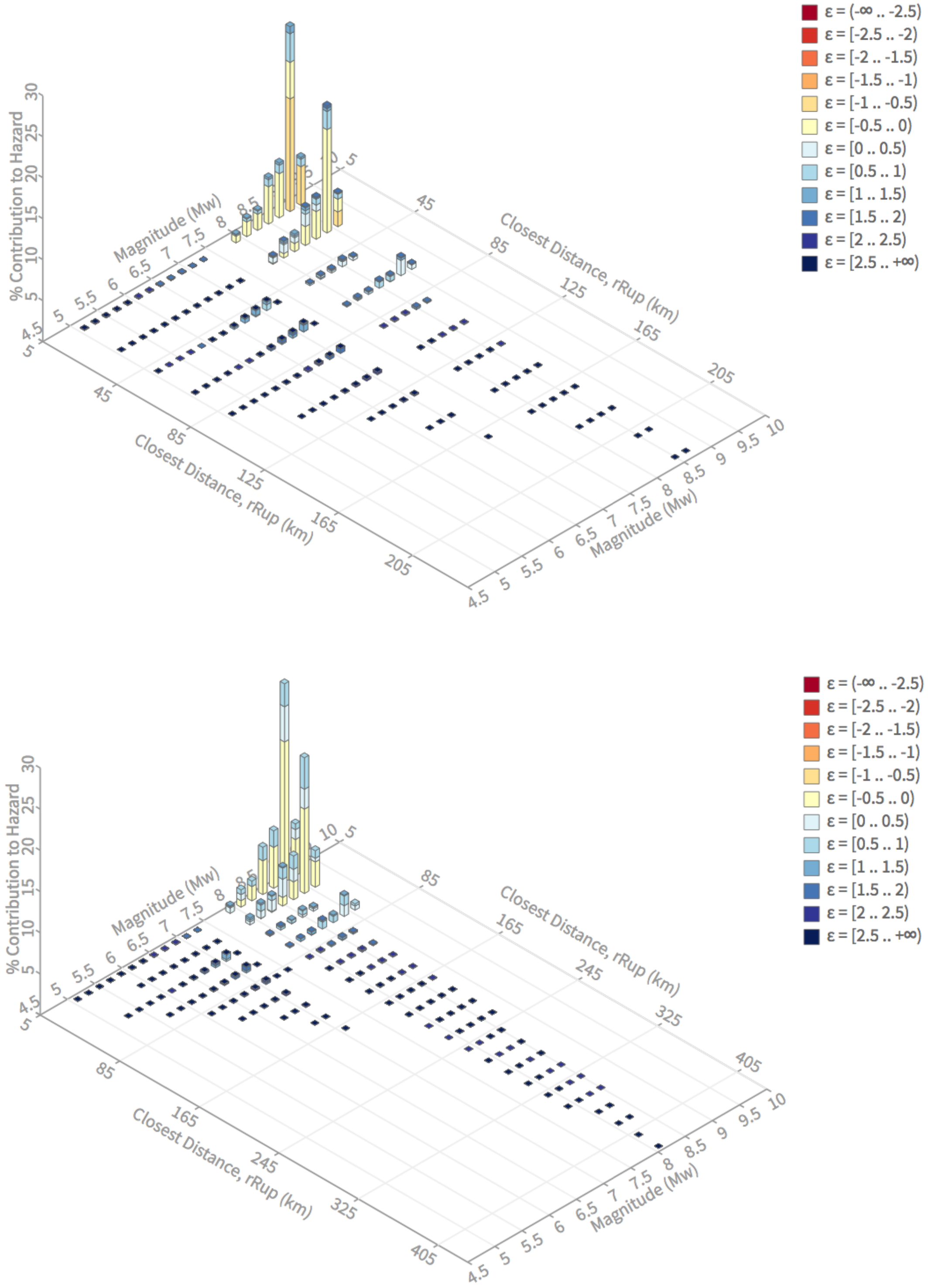

Figure 2-7: Astoria seismic hazard deaggregation for the 975-year return period at PGA (top) and T=1.0 second (bottom) (USGS 2008)

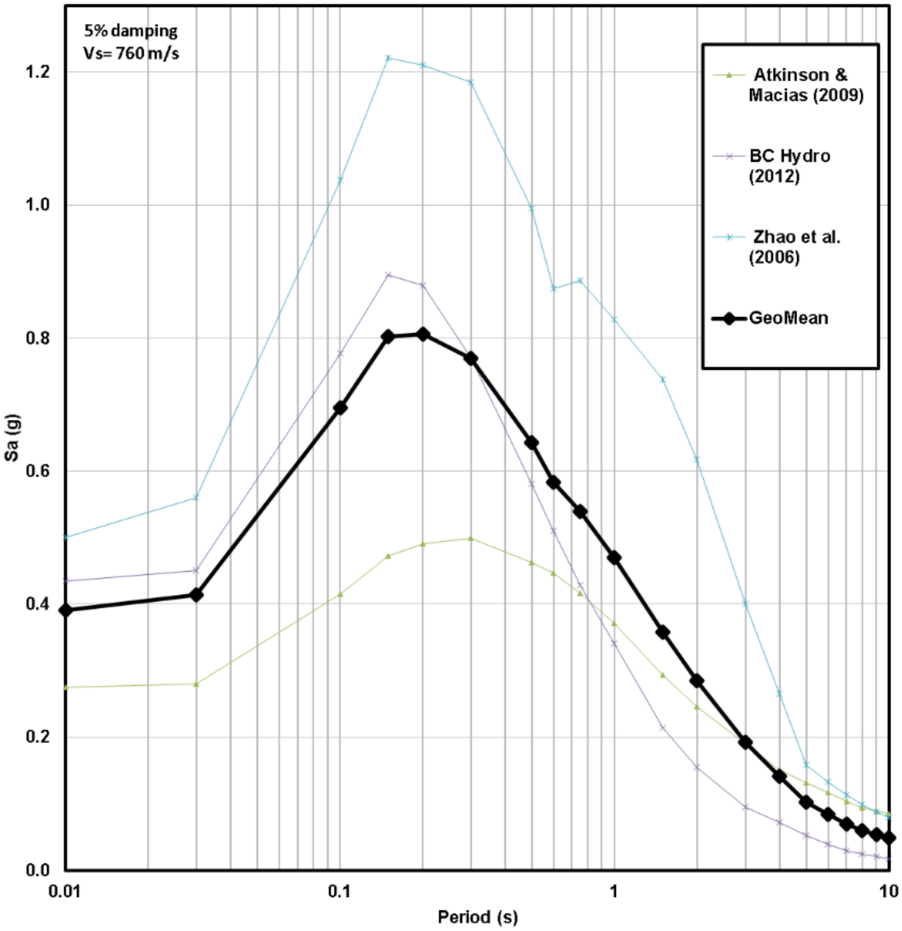

Figure 2-8: Median + 1 sigma deterministic spectra for the Cascadia Subduction Zone at the Portland site

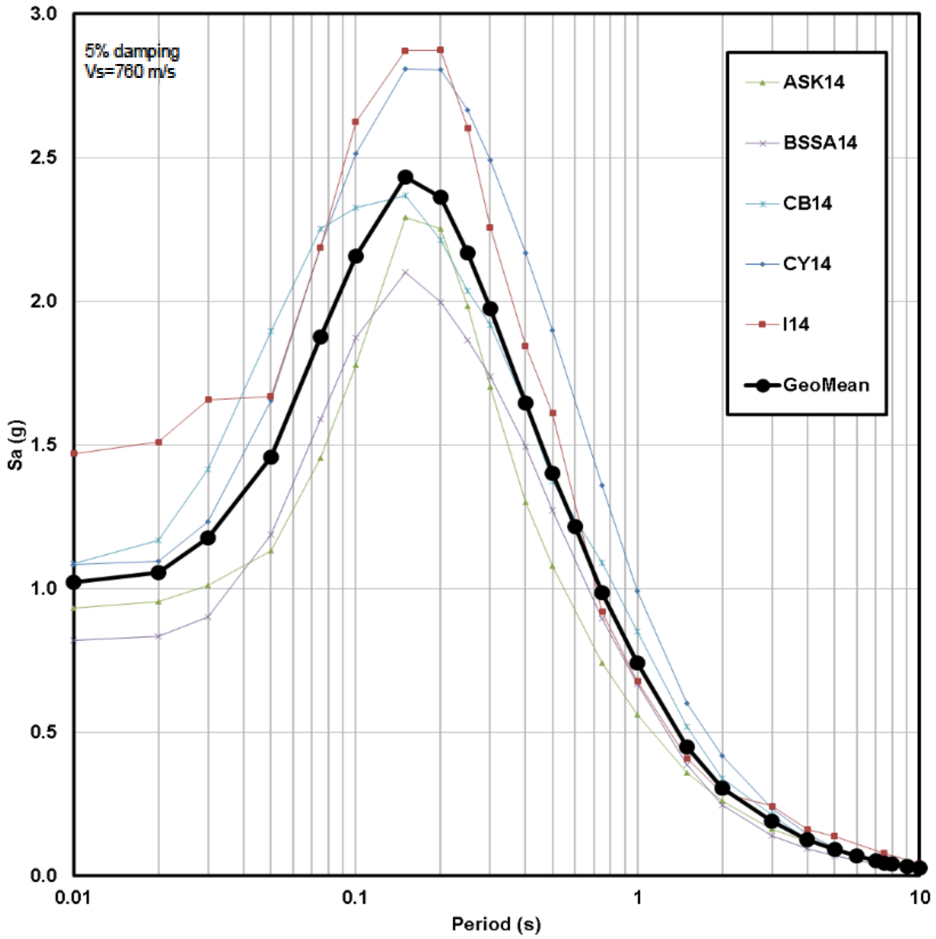

Figure 2-9: Median + 1 sigma deterministic spectra for the Portland Hills Fault at the Portland site

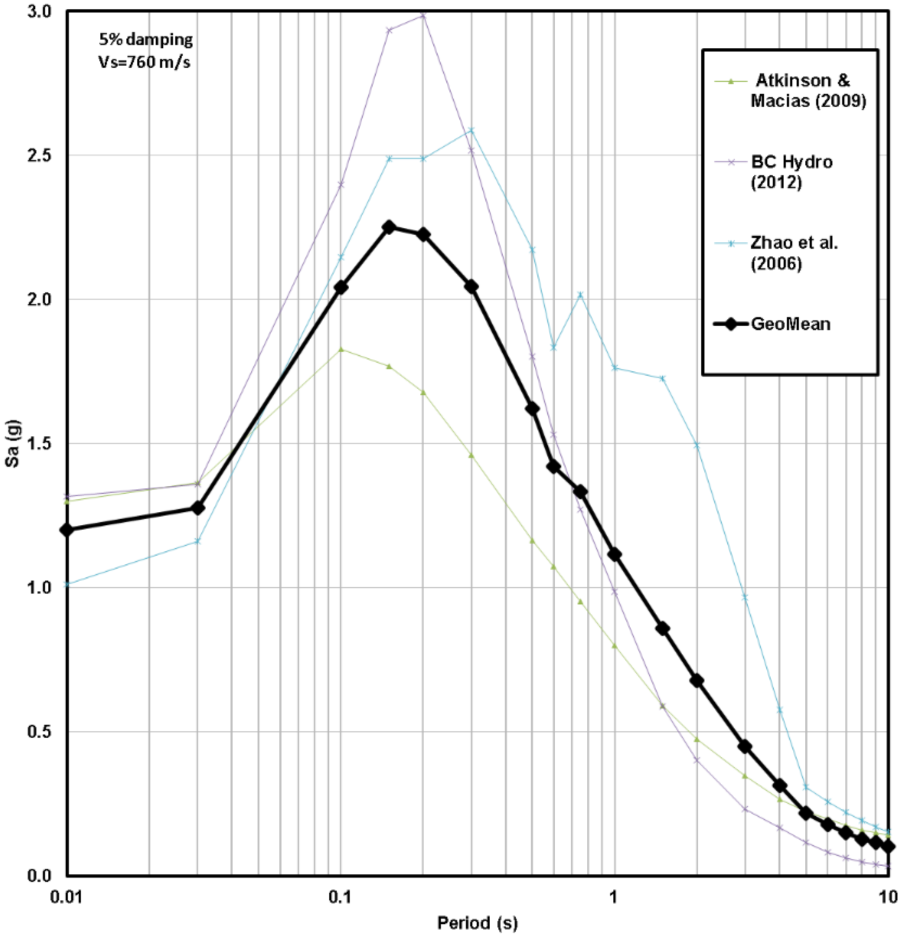

Figure 2-10: Median + 1 sigma deterministic spectra for the Cascadia Subduction Zone at the Astoria site

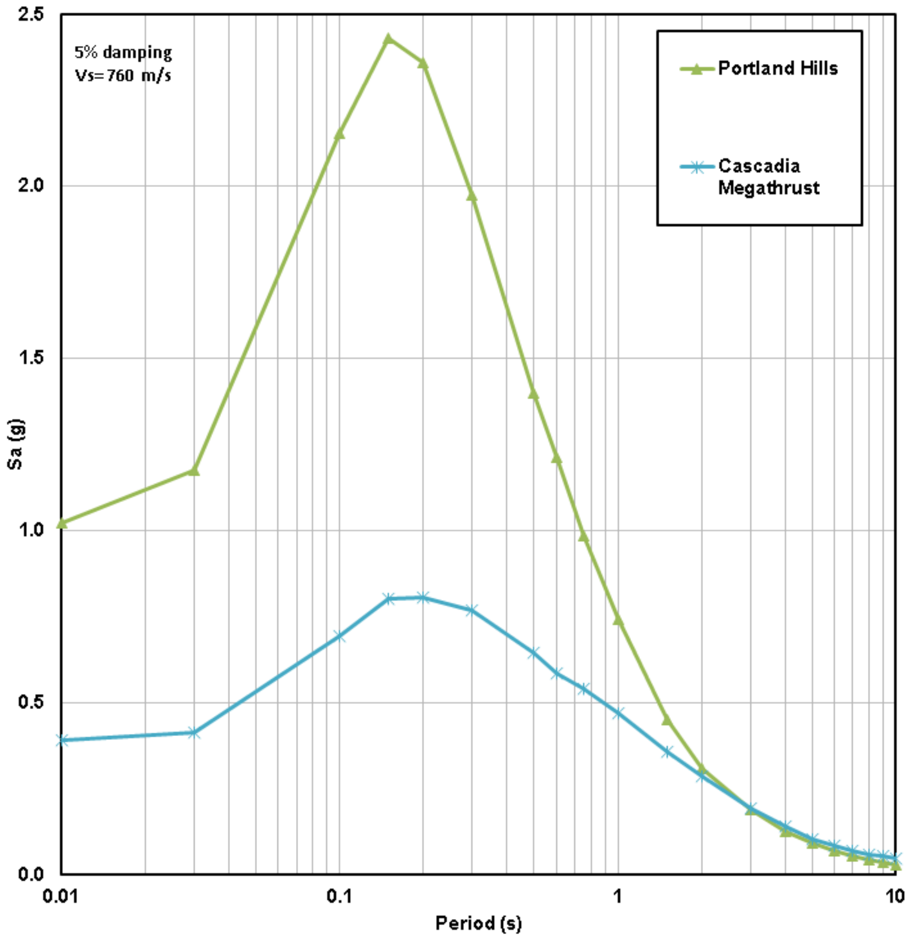

Figure 2-11: Comparison of the deterministic spectra for the two sources at the Portland site

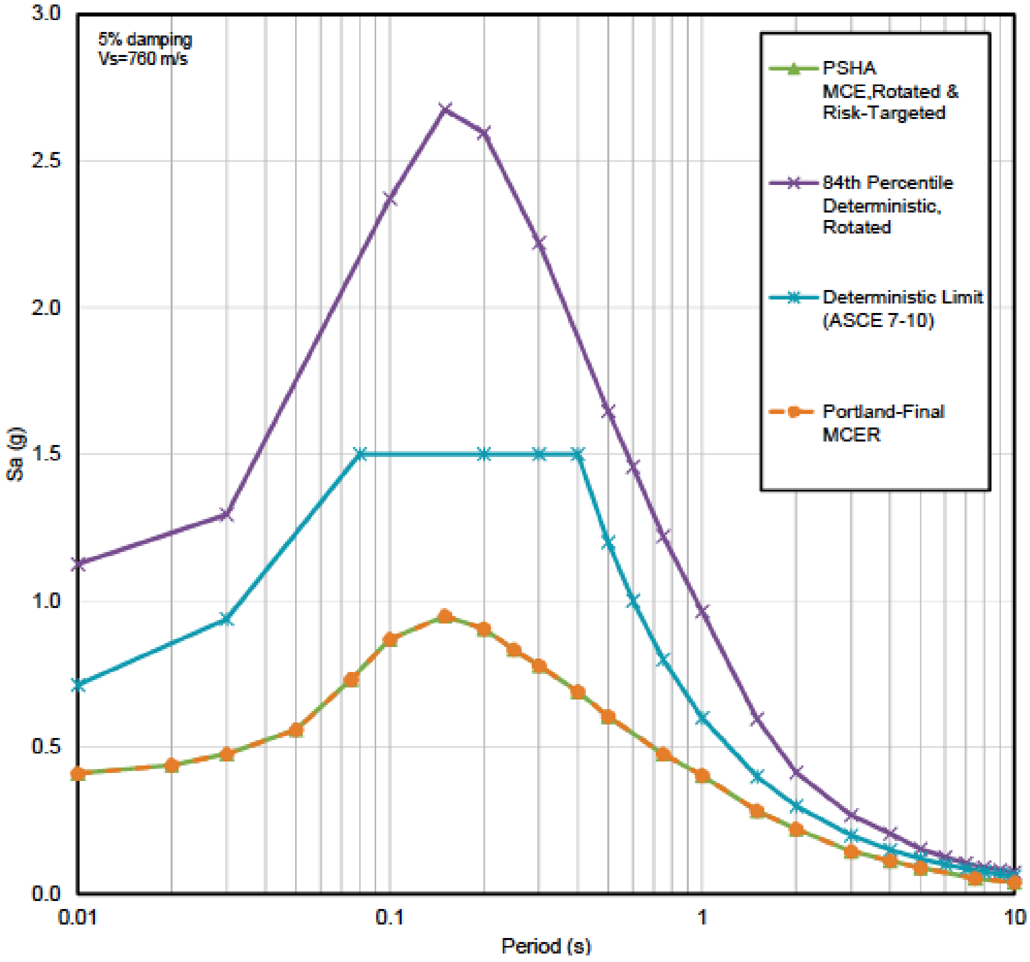

Figure 2-12: Development of the target MCE_R spectrum, per ASCE 7-10, for the Portland site

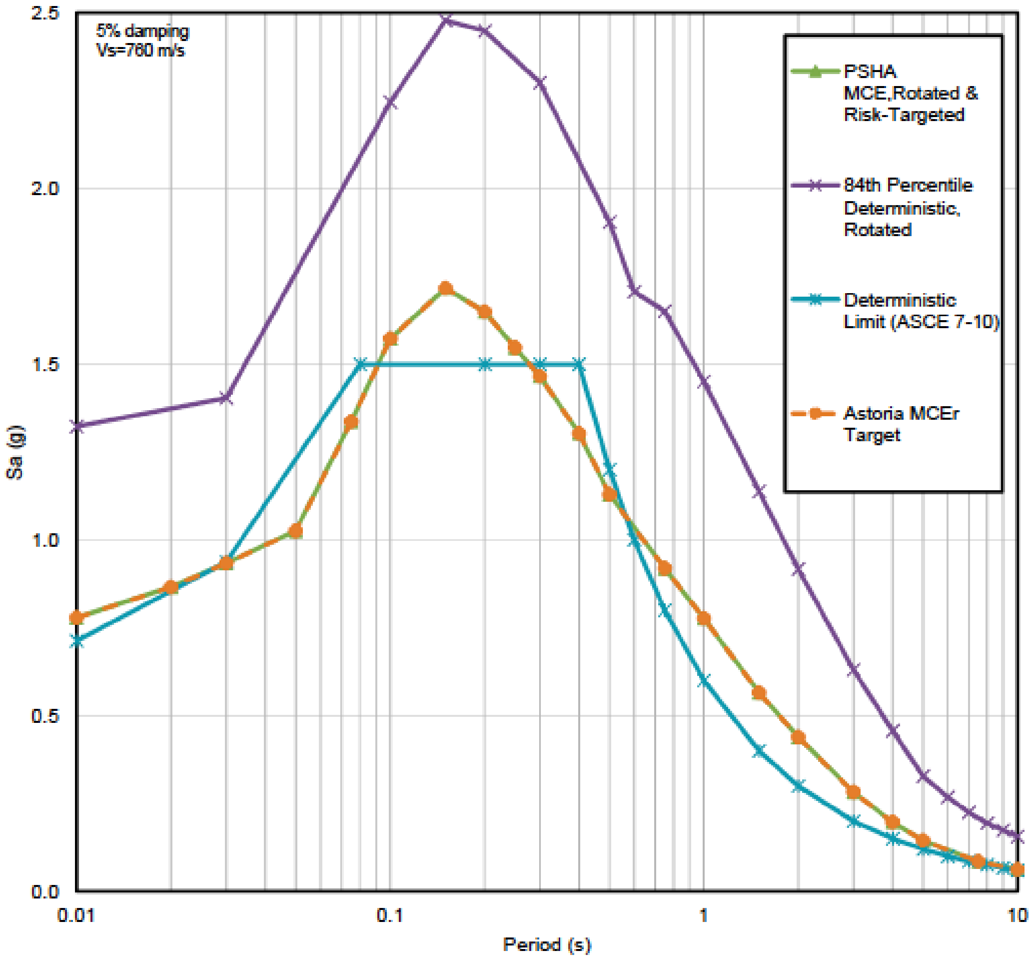

Figure 2-13: Development of the target MCE$_R$ spectrum, per ASCE 7-10, for the Astoria site

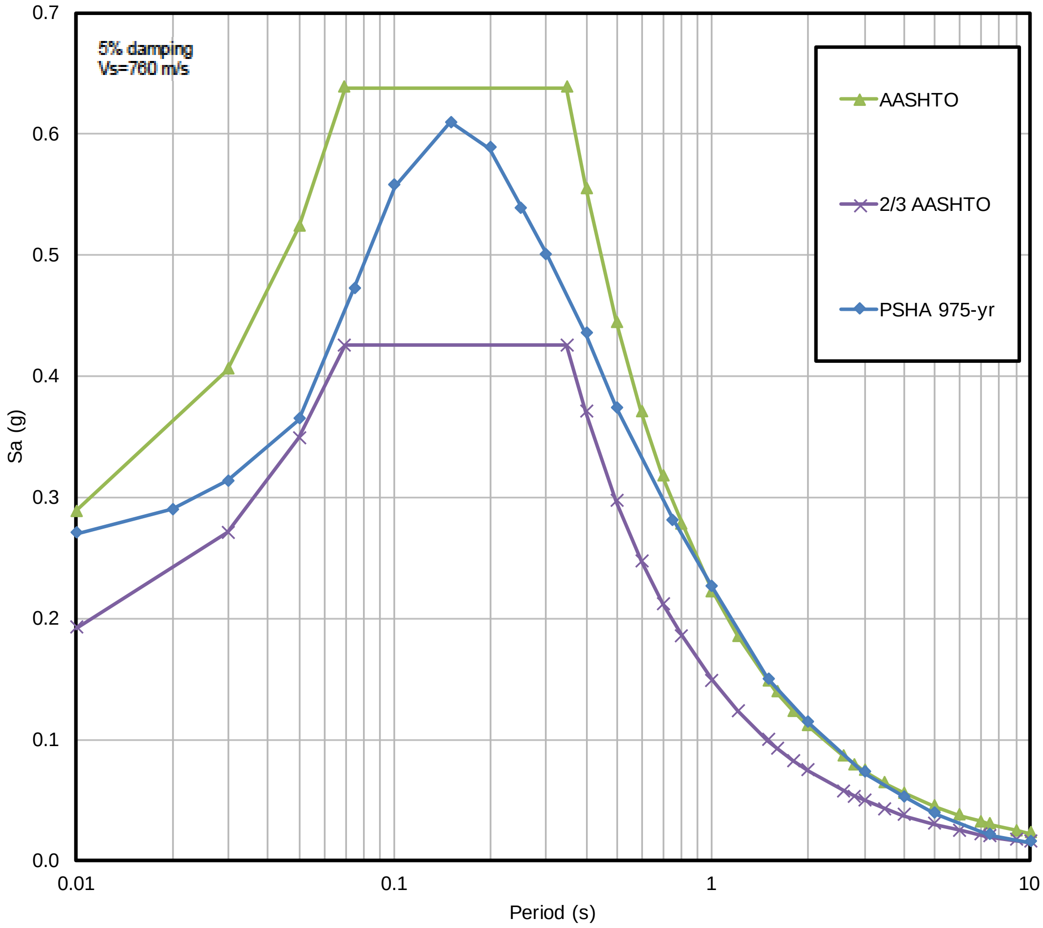

Figure 2-14: Development of the AASHTO LRFD (2014) target spectrum for the Portland site

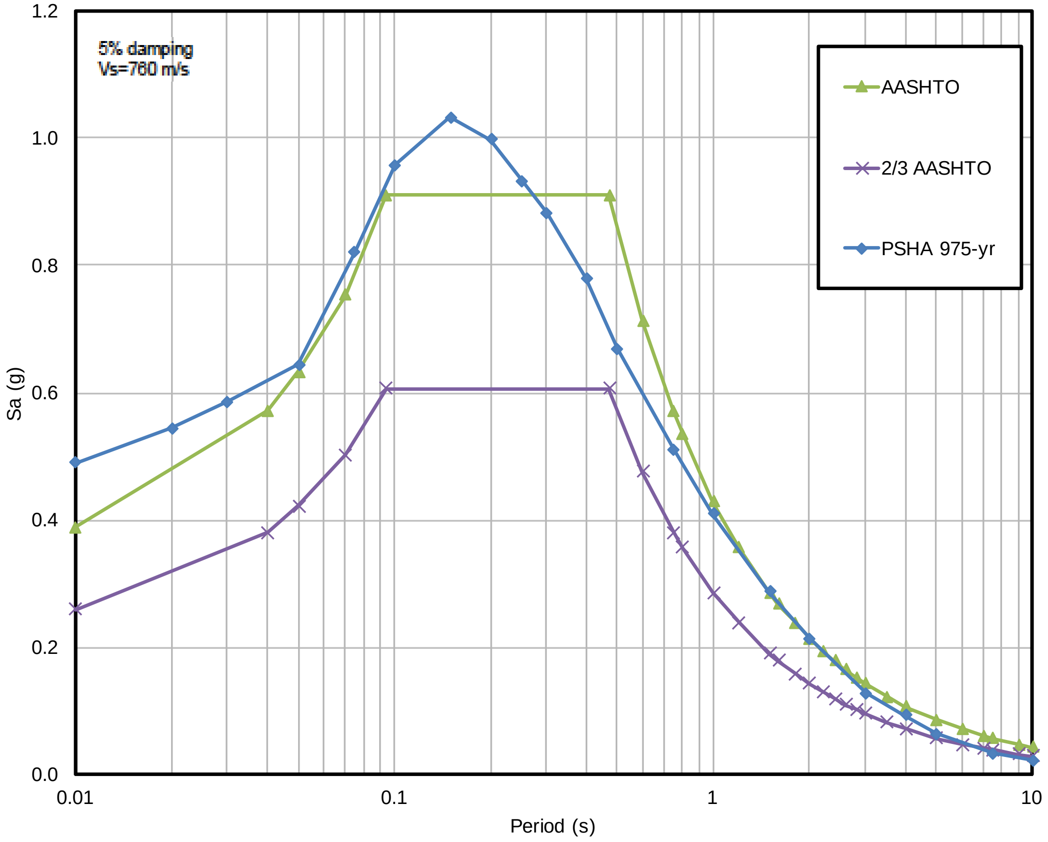

Figure 2-15: Development of the AASHTO LRFD (2014) target spectrum for the Astoria site

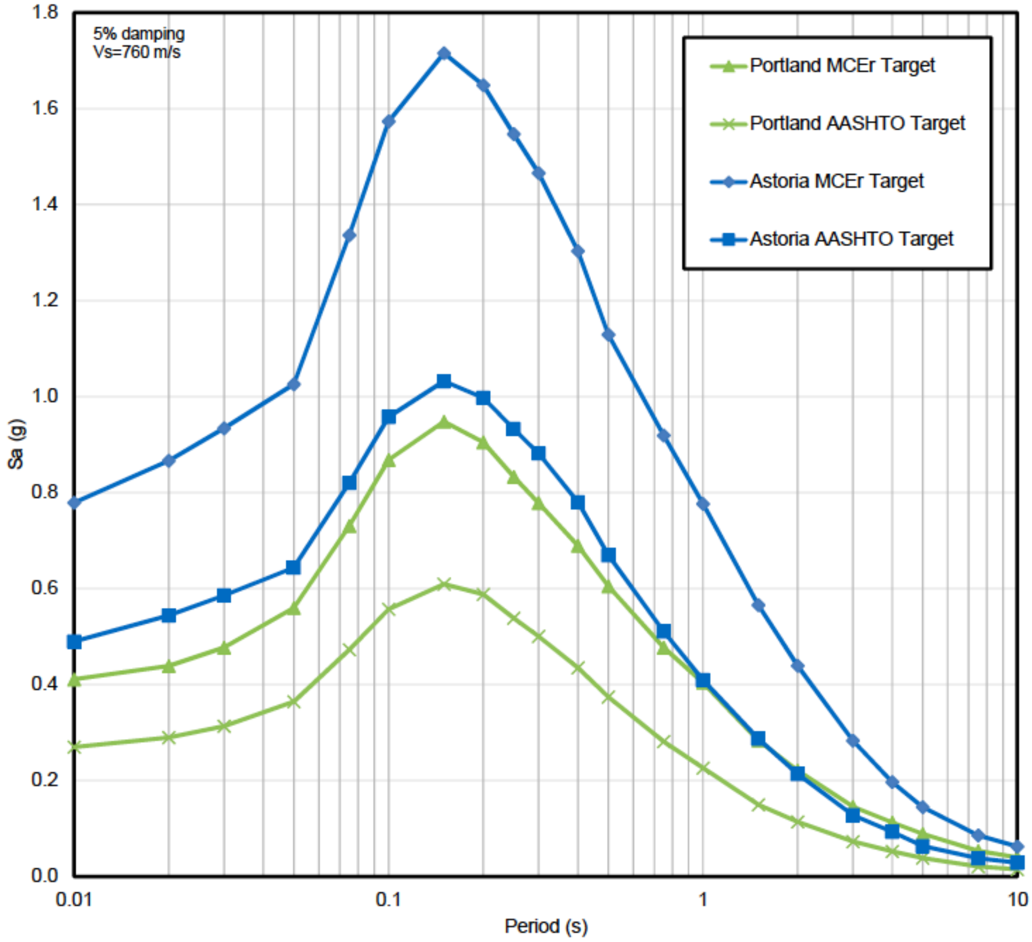

Figure 2-16: Comparison of the target spectra for Portland and Astoria sites

3 GROUND MOTION SELECTION AND MODIFICATION

3.1 Ground motion selection

Seven ground motion records were selected for each site as eventual input to the nonlinear dynamic analyses (NDA). The selection of the ground motion records was based on a multitude of factors, including:

- earthquake magnitude,
- source to site distance,
- site conditions (namely the shear wave velocity in the upper 30-meters - V_{s30}),
- and rupture mechanism (e.g. subduction, reverse, normal, etc.).

The relative proportion of ground motion records chosen to represent each seismic source was based on the USGS deaggregation results discussed in Chapter 2.

As previously mentioned, both sites experience significant hazard contribution from the Cascadia Subduction Zone (CSZ). The characteristic earthquake associated with the CSZ (magnitude 9) would be a historically intense ground motion, meaning that the database of available recordings from similar events is few and far between. This presents a challenge for practitioners in need of multiple large magnitude ground motion records. The relatively recent Tohoku (magnitude 9) and Maule (magnitude 8.8) earthquakes have alleviated the issue to some extent, but the result is that many ground motion suites contain multiple records from these two events and this study is no exception. The use of multiple recordings from the same event is quite common in the Pacific Northwest, and is essentially unavoidable due to the lack of large magnitude events with recorded time histories.

Figures 3-1 to 3-6 show the acceleration, velocity, and displacement time histories of the ground motions that were selected for Portland and Astoria, respectively. The fourteen selected ground motions were eventually modified for compatibility with their respective target spectra. This was accomplished for both sites using the common linear scaling method. In the case of the Portland site, an additional spectral matching routine was performed in addition to the scaling. The following sections provide information regarding the seed ground motions and the modification processes used to generate the target spectrum compatible time histories for NDA input.

3.1.1 Portland

The seven motions that were selected for Portland are shown in Table 3-1, along with their key characteristics. The ground motion records were selected based on the deaggregated hazard data (Table 2-5) and the aforementioned factors, such as site conditions, rupture mechanics, etc. They include four shallow crustal records, two interface subduction records, and one intraplate subduction record. The hazard contribution for the 975-year return period followed a similar breakdown, which allowed for the same ground motion suite to be used for both return periods.

The selection of ground motion records used to represent local crustal events was performed using the PEER NGA-West2 online tool (http://ngawest2.berkeley.edu/). The selection of earthquake records was further refined to account for the probability of pulse motions due to the proximity of the PHF. The method of Hayden et al. (2014) was used to estimate the probability of pulse motions based on the spectral acceleration at a period of 1-second and the epsilon value of the ground motion. The result was that two of the four crustal motions include a velocity pulse, as classified by PEER (2013). The 1989 Loma Prieta earthquake record, taken from the Lexington Dam station, was recorded on the dam abutment. The record was assumed to be representative of a free field recording based on the work of Makdisi et al. (1994).

3.1.2 Astoria

In the case of the Astoria site, the seismic hazard was unsurprisingly dominated by the CSZ megaquake. A summation of various CSZ rupture scenarios accounts for approximately 98% of the hazard for a 2475-year return period at PGA (Table 2-5). The difference in magnitude and distance for the two scenarios is due to the uncertainty involved in modelling the fault rupture mechanisms. Table 3-2 shows the seven selected ground motions that were chosen based on the deaggregation. Two ground motion records from each, Tohoku and Maule, were used due to the previously discussed lack of similar strong motion recordings.

3.2 Ground motion scaling

Linear ground motion scaling is a common method of ground modification in which an acceleration time history is multiplied by a constant factor in order to improve the spectral fit across the structure's period range of interest. The period range of interest is usually taken as 0.2*T to 1.5*T, where T is the fundamental period of the structure, to account for both higher mode response and period lengthening due to inelasticity (NIST 2011). For the single soil-pile system considered in this analysis the fundamental period of the structure can be approximated as 1.4 seconds, as will be shown in the subsequent chapters.

Typically, peaks and valleys in the response spectrum of an individual ground motion make it difficult to adequately scale the record using a constant factor. Bi-modal hazard distributions stemming from different fault mechanisms can further complicate the scaling process because of the different characteristics of the expected motions. For instance, the target spectrum that was derived from the probabilistic hazard analysis at the Portland site is dominated by the PHF at short to intermediate periods and the CSZ at long periods. This means that a single ground motion event is unlikely to produce a response spectrum with the same shape as the target. For this reason, linear scaling of either a subduction or crustal event to match the entire target spectrum can be challenging. It is important to remember that the goal of the scaling process is to obtain an average response across the entire suite of motions that is in line with the target spectrum.

The scale factors used for the ground motions in Portland and Astoria are shown in Tables 3-3 and 3-4, respectively. These scale factors were chosen based on the resulting fit to the target spectrum across the period range of interest and at PGA. While most of the scale factors fall within reasonable limits, it should be noted that the Talagante recording from the 2015 Illapel, Chile earthquake required scale factors greater than 6 to achieve a reasonable fit with the target spectra. Although there is no strict limit regarding the maximum magnitude of scale factors, it is worth recognizing that in this case the scale factors were outside of the preferred range. The resulting scaled spectra are shown, plotted against their respective target spectra in Figures 3-7 to 3-10.

3.3 Ground motion matching

Spectral matching is a ground motion modification procedure in which the frequency content of a seed ground motion is adjusted in order to improve the agreement between the spectral response and target spectrum. While the matching procedure often results in a higher degree of compatibility across the entire target spectrum (relative to linear scaling), it also reduces the variability of the structural response. For the purpose of this study, the reduction of variability was an advantageous consequence because it isolated the differences in structural response solely due to the effects of strong motion duration.

Spectral matching was performed using RspMatch (Al Atik and Abrahamson 2010). Initially, the Portland set of ground motions were matched to the AASHTO target spectrum. The matched set of motions was then linearly scaled to the MCE_R level using a constant factor of 1.7, which corresponds to the ratio of PGA between the MCE_R and AASHTO spectra. A reasonably good fit to the MCE_R target was obtained due to the similarity in shape between the two target spectra. Figures 3-11 to 3-17 show comparisons between the 7 original time histories and their spectrally matched counterparts. Figures 18 and 19 show the resulting matched spectra and their respective targets. Generally, the matched spectra are in good agreement with target spectra and the velocity time histories generally retained their key characteristics

3.4 Tables and Figures

Table 3-1: Ground motions selected for the Portland site and their key characteristics

	Event						
	Tohoku, Japan March 3, 2011	**Maule, Chile February 27, 2010**	**Offshore, El Salv. January 13, 2001**	**Tabas, Iran September 16, 1978**	**Nahanni, Canada December 23, 1985**	**Cape Mendocino, CA April 25, 1992**	**Loma Prieta, CA October 17, 1989**
Station	Tajiri (MYGH06)	Cerro Santa Lucia (STL)	Acajutla Cepa (CA)	Tabas (TAB)	Site 1	Cape Mendocino (CPM)	Los Gatos-Lex. Dam (LEX)
Component	NS	360	90	T1	280	00	90
Magnitude	9.0	8.8	7.7	7.35	6.76	7.01	6.93
Rupture Distance (km)	63.8	64.9	151.8*	2.05	9.6	6.96	5.02
Vs30 (m/s)	593	1411	Intermediate Intrusive Rock	767	605	568	1070
Rupture Mechanism	Subduction (Interface)	Subduction (Interface)	Subduction (Intraslab)	Crustal (Reverse)	Crustal (Reverse)	Crustal (Reverse)	Crustal (Reverse Oblique)
$D_{5\text{-}95}$ (sec)	85.5	40.7	27.2	16.5	7.5	9.7	4.3
PGA(g)	0.27	0.24	0.10	0.87	1.25	1.51	0.41
Pulse	No	No	No	Yes	No	No	Yes

Table 3-2: Ground motions selected for the Astoria site and their key characteristics

	Event						
	Tohoku, Japan March 3, 2011	**Tohoku, Japan March 3, 2011**	**Maule, Chile February 27, 2010**	**Maule, Chile February 27, 2010**	**Mexico City, Mexico September 19,1985**	**Illapel, Chile September 16, 2015**	**Arequipa Peru June 23 2001**
Station	Tajiri (MYGH06)	Matsudo (CHB002)	Cien Agronomicas (ANTU)	Cerro Santa Lucia (STL)	La Union (UNIO)	Talagante (TAL)	Moquegu (MOQ)
Component	NS	NS	NS	360	N00W	90	NS
Magnitude	9.0	9.0	8.8	8.8	8.0	8.3	8.4
Rupture Distance (km)	63.8	356.0*	64.6	64.9	83.9*	140.9	76.7
Vs30 (m/s)	593	325**	621	1411	Meta-Andesite Breccia	1127	573
Rupture Mechanism	Subduction (Interface)	Subduction (Interface)	Subduction (Interface)	Subduction (Interface)	Subduction (Interface)	Subduction (Interface)	Subducti (Interfac
D_{5-95} (sec)	85.5	47.1	38.5	40.7	24.2	76.4	36.0
PGA(g)	0.27	0.29	0.23	0.24	0.17	0.065	0.22

Table 3-3: Scale factors for the Portland ground motions

	Event						
	Tohoku, Japan March 3, 2011	**Maule, Chile February 27, 2010**	**Offshore, El Salv. January 13, 2001**	**Tabas, Iran September 16, 1978**	**Nahanni, Canada December 23, 1985**	**Cape Mendocino, CA April 25, 1992**	**Loma Prieta, CA October 17, 1989**
MCEr Scale Factor	1.38	1.85	3.61	0.51	0.42	0.32	1.11
AASHTO Scale Factor	0.86	1.16	2.26	0.32	0.26	0.2	0.69

Table 3-4: Scale factors for the Astoria ground motions

	Event						
	Tohoku, Japan March 3, 2011	**Tohoku, Japan March 3, 2011**	**Maule, Chile February 27, 2010**	**Maule, Chile February 27, 2010**	**Mexico City, Mexico September 19,1985**	**Illapel, Chile September 16, 2015**	**Arequipa Peru June 23, 2001**
MCEr Scale Factor	2.35	3.00	2.75	3.00	4.50	10.20	3.10
AASHTO Scale Factor	1.40	1.60	1.80	1.80	2.75	6.50	1.90

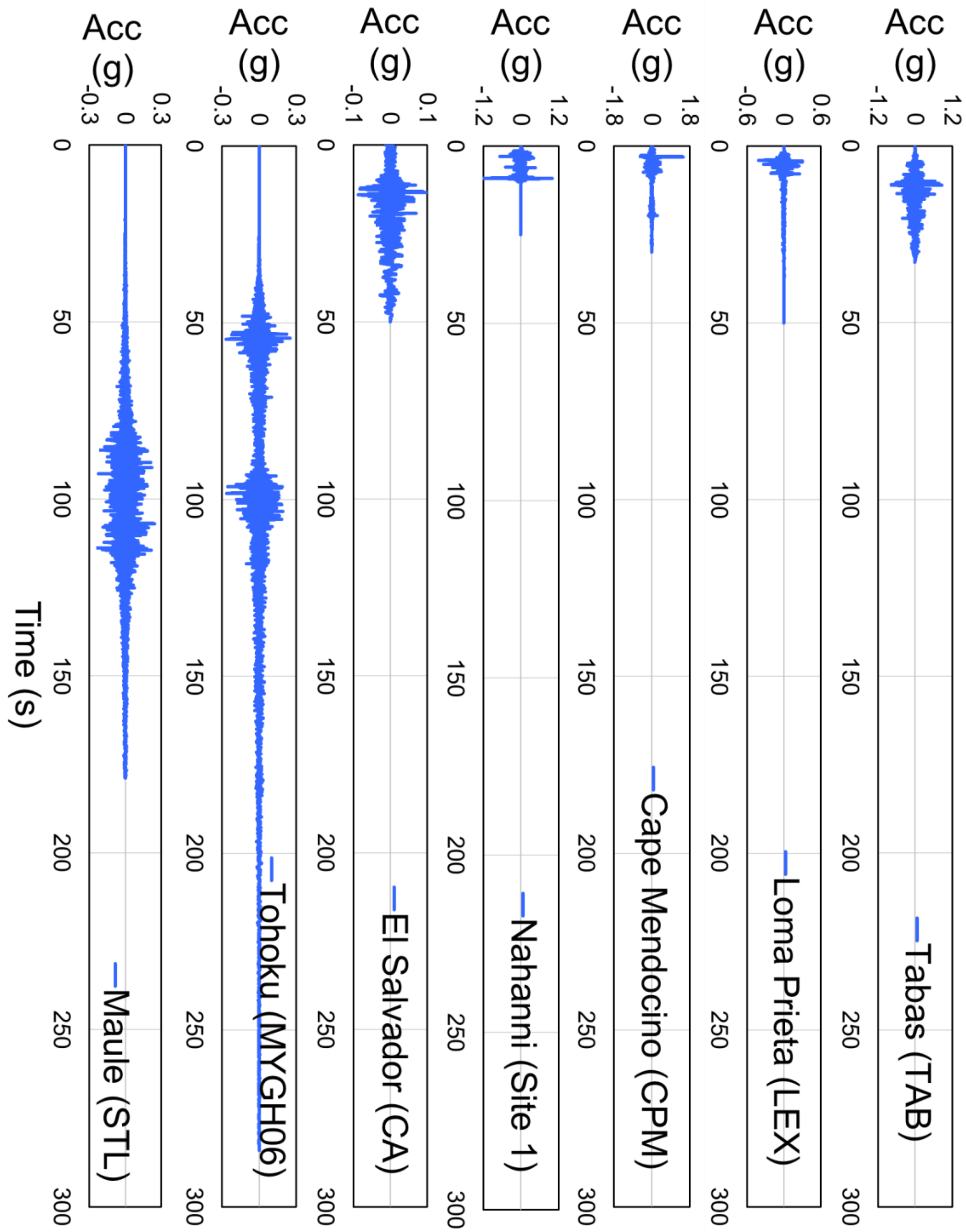

Figure 3-1: Unscaled acceleration time histories of the 7 ground motions selected for Portland

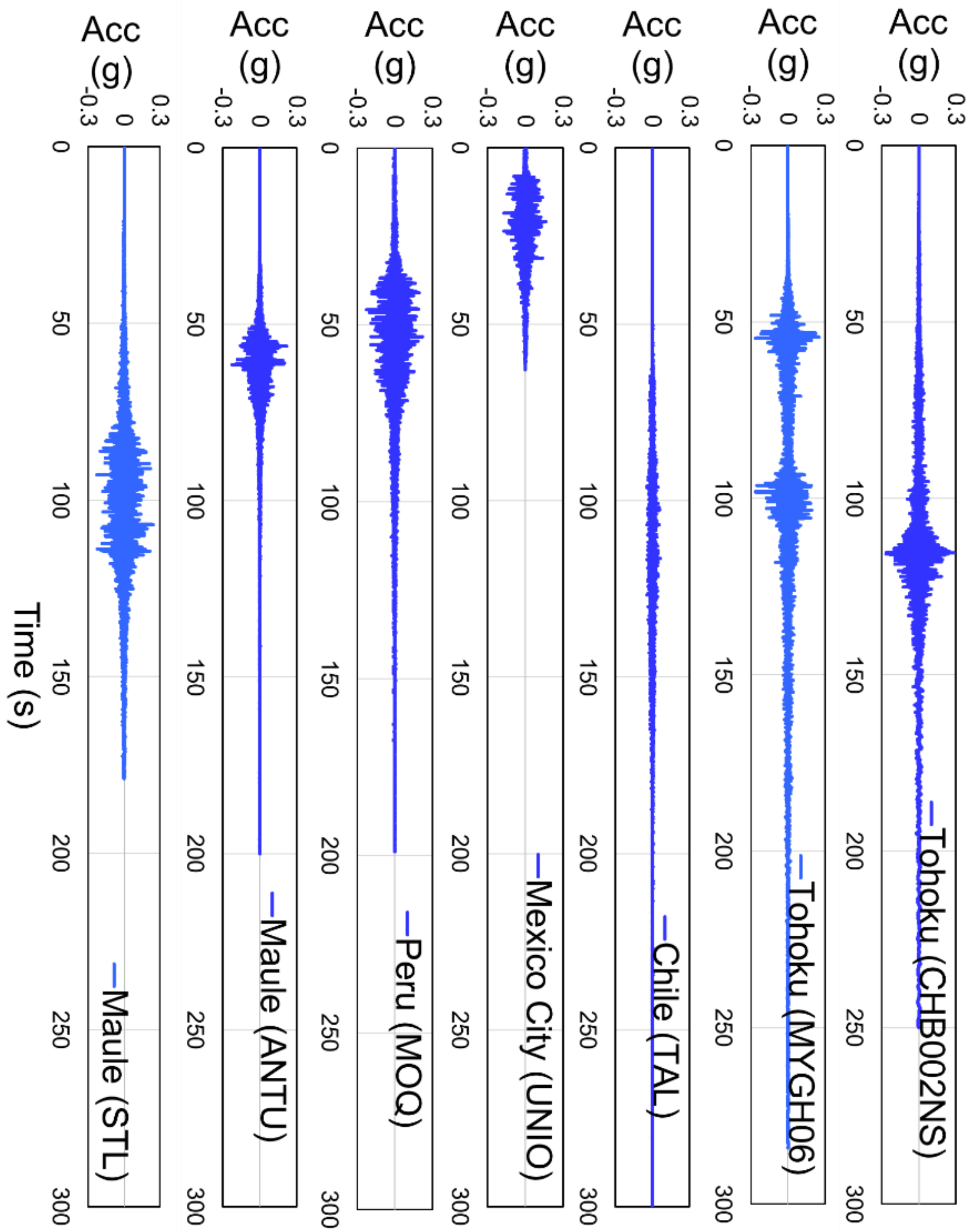

Figure 3-2: Unscaled acceleration time histories of the 7 ground motions selected for Astoria

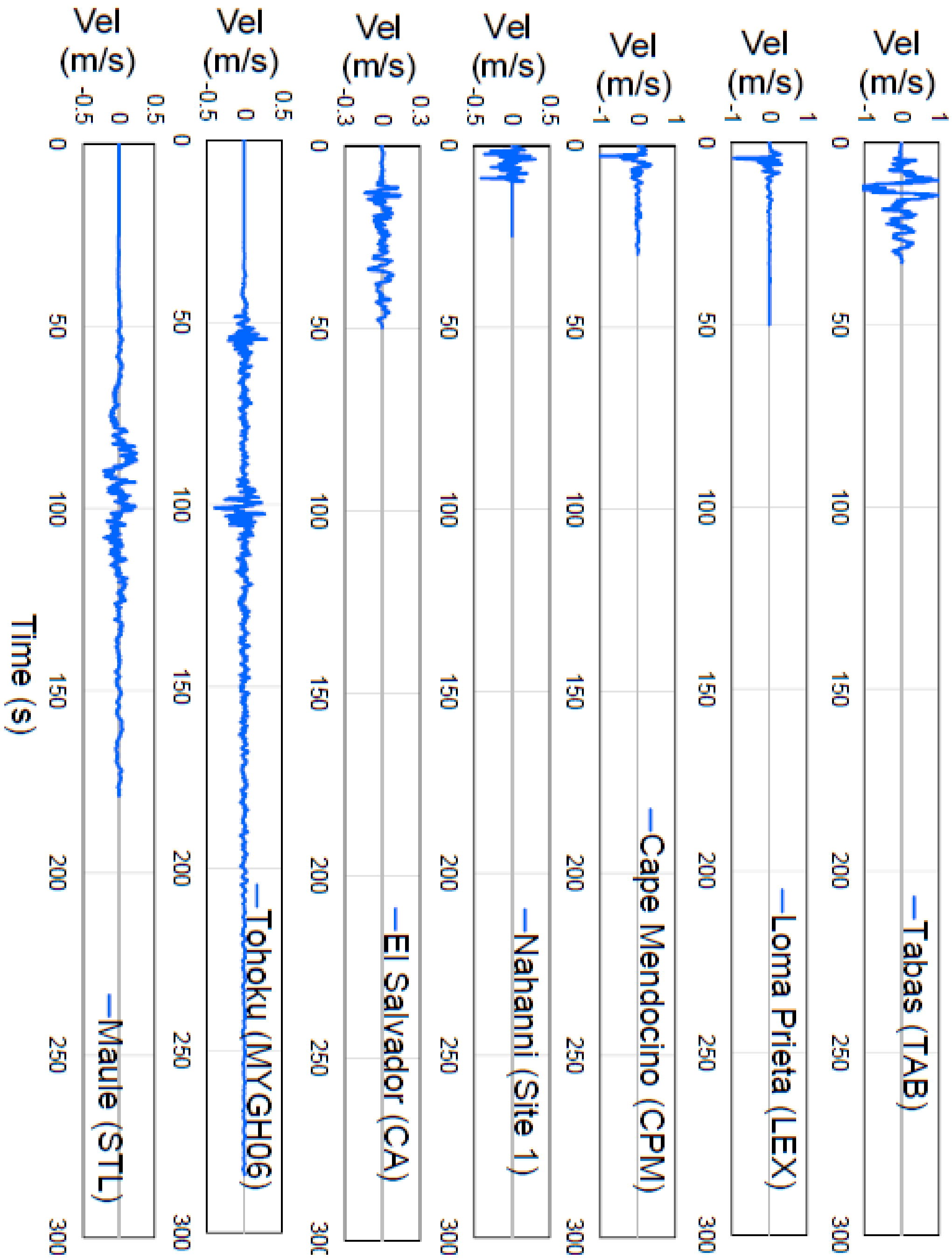

Figure 3-3: Unscaled velocity time histories of the 7 ground motions selected for Portland

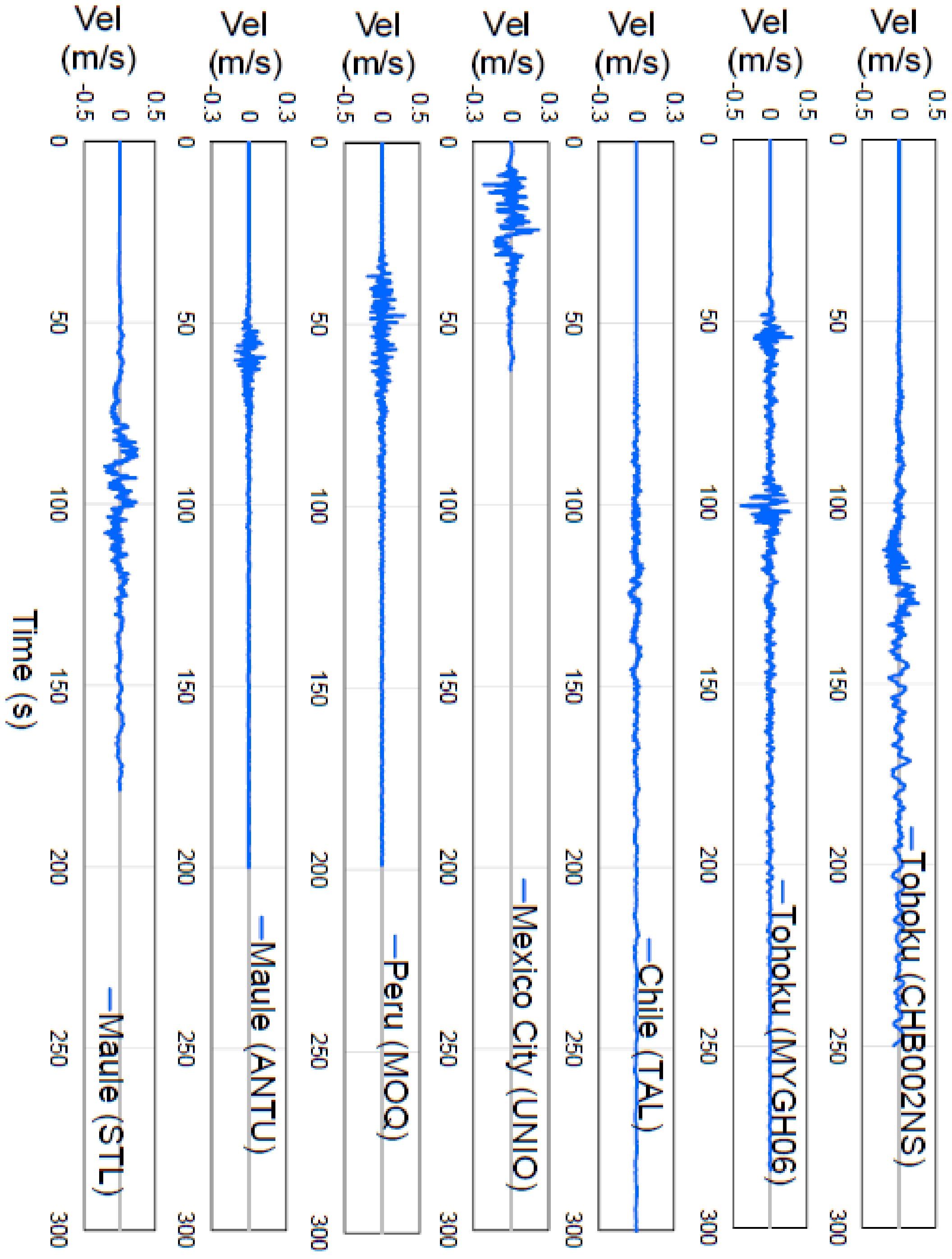

Figure 3-4: Unscaled velocity time histories of the 7 ground motions selected for Astoria

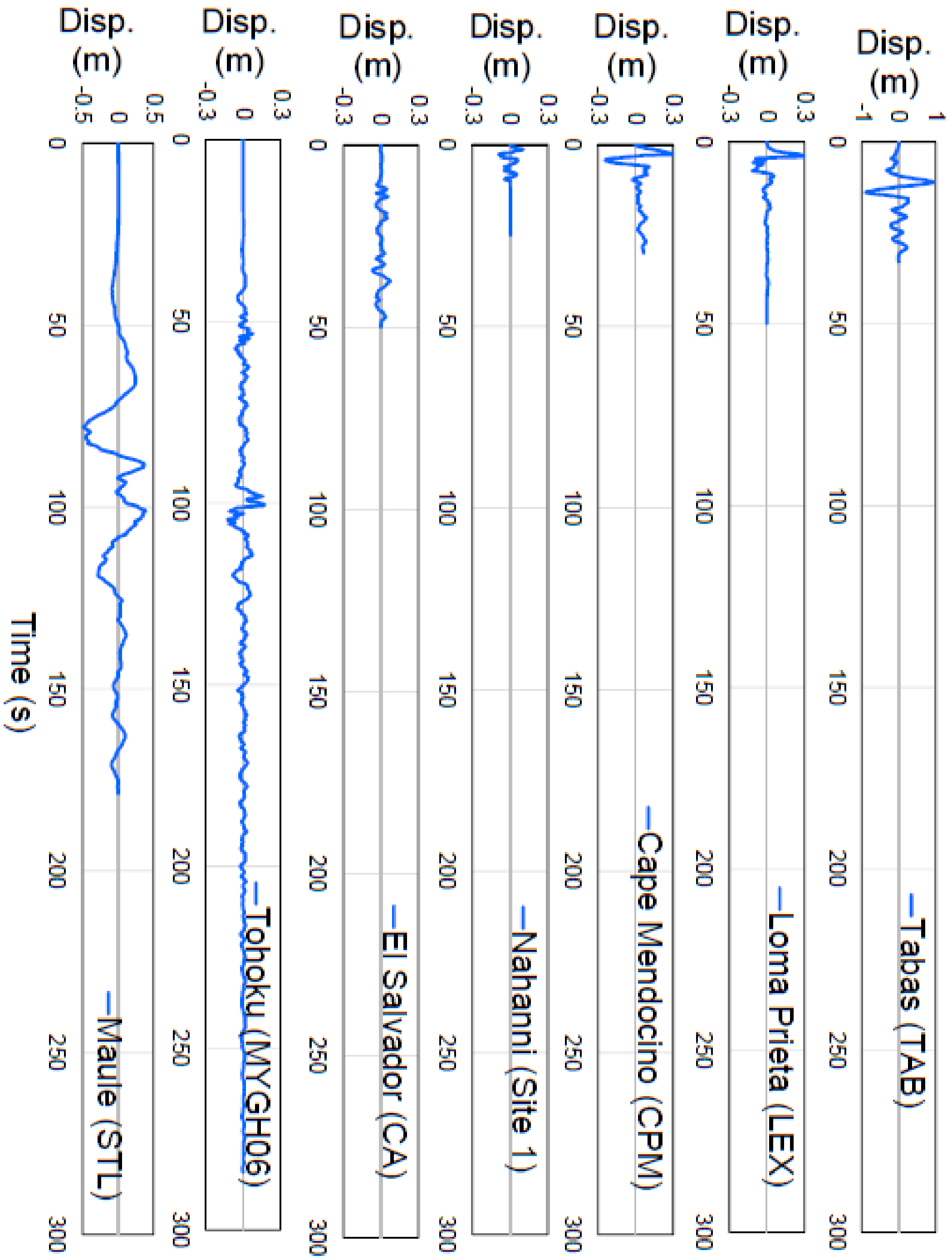

Figure 3-5: Unscaled displacement time histories of the 7 ground motions selected for Portland

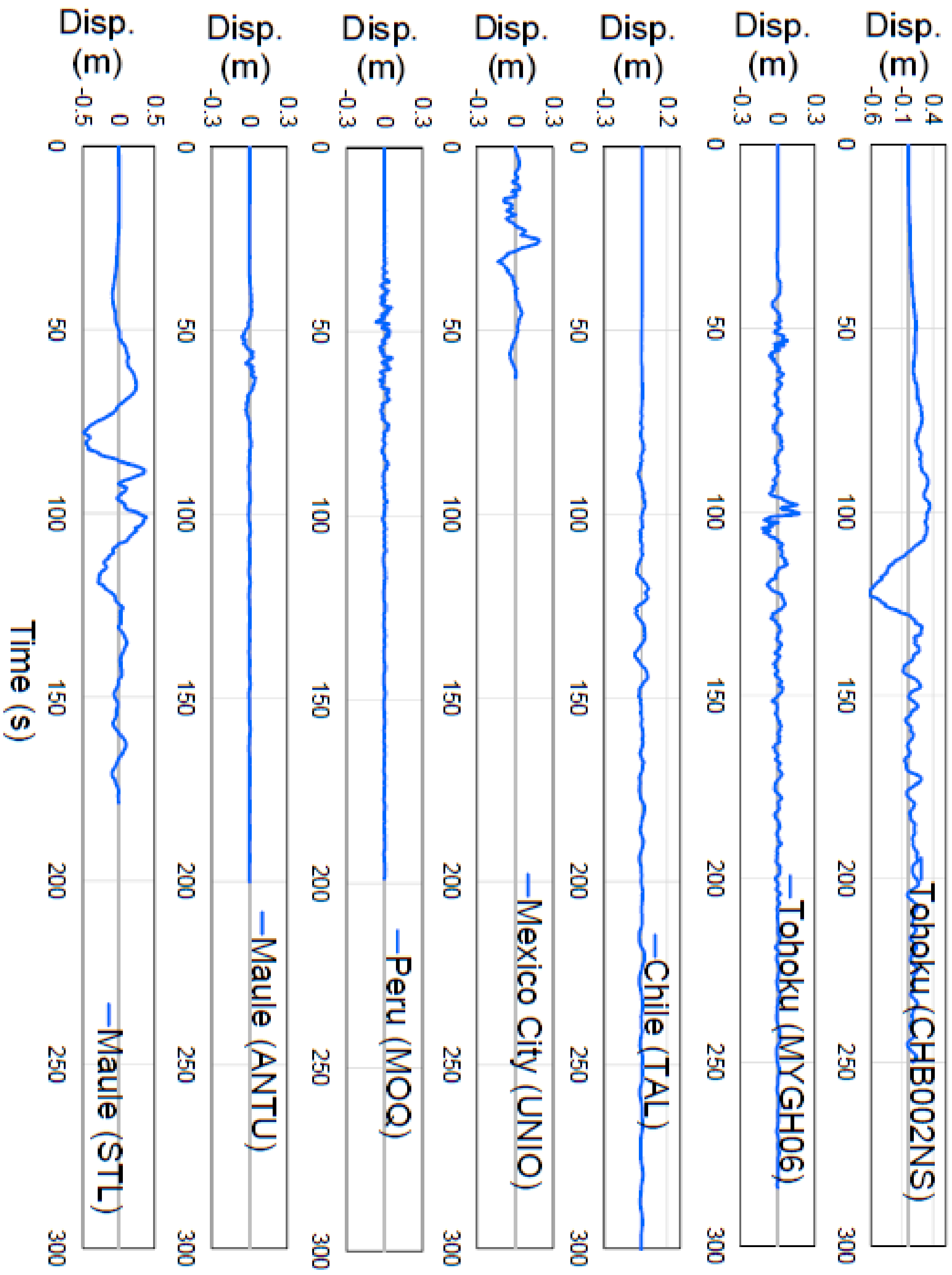

Figure 3-6: Unscaled displacement time histories of the 7 ground motions selected for Astoria

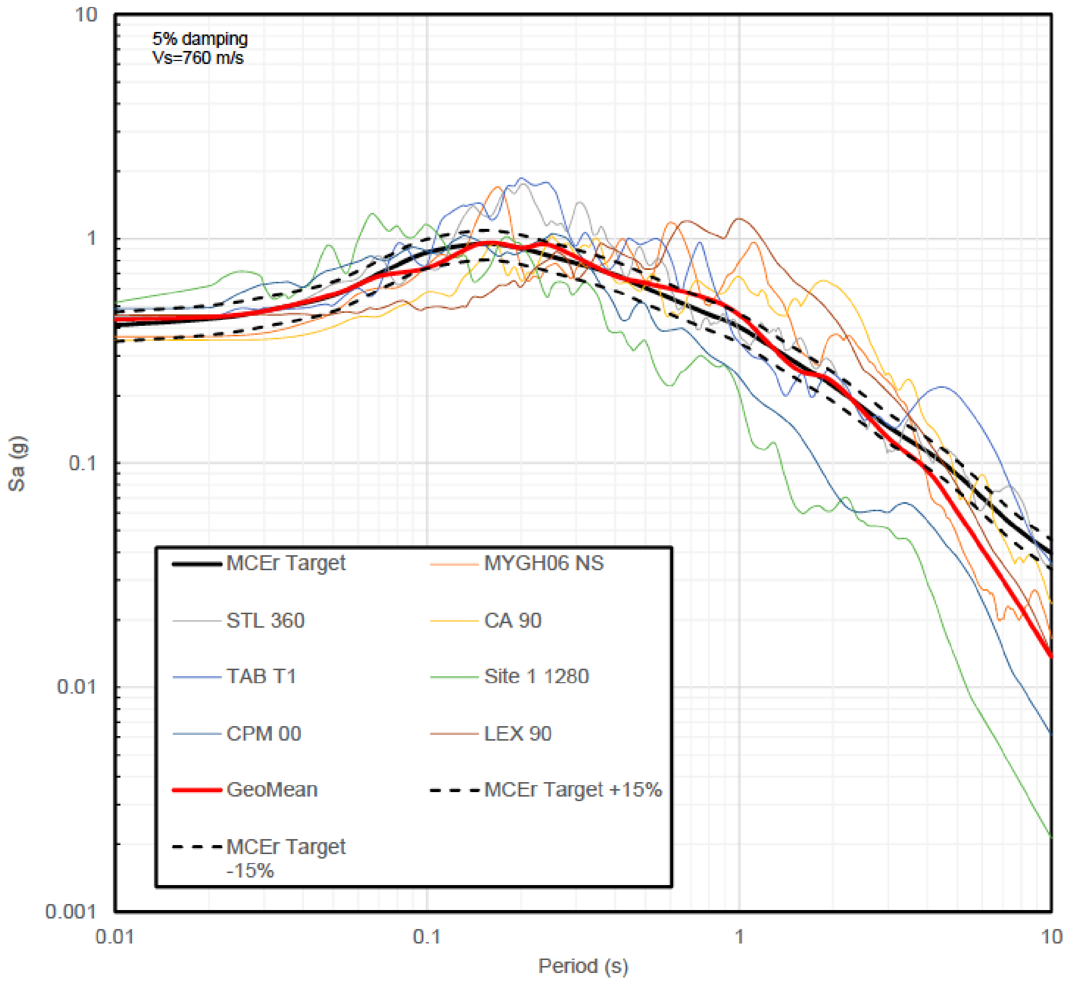

Figure 3-7: Individual ground motion spectra scaled to the MCER target spectrum at the Portland site

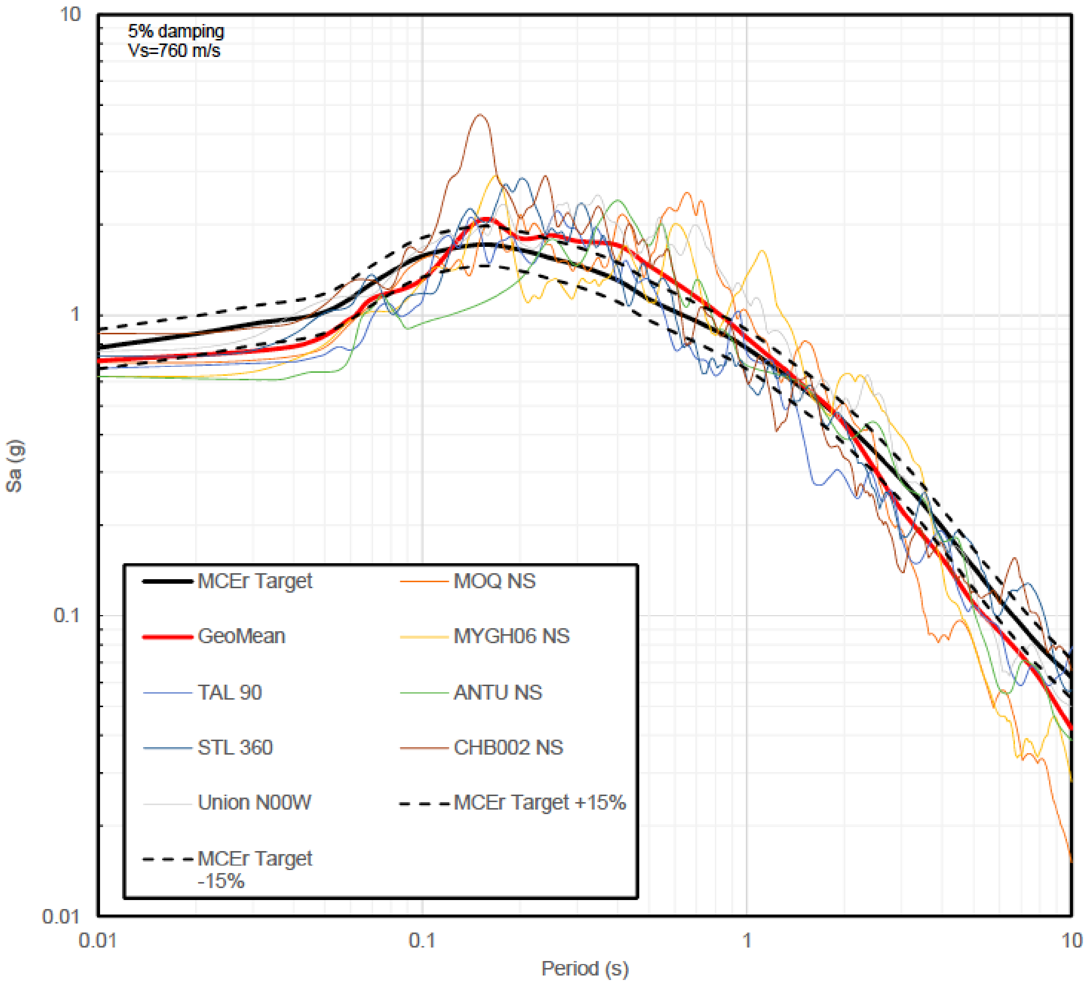

Figure 3-8: Individual ground motion spectra scaled to the MCE$_R$ target spectrum at the Astoria site

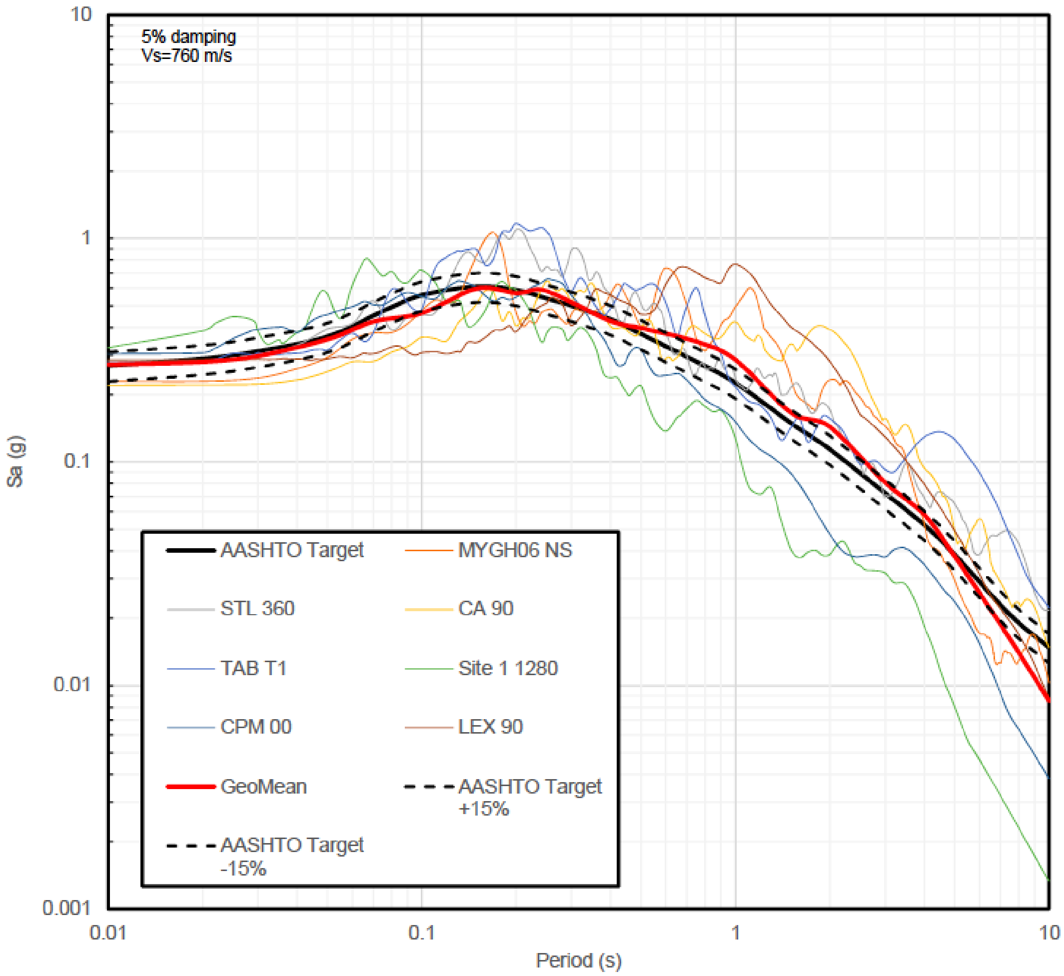

Figure 3-9: Individual ground motion spectra scaled to the AASHTO target spectrum at the Portland site

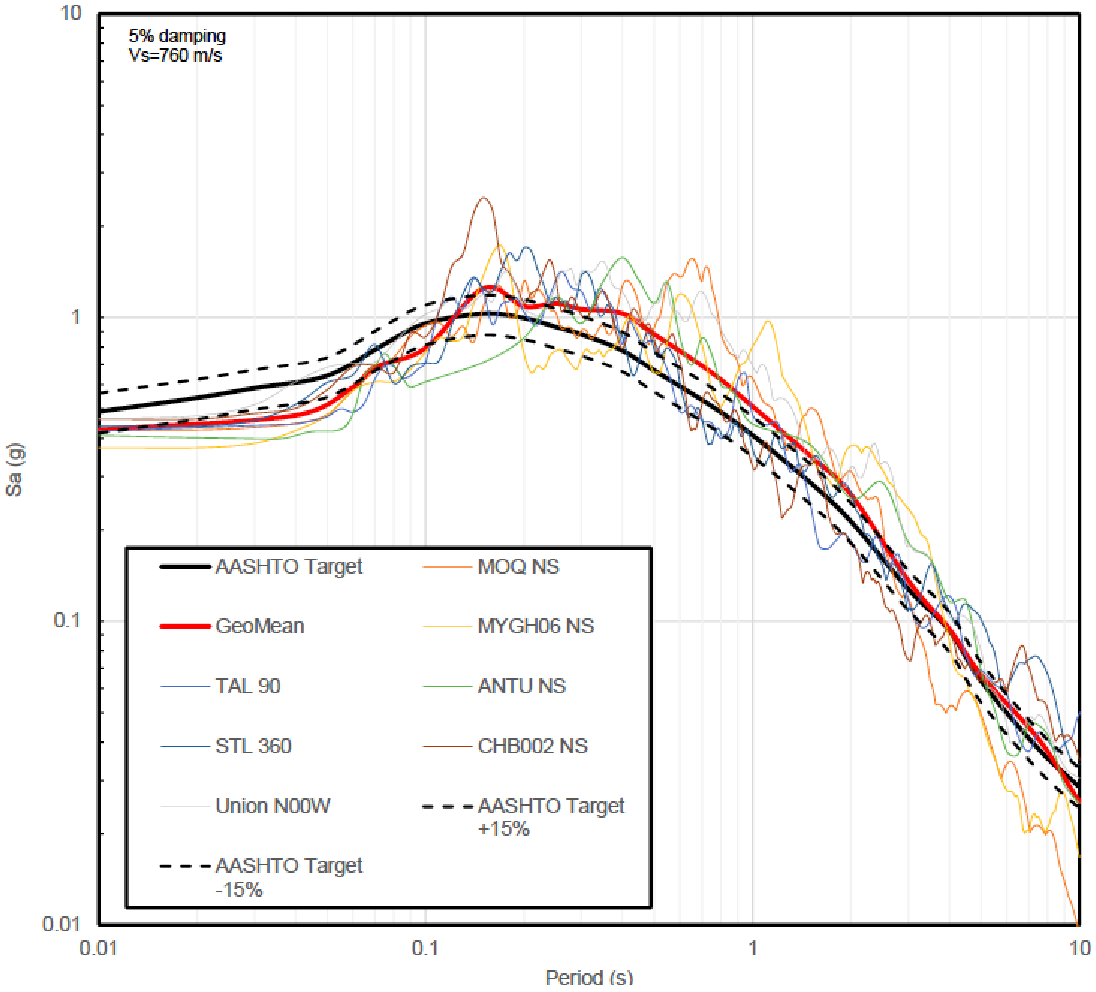

Figure 3-10: Individual ground motion spectra scaled to the AASHTO target spectrum at the Astoria site

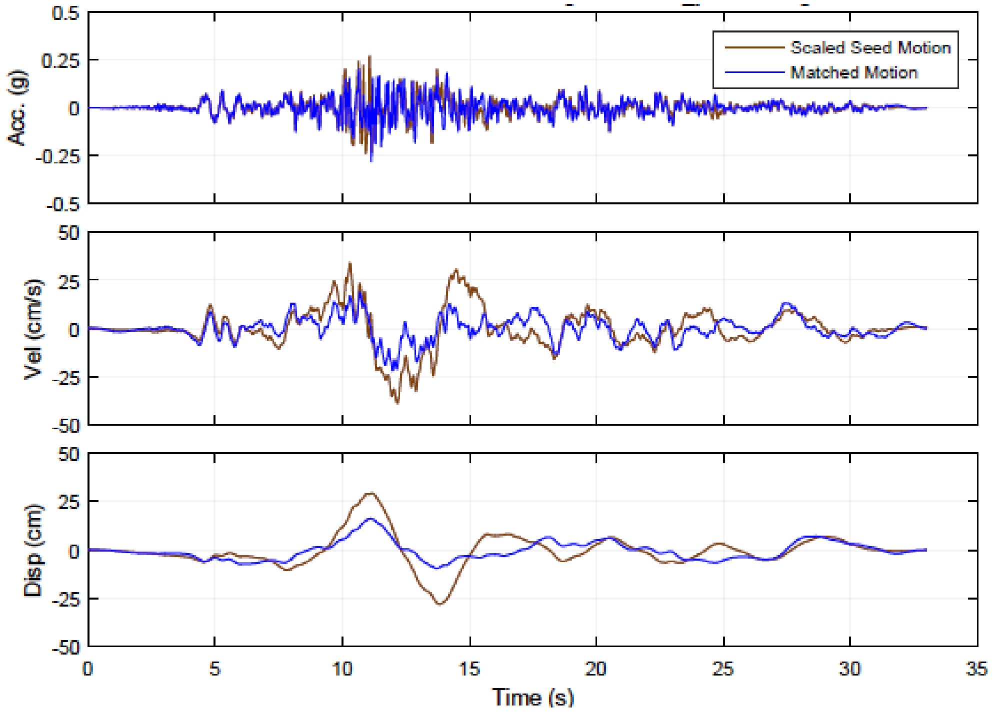

Figure 3-11: Comparison of original and matched motions for the 1978 Tabas earthquake at the Tabas station (component T1) at the Portland-AASHTO level

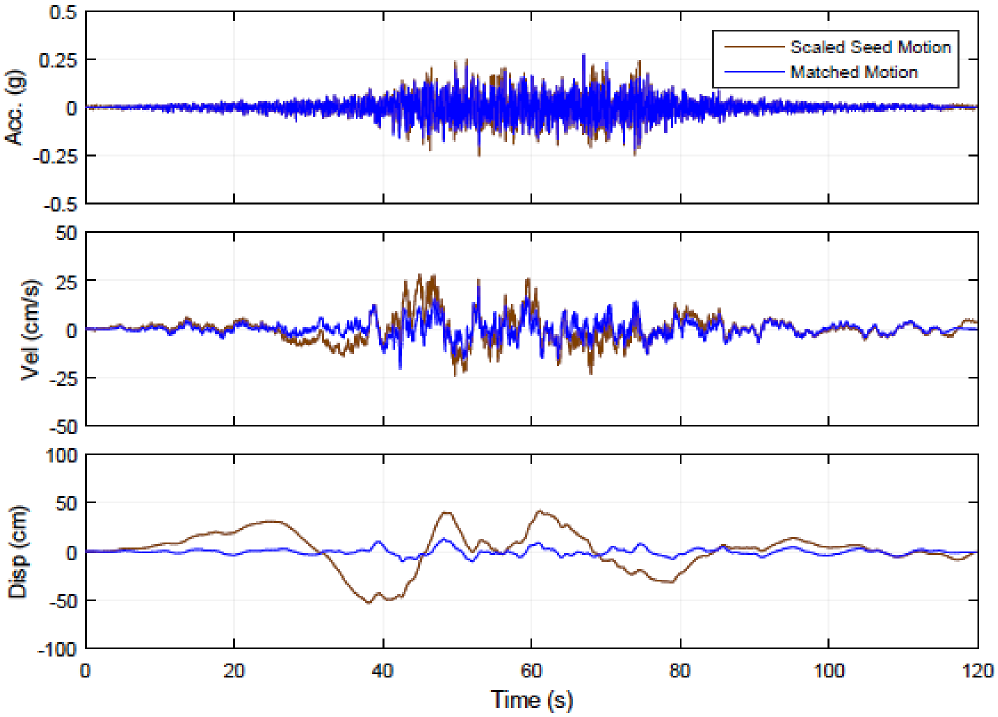

Figure 3-12: Comparison of original and matched motions for the 2010 Maule earthquake at the Cerro Santa Lucia station (component 360) at the Portland AASHTO level

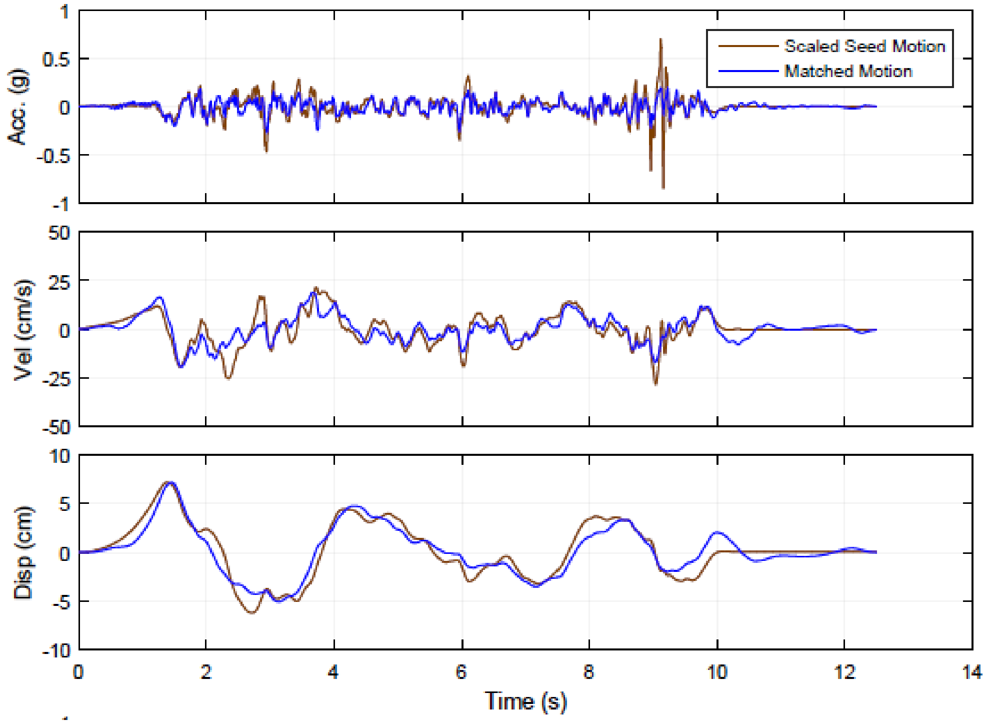

Figure 3-13: Comparison of original and matched motions for the 1985 Nahanni earthquake at the Site 1 station (component 280) at the Portland AASHTO level

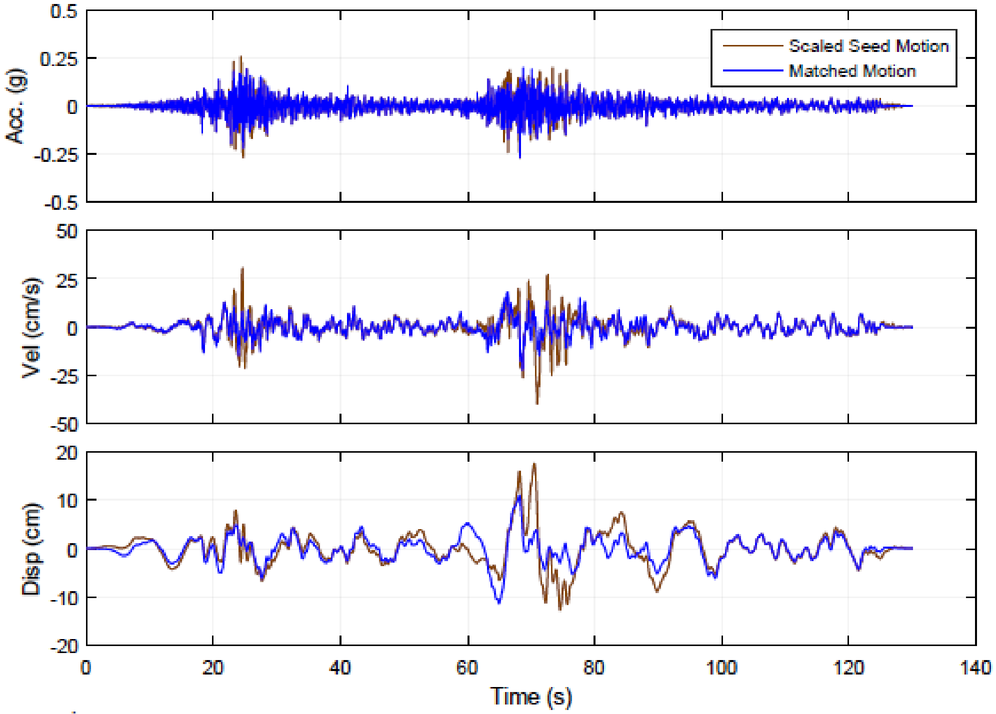

Figure 3-14: Comparison of original and matched motions for the 2011 Tohoku earthquake at the Tajiri station (component NS) at the Portland AASHTO level

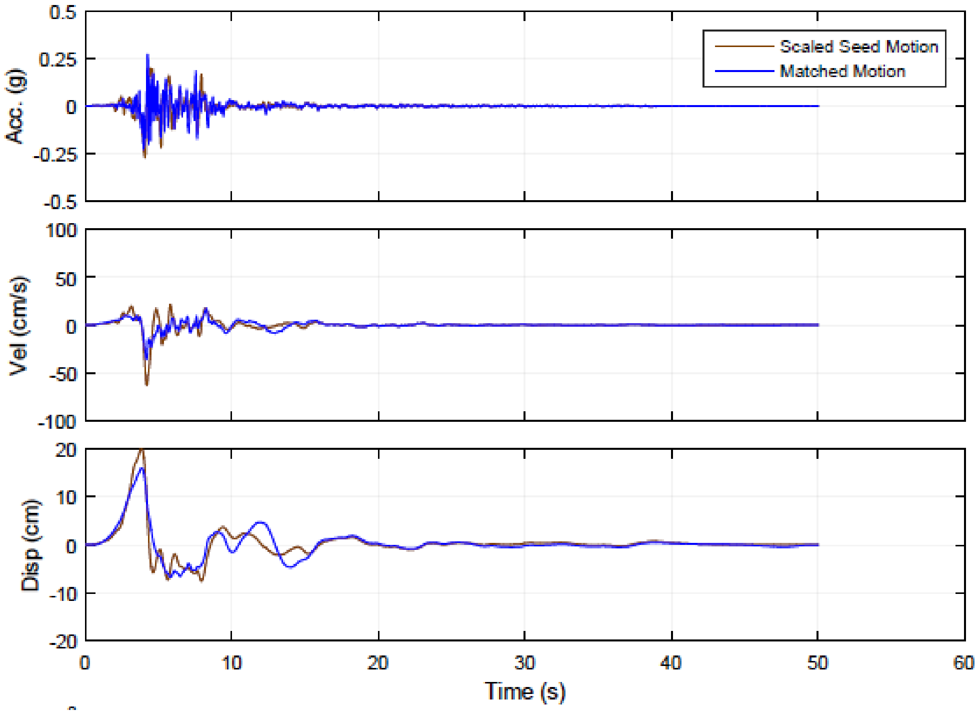

Figure 3-15: Comparison of original and matched motions for the 1989Loma Prieta earthquake at the Lexington Dam station (comp 90) at the Portland AASHTO level

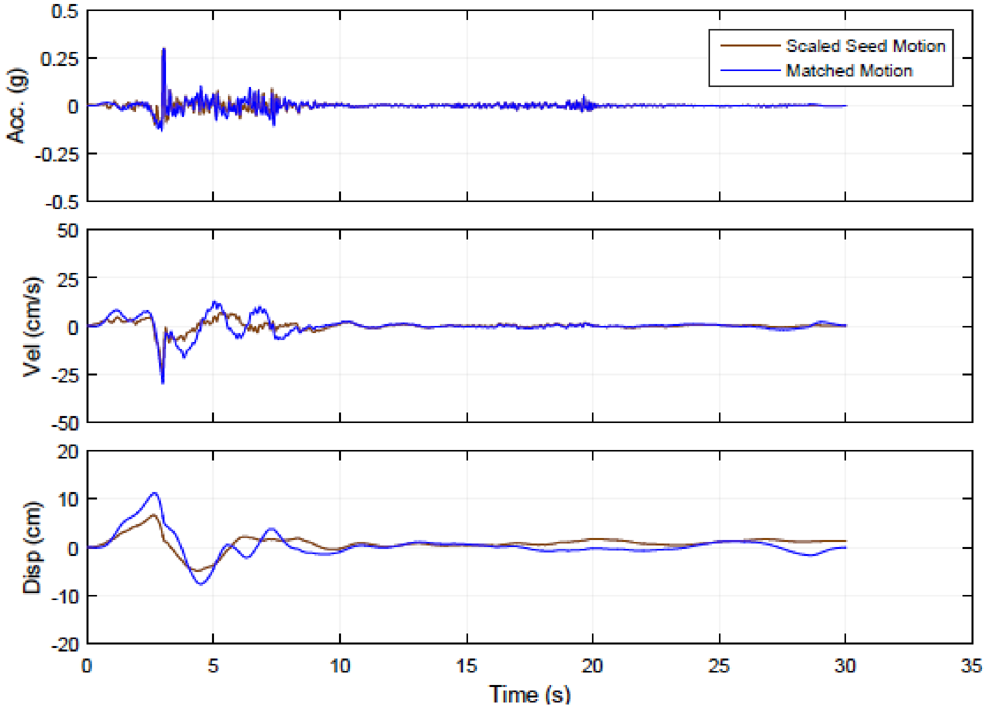

Figure 3-16: Comparison of original and matched motions for the 1992 Cape Mendocino earthquake at the Cape Mendocino station (component 00) at the Portland AASHTO level

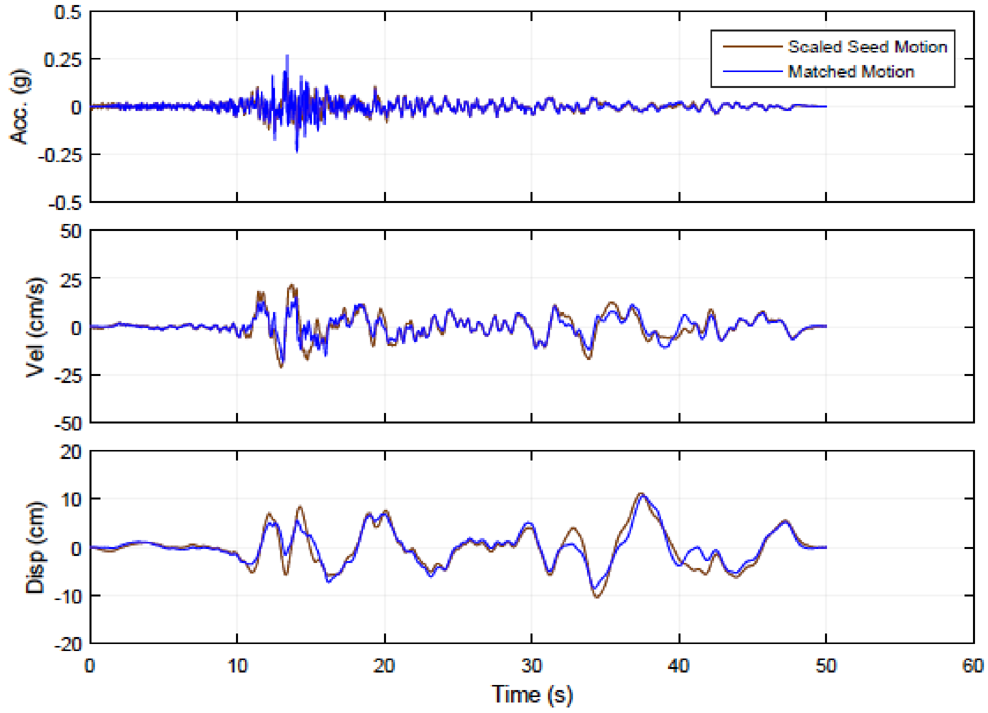

Figure 3-17: Comparison of original and matched motions for the 2001 El Salvador earthquake at the Acajutla Cepa station (component 90) at the Portland AASHTO level

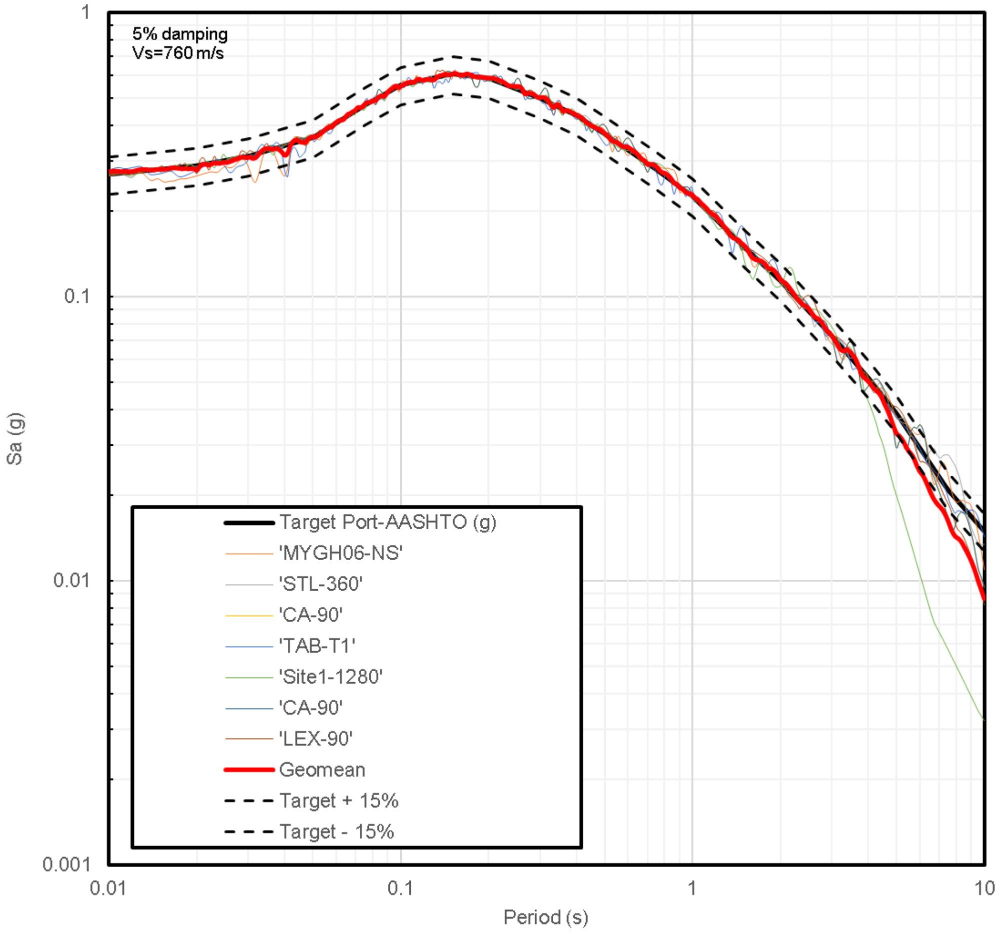

Figure 3-18: Individual ground motion spectra matched to the AASHTO target spectrum for the Portland site

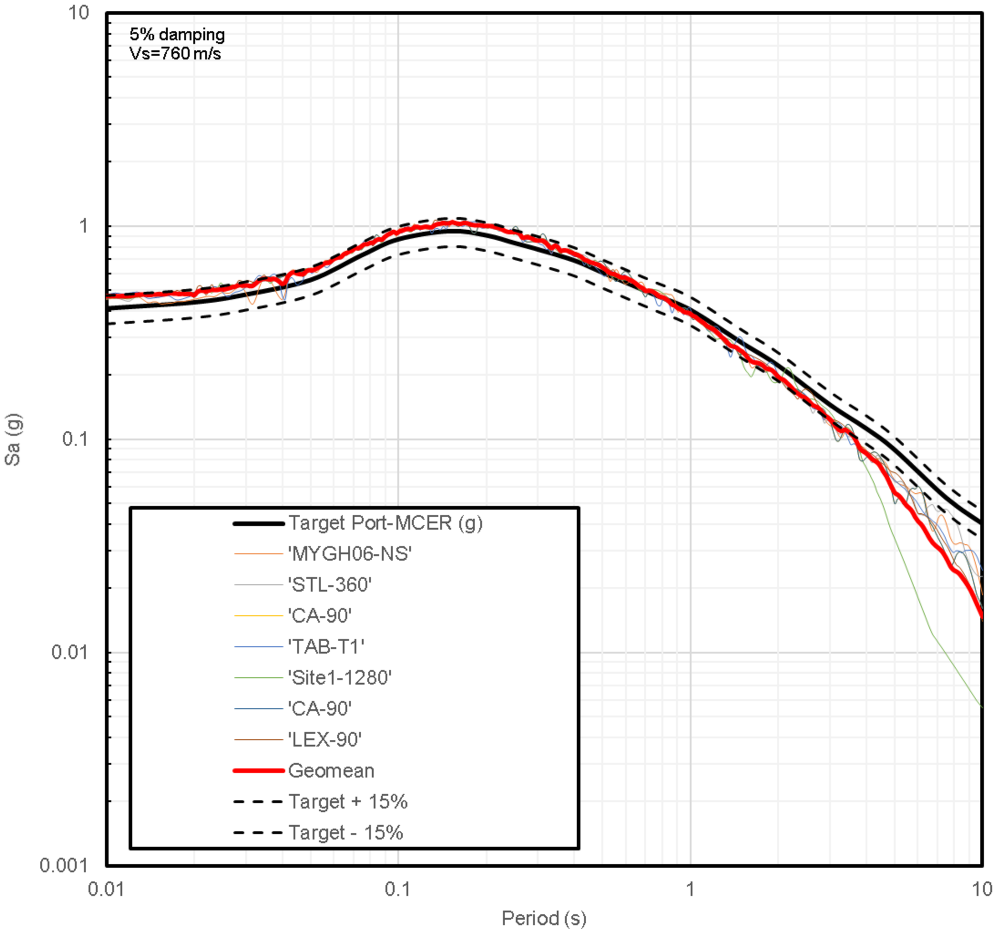

Figure 3-19: Individual ground motion spectra, originally matched to the AASHTO target at the Portland site, scaled by a factor of 1.7 to the MCEr level

4 NONLINEAR DYNAMIC ANALYSIS (NDA)

4.1 Background

This chapter focuses on providing a broad overview of the finite element (FE) model used to perform the nonlinear dynamic analyses (NDA), the cases that were considered in our analyses, and a summary of the NDA output. The numerical model employed in this study was largely based on the model developed by Khosravifar et al. (2014), with a few minor modifications. While some discussion of the model details and calibration is presented herein, a more detailed explanation regarding the technical merits of the model is provided by Khosravifar et al. (2014).

4.2 Finite Element Model

A two-dimensional (2-D) finite element (FE) model was created in the OpenSees framework. (Mazzoni et al. 2009).

The model consists of three main parts (Figure 4-1):

i. a 2-D soil column representing the far-field soil behavior,

ii. a reinforced concrete (RC) pile shaft, and

iii. interface elements (i.e. soil springs) that connect the RC pile and soil column.

The advantages of modelling in 2-D versus 3-D include faster computational times and simplified pre-and post-processing of results. The 3-D effect of soil flowing around the pile is approximated in the 2-D model through the use of the soil springs (p-y curves). These springs allow for large relative displacements between the soil and the pile. For this reason, the 2-D model is expected to provide a reasonable approximation of the 3-D behavior of laterally spreading soil around the pile. Finally, the numerical modelling approach used in this study has been shown to capture pore-water pressure build up, liquefaction triggering, post-liquefaction accumulation of shear strains in the liquefied soil, first order interaction between piles and liquefied soil, and timing/phasing of critical load combinations reasonably well (Khosravifar et al. 2014).

The dynamic analyses (NDA) were performed for two conditions: (1) liquefied sloped-ground condition, and (2) nonliquefied level-ground condition where pore-water pressure generation was precluded. In the liquefied sloped-ground condition, a static shear stress was applied to the soil model to simulate 10% ground slope ($\alpha = 0.1$). The following sections provide additional discussion regarding individual components of the model, as well as a representative dynamic response from FE model, and a summary of the NDA results.

4.2.1 Soil elements

The soil profile consists of a 5-meter thick clay crust (Su=40 kPa), over a 3-meter thick loose sand layer ($(N_{1)60}$=5), over a 12-meter thick dense sand layer ($(N_{1)60}$=35). The soil was modeled using the Pressure-Dependent-Multi-Yield (PDMY02) constitutive model for sand and the Pressure-Independent-Multi-Yield (PIMY) for clay, in conjunction with the 9-4-Quad-UP elements (Yang et al. 2003). Figure 4-2 presents a generic depiction of the PDMY02 model behavior. The 9-4-Quad-UP elements have 9 nodes with translational degrees-of-freedom (DOF) and 4 pore-water pressure DOF. The soil elements were discretized into heights of 0.5m. The soil column was assigned a large thickness (500-meters) to preclude the effects of soil-pile reactions on the site response, thus capturing the free-field soil behavior (Khosravifar et al. 2014).

The primary focus of the calibration process was to capture liquefaction triggering and post-liquefaction accumulation of shear strains based on empirical or mechanics-based correlations by Idriss and Boulanger (2008). Figures 4-3 and 4-4 show the shear modulus, damping ratio reduction curves, and a simulated cyclic direct simple shear test on the loose ($(N_{1)60}$=5) sand. The PIMY model, used for the clay layer, was calibrated based on the shear modulus and damping ratio curves of Vucetic and Dobry (1991) for a clay with a plasticity index of 35. Table 4-1 shows the parameters that were used to model each soil layer. In the nonliquefaction cases, pore-water pressure generation in the PDMY02 model was suppressed by adjusting contraction and dilation parameters so that shear modulus and equivalent damping ratio behavior was unaffected (Khosravifar et al. 2014).

4.2.2 Structural elements

The RC pile was 2-meters in diameter with 20-meter embedment and 5-meter height above the ground. Pile element lengths were set at 0.5-meters. The pile head to superstructure connection was free to rotate. The RC shaft was modeled using fiber sections and nonlinear-beam-column elements with nonlinear stress-strain behavior for reinforcing steel, confined concrete, and unconfined concrete (Figure 4-5). This model is capable of capturing the nonlinear behavior of RC piles and the formation of a plastic hinge at any depth. Figure 4-6 shows the moment-curvature response of the RC shaft.

The concrete compressive strength (f'c) was equal to 44.8-MPa. The superstructure dead load was modeled as a 7-MN lumped mass, corresponding to an axial load ratio (f'c*Ag) of approximately 5%. The longitudinal steel ratio of the RC column was 2%. The steel bars were modeled with a yield strength of 475-MPa, an elastic modulus of 200-GPa, and a strain hardening ratio of 3%.

4.2.3 Interface elements

The soil-pile interface was simulated using p-y, t-z, and q-z soil springs to model lateral, side-friction, and end-bearing interface behavior, respectively. The spring spacing was set at 0.5-meters. This value was refined enough so that pile response was unaffected (Khosravifar et al. 2014). The soil-springs used to model the clay were based on the Matlock (1970) p-y curves (Figure 4-7), while the soil-spring parameters for the sand layers were selected based on guidance from API (2000).

A special type of py and tz springs were used in the liquefied layer (implemented as PyLiq and TzLiq in OpenSees) where the strength and stiffness of the springs change in proportion to the excess-pore-water pressure ratio in the adjacent soil element (Figure 4-8). These models have proven to be effective in capturing the first-order effects of liquefaction during dynamic analyses (Brandenberg et al. 2013). A transition zone of 1 pile diameter in length was implemented for the soil-springs above the dense sand layer and below the clay layer, to model the weakening effect that the liquefied layer exerts on the overlying and underlying nonliquefied layers (Yang and Yeremic 2002)

4.2.4 Ground motion

The input ground motions consisted of the 14 records that were selected and modified as described in Chapter 3 (total of 42 individual cases). The ground motions were applied as a shear stress at the base of the soil column, following the compliant base procedure described by Mejia and Dawson (2006). The dashpot coefficient was based on the mass density and shear wave velocity (760 m/s) of the bed rock half-space.

4.2.5 Solution Scheme

The FE solution scheme used the KrylovNewton solution algorithm and the β-Newmark transient integrator with the constant acceleration scheme. Rayleigh. damping of 0.5% at frequencies of 0.3 to 5 Hz was used for the soil column and 2% at the same frequencies for the RC shaft. The Rayleigh damping in soil was used to account for small-strain damping and to reduce numerical “noise.” Viscous radiation dashpots of p-y springs were assigned damping coefficients of $4\rho DV_s$. The V_s value used to calculate the damping coefficient was computed as 10% of the pre-earthquake value to account for strain softening of the soil column under earthquake loading.

4.2.6 Representative Dynamic Response

An example set of representative NDA results for one ground motion are provided in Figure 4-9. The input motion used in the example is the 2010 Maule earthquake (STL station) scaled to the AASHTO design spectrum developed for the Portland site (PGA = 0.27 g). This is a subduction earthquake with a significant duration, $D_{5\text{-}95}$, of 40.7 seconds. The time of maximum pile head displacement (0.17-meter downslope) is marked by a vertical dashed line in Figure 4-9. At the time of maximum pile head displacement, the superstructure inertia is 75% of its maximum and the lateral spreading force (crust load) is 70% of its maximum. Note that at this time, liquefaction has already triggered (ru=100%) and the lateral spreading load has almost fully mobilized. The relative displacement between soil and pile is 0.35 meters; 0.4 meters of relative displacement is required to fully mobilize the passive force in the clay crust.

4.3 Results

The relevant NDA results are presented in the following sections as it pertains to either the site response portion of the analysis or the structural response of the pile. It is important to remember that FE model was capable of modelling both aspects of interest (the geotechnical and structural response) simultaneously and the results are merely presented in this manner for clarity.

4.3.1 Site response analysis

The site response results for nonliquefied level ground and liquefied sloped ground (α=0.1) for each site, and for both ground motion levels, is presented in Figures 4-10 to 4-15 by plotting the spectral amplification ratios (SAR). The SAR in this case is computed as the spectral acceleration recorded at the ground surface of the soil column relative to the spectral acceleration of the bedrock input motion (outcrop). In general, the site response results showed:

- deamplification at short structural periods in the nonliquefied case due to the large ground motion intensity and nonlinear soil behavior,
- pronounced deamplification at short and intermediate structural periods in the liquefied case due to liquefaction induced soil softening, and

- for any given site and hazard level, the maximum SAR was controlled by the nonliquefied case up to a structural epriod of about 2 seconds, at which point the liquefied case usually began to control the SAR envelope.

Lateral soil displacements were also of particular interest because of their effect on the magnitude of passive pressure exerted on the RC shaft. The ground surface displacement values were computed relative to the displacements at the base of the soil column and were residual values (i.e. end of ground motion). The displacement profiles in all of the liquefied cases followed the same general pattern. The displacement was negligible through the dense sand layer and then linearly increased through the liquefied layer to its maximum value where it remained at a maximum through the clay crust. In the nonliquefied case, maximum recorded soil displacements were negligible and the displacement profiles varied in an unpredictable manner. As an example, Figure 4-16 shows a representative set of soil displacement profiles fort the Portland set of ground motions matched to the AASHTO target spectrum.

Note that approximately 0.4-meters of relative soil-pile displacement was required to mobilize full passive pressure of the clay crust. Of the 42 different cases that were analyzed under liquefied conditions, only 5 cases did not result in enough relative ground surface displacement to mobilize the full passive pressure; all 5 cases involved crustal motions at the Portland site. Figures 4-17 and 4-18 provide a comparison of the relative ground surface displacements for all of the ground motion scenarios.

4.3.2 Structural response

Figures 4-19 and 4-20 show the maximum relative superstructure displacements that occurred during each ground motion scenario. The displacements were computed as the maximum pile head displacement at any time during the ground motion relative to the base of soil column. As expected, the superstructure displacements increase, for any given ground motion, when (1) the ground motion intensity is greater (i.e. MCE_R level versus AASHTO) and (2) the effects of liquefaction are included.

Figure 4-21 shows aggregated NDA results from all 42 input motions. The figure compares the maximum pile head displacements between liquefied sloped-ground conditions (combined inertial and kinematic demands) and nonliquefied level-ground conditions (inertia only). The fact that all pile demands are larger in the liquefied condition compared to the nonliquefied condition indicates that demands cannot be enveloped by merely accounting for the effects of inertia only or lateral spreading only (i.e. treating them separately). This finding is contrary to the recommendations of MCEER/ATC (2003) that suggests designing piles for the envelope of inertia and kinematics separately. Furthermore, these findings are aligned with the results of other recent studies such as Tokimatsu et al. (2005), Boulanger et al. (2007), Caltrans (2012), and Khosravifar et al. (2014).

The spectral response of the superstructure was also recorded during the NDA. Figure 4-22 shows the nonliquefied SAR curves for the Portland site at the MCE_R and AASHTO levels. The structural period of the system can be approximated from these curves as 1.4-seconds in the nonliquefied condition. This value compared favorably with the structural period obtained from the pushover curve, as described in the subsequent chapter.

4.4 Tables and Figures

Table 4-1: Soil parameters used in the FE model (Khosravifar et al. 2014)

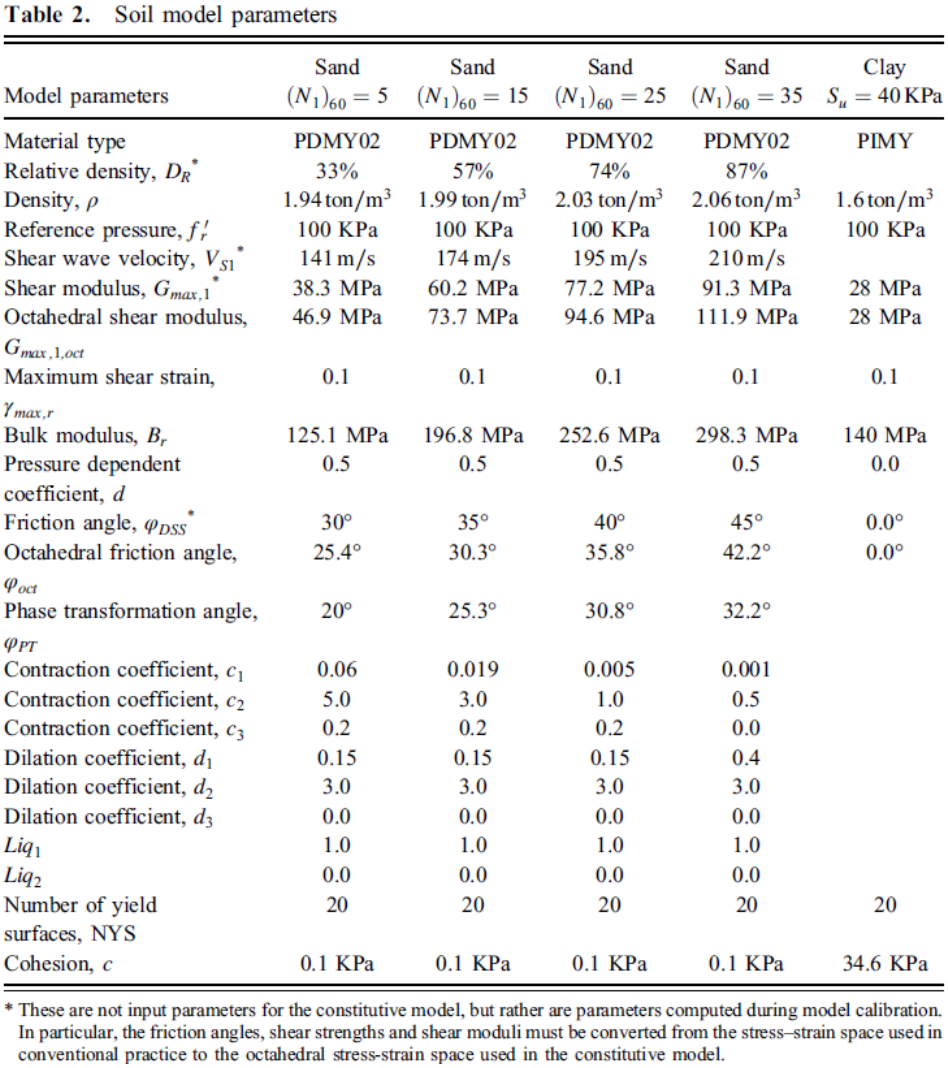

Table 2. Soil model parameters

Model parameters	Sand $(N_1)_{60} = 5$	Sand $(N_1)_{60} = 15$	Sand $(N_1)_{60} = 25$	Sand $(N_1)_{60} = 35$	Clay $S_u = 40$ KPa
Material type	PDMY02	PDMY02	PDMY02	PDMY02	PIMY
Relative density, D_R*	33%	57%	74%	87%	
Density, ρ	1.94 ton/m^3	1.99 ton/m^3	2.03 ton/m^3	2.06 ton/m^3	1.6 ton/m^3
Reference pressure, f_r'	100 KPa	100 KPa	100 KPa	100 KPa	100 KPa
Shear wave velocity, V_{S1}*	141 m/s	174 m/s	195 m/s	210 m/s	
Shear modulus, $G_{max,1}$*	38.3 MPa	60.2 MPa	77.2 MPa	91.3 MPa	28 MPa
Octahedral shear modulus, $G_{max,1,oct}$	46.9 MPa	73.7 MPa	94.6 MPa	111.9 MPa	28 MPa
Maximum shear strain, $\gamma_{max,r}$	0.1	0.1	0.1	0.1	0.1
Bulk modulus, B_r	125.1 MPa	196.8 MPa	252.6 MPa	298.3 MPa	140 MPa
Pressure dependent coefficient, d	0.5	0.5	0.5	0.5	0.0
Friction angle, φ_{DSS}*	30°	35°	40°	45°	0.0°
Octahedral friction angle, φ_{oct}	25.4°	30.3°	35.8°	42.2°	0.0°
Phase transformation angle, φ_{PT}	20°	25.3°	30.8°	32.2°	
Contraction coefficient, c_1	0.06	0.019	0.005	0.001	
Contraction coefficient, c_2	5.0	3.0	1.0	0.5	
Contraction coefficient, c_3	0.2	0.2	0.2	0.0	
Dilation coefficient, d_1	0.15	0.15	0.15	0.4	
Dilation coefficient, d_2	3.0	3.0	3.0	3.0	
Dilation coefficient, d_3	0.0	0.0	0.0	0.0	
Liq_1	1.0	1.0	1.0	1.0	
Liq_2	0.0	0.0	0.0	0.0	
Number of yield surfaces, NYS	20	20	20	20	20
Cohesion, c	0.1 KPa	0.1 KPa	0.1 KPa	0.1 KPa	34.6 KPa

* These are not input parameters for the constitutive model, but rather are parameters computed during model calibration. In particular, the friction angles, shear strengths and shear moduli must be converted from the stress–strain space used in conventional practice to the octahedral stress-strain space used in the constitutive model.

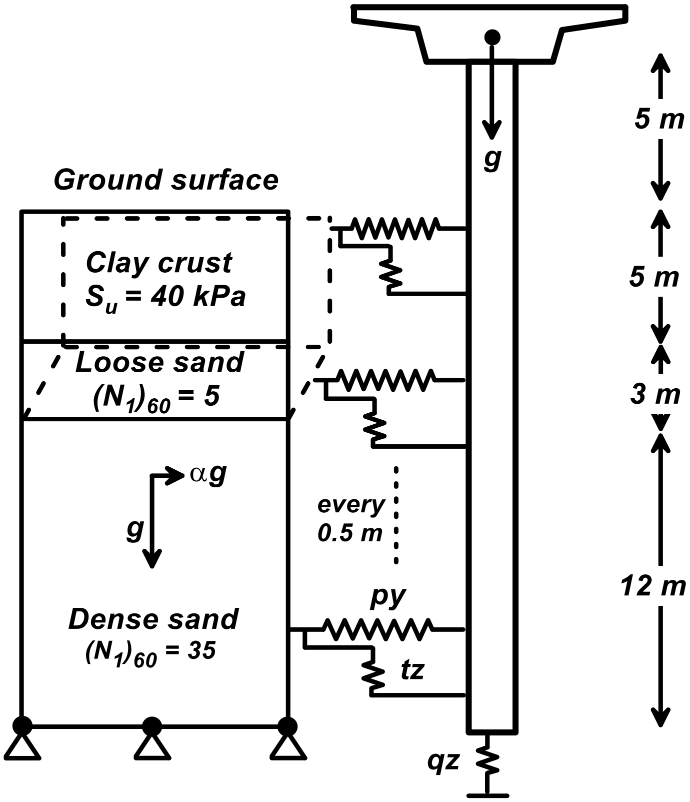

Figure 4-1: Depiction of the FE model

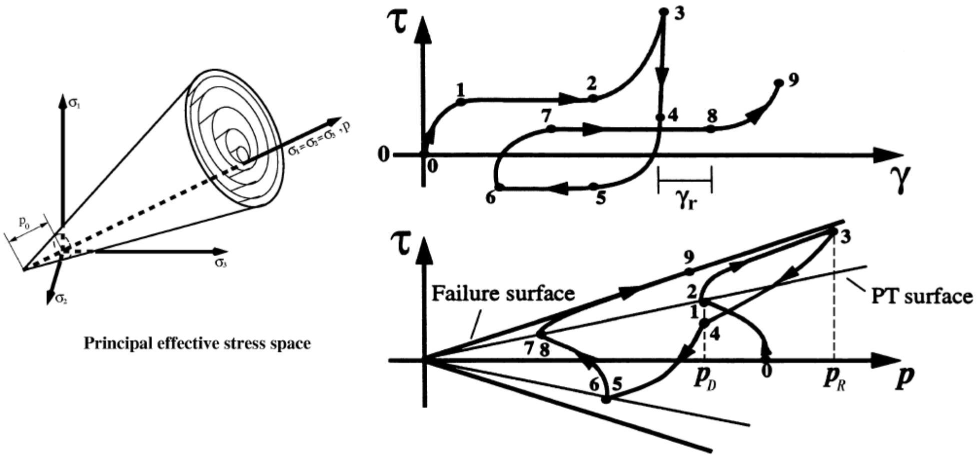

Figure 4-2: Pressure dependent multi yield surface model (Elgamal et al. 2001)

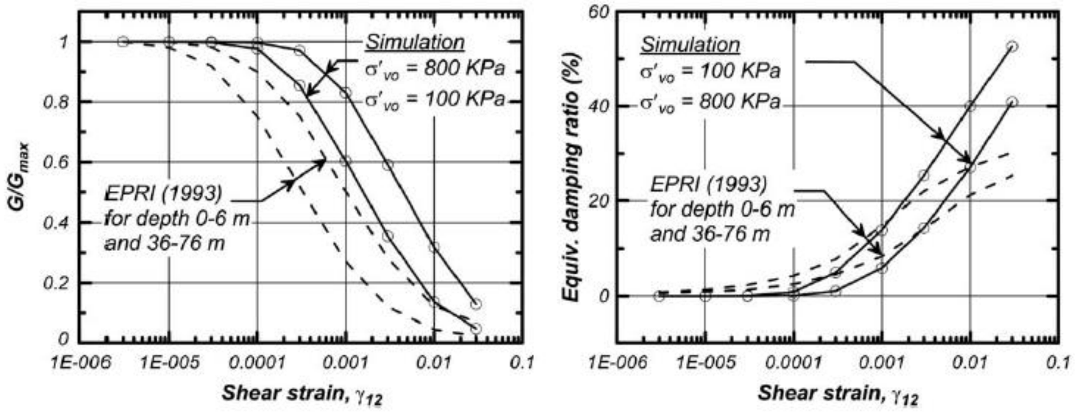

Figure 4-3: G/Gmax and equivalent damping ratios for undrained loading of sand with $(N_{1)60}=5$

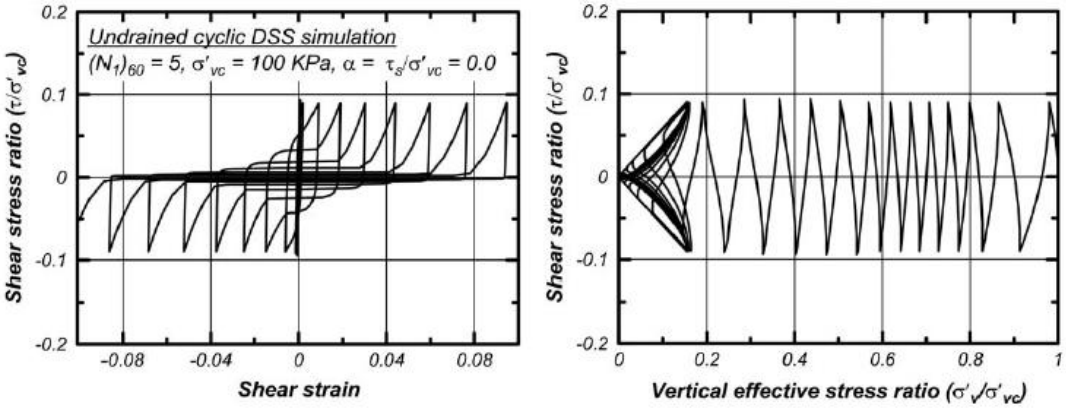

Figure 4-4: Undrained cyclic direct simple shear (DSS) simulation for sand with $(N_{1)60}=5$

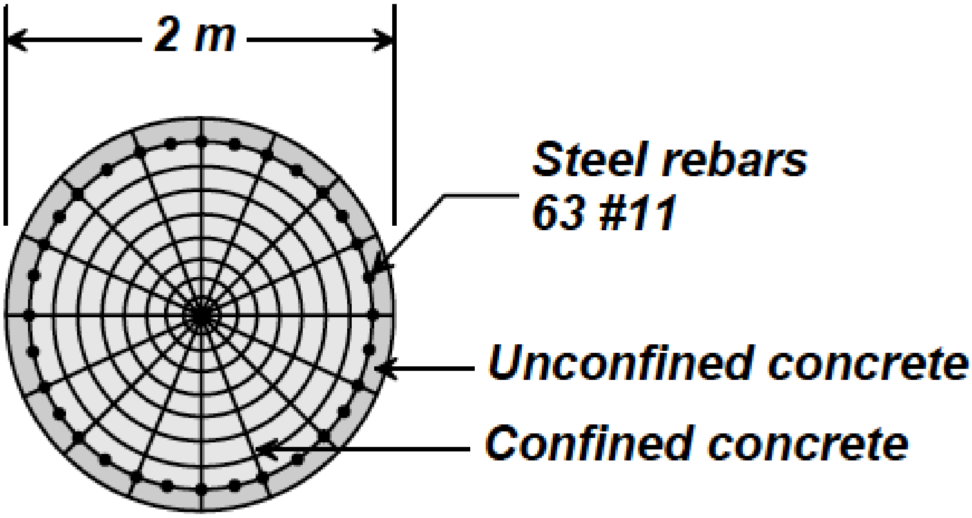

Figure 4-5: Cross section of the fiber section used to model the pile shaft

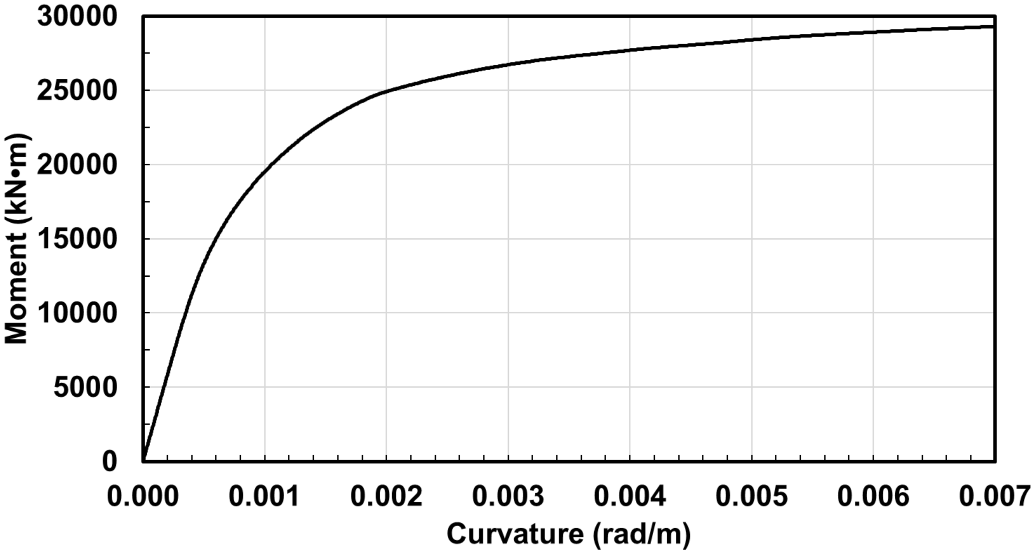

Figure 4-6: Moment-curvature behavior of the pile shaft

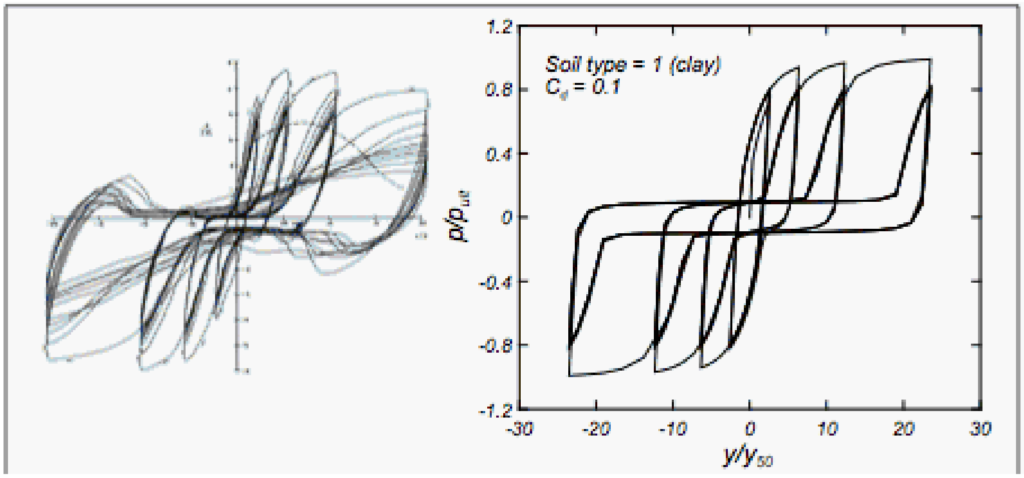

Figure 4-7: Example of PYSimple1 material behavior (OpenSees Wiki 2009)

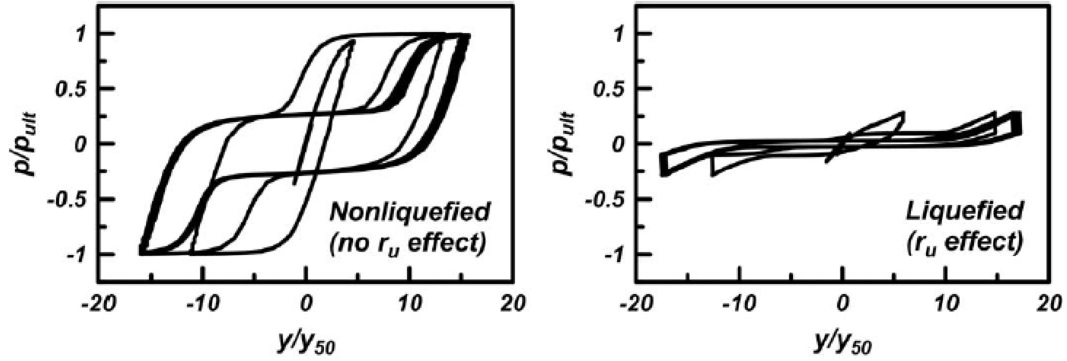

(a)

(b)

Figure 4-8: Example of PyLiq1 and TZLiq1 material behavior during (a) nonliquefied conditions (b) liquefied conditions

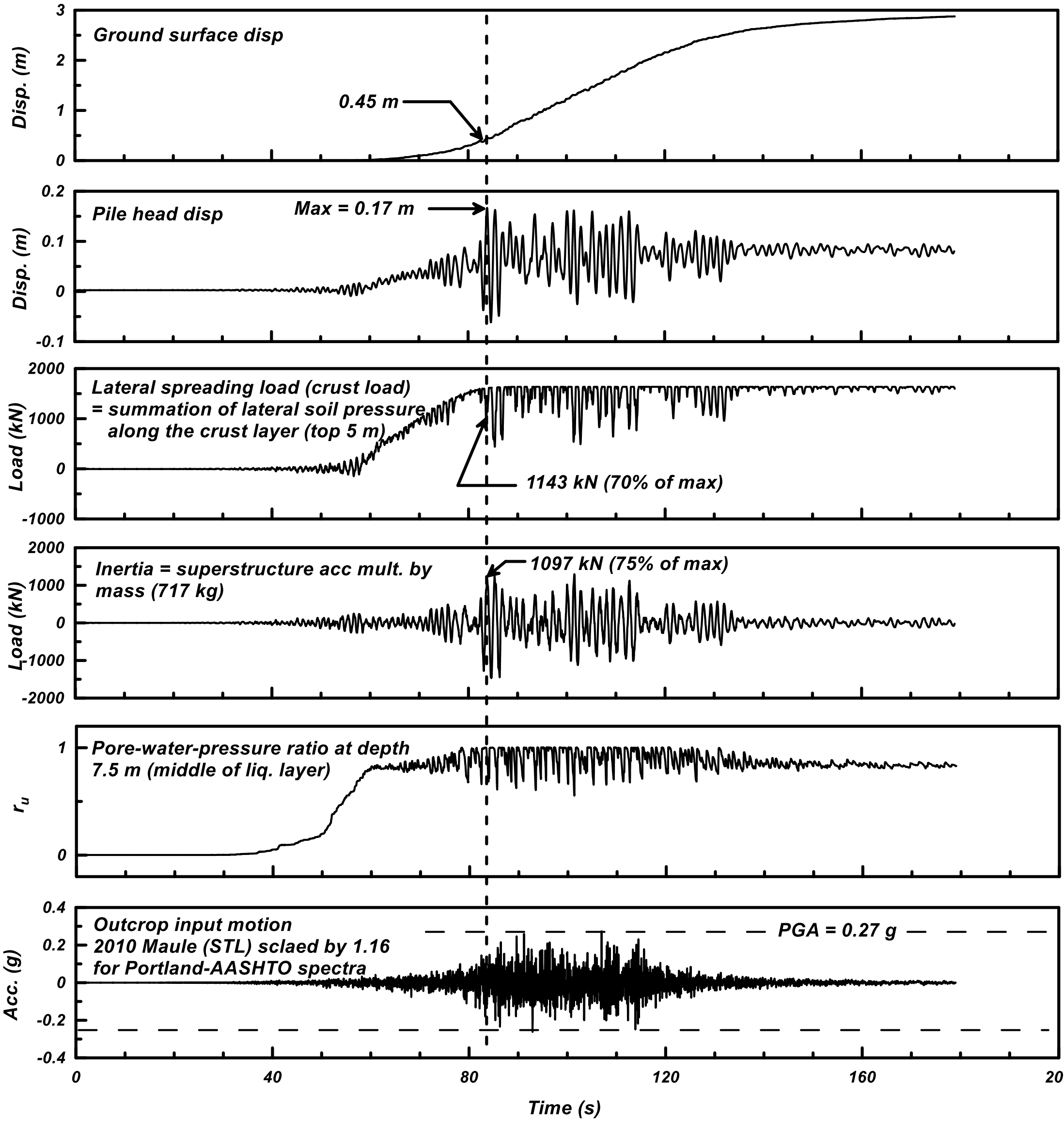

Figure 4-9: Representative nonlinear dynamic analysis (NDA) results for the 2010 Maule EQ (Station STL) scaled by a factor of 1.16 for the AASHTO design spectrum developed for the Portland site

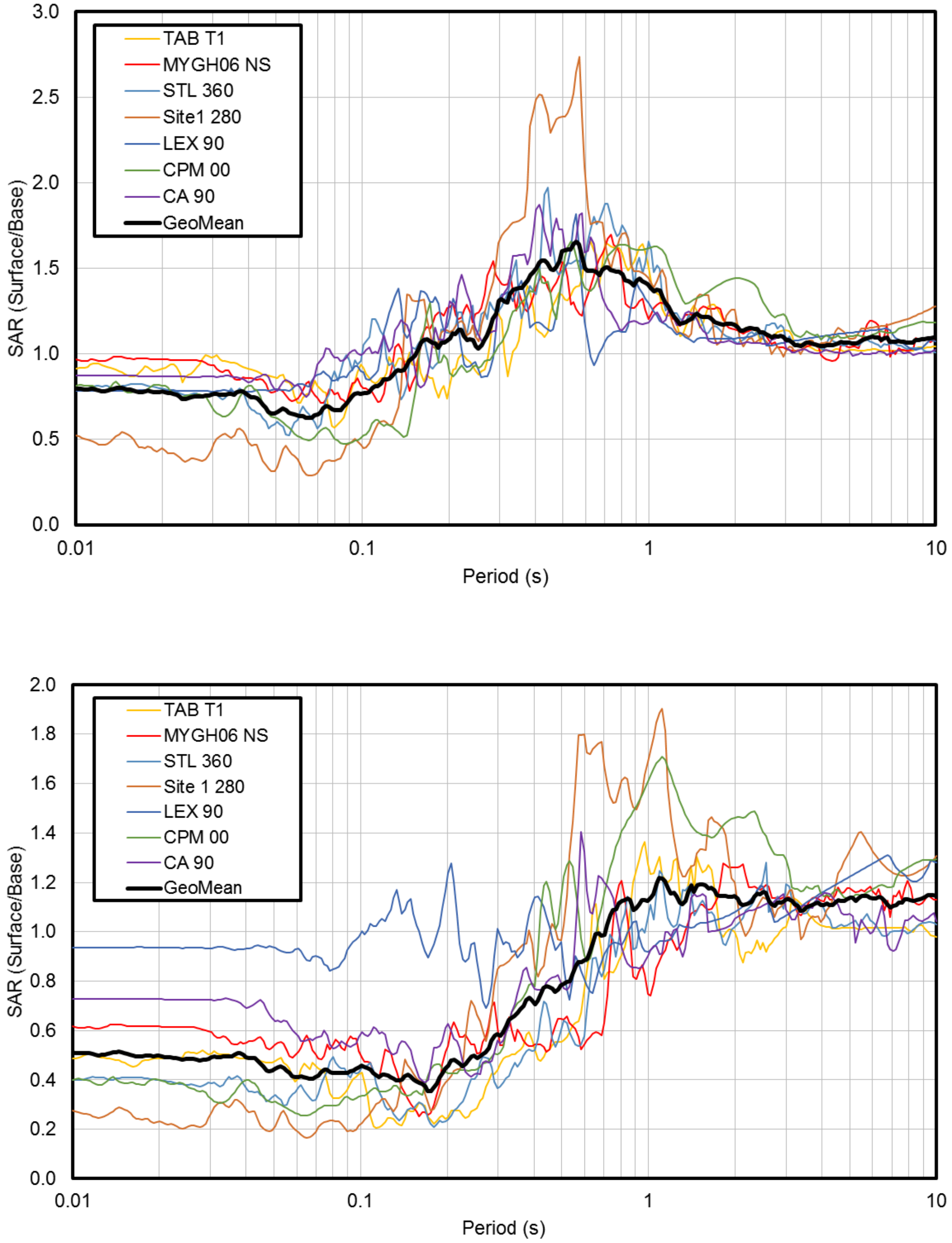

Figure 4-10: Spectral amplification ratios (SAR) for the nonliquefied, level ground case (top) and liquefied case with α=0.1 (bottom) at the Portland site (ground motions scaled to the MCEr target spectrum)

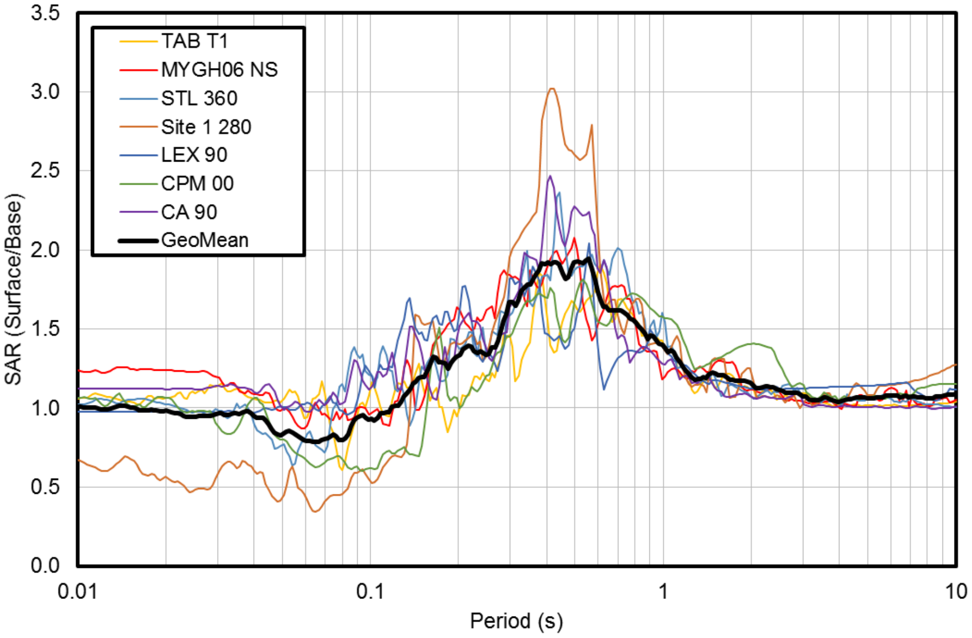

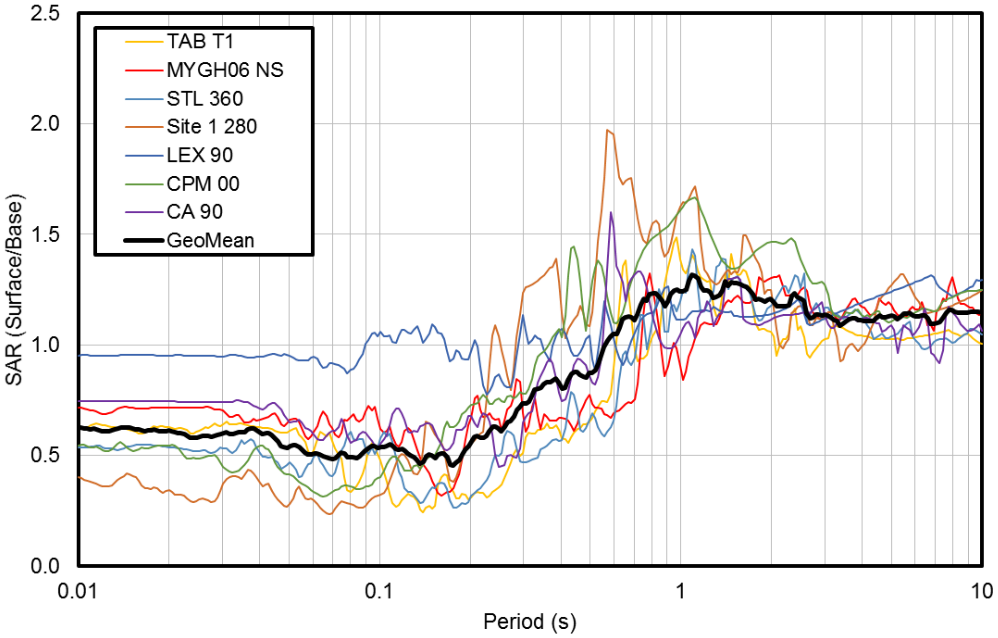

Figure 4-11: Spectral amplification ratios (SAR) for the nonliquefied level ground case (top) and liquefied case with α=0.1 (bottom) at the Portland site (ground motions scaled to the AASHTO target spectrum)

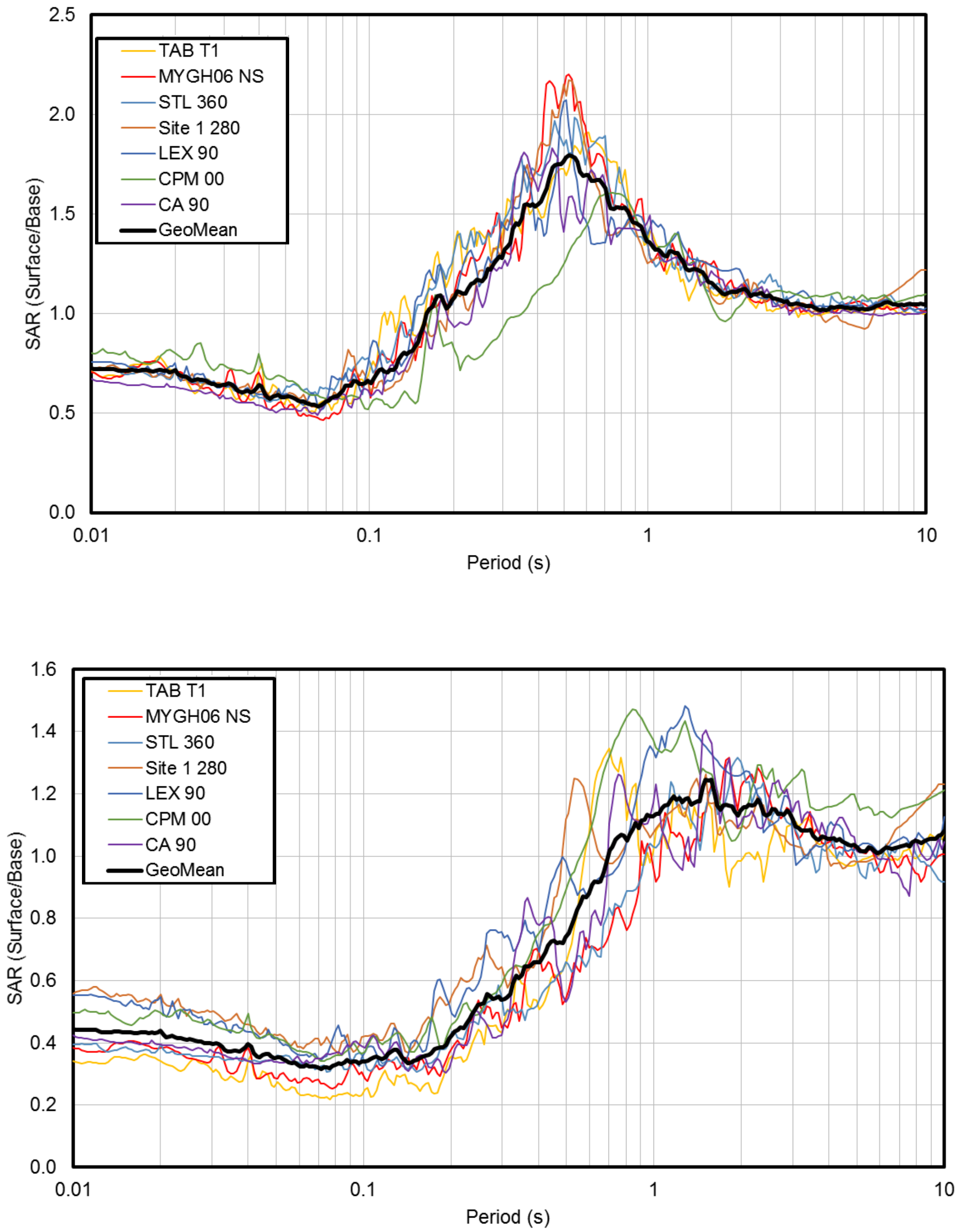

Figure 4-12: Spectral amplification ratios (SAR) for the nonliquefied, level ground case (top) and liquefied case with α=0.1 (bottom) at the Portland site (ground motions matched to the MCEr target spectrum)

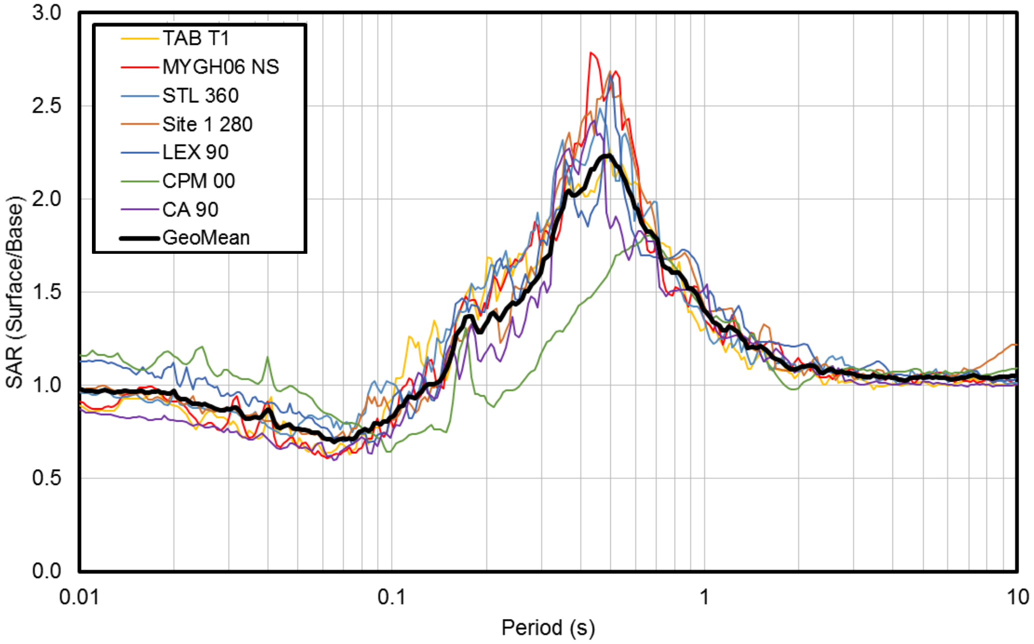

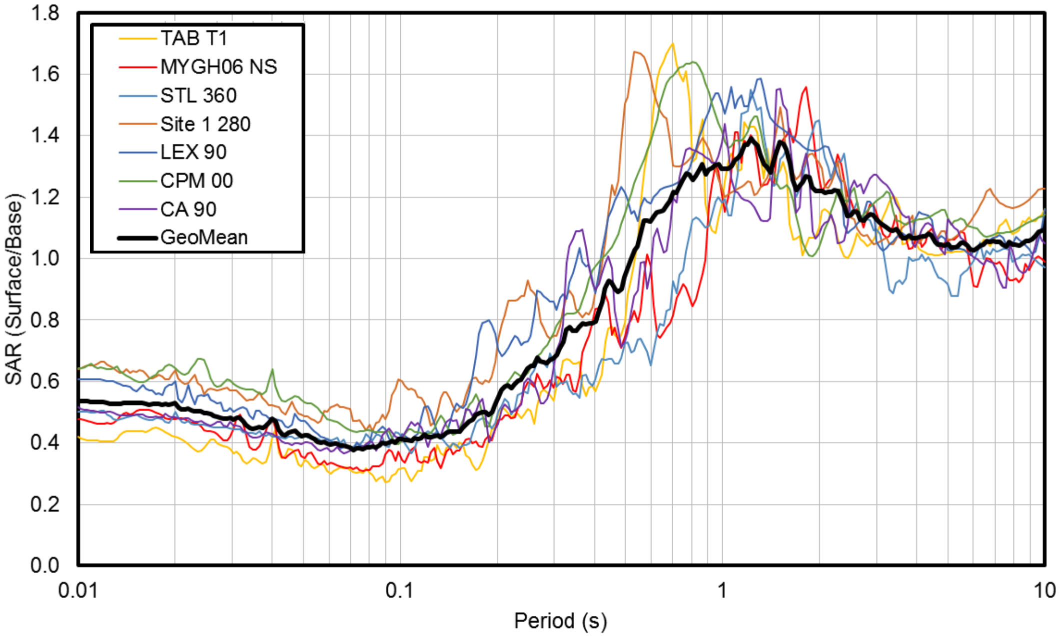

Figure 4-13:Spectral amplification ratios (SAR) for the nonliquefied, level ground case (top) and liquefied case with α=0.1 (bottom) at the Portland site (ground motions matched to the AASHTO target spectrum)

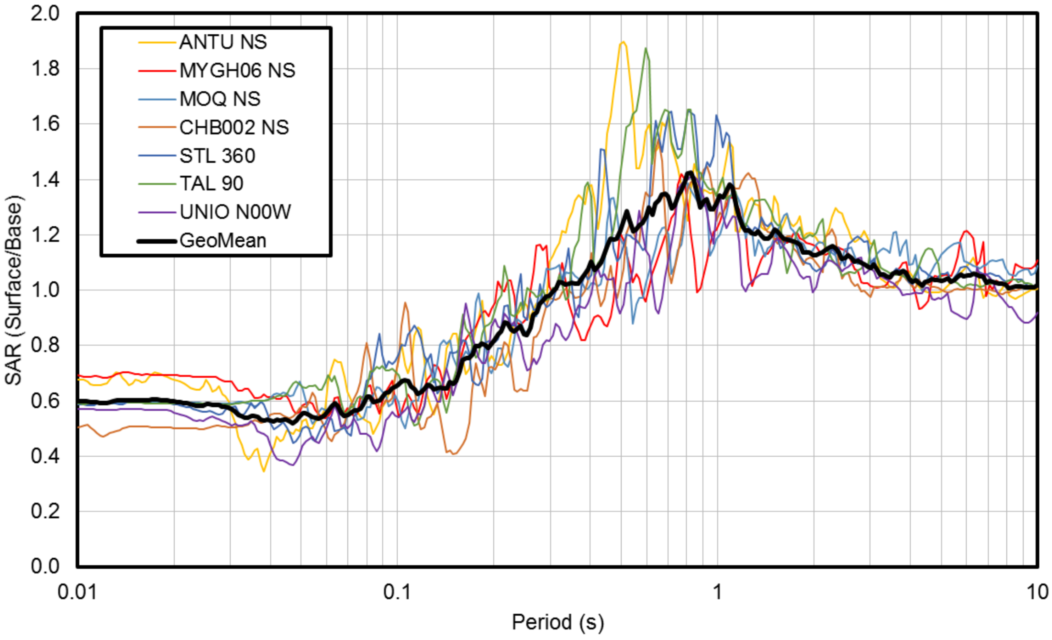

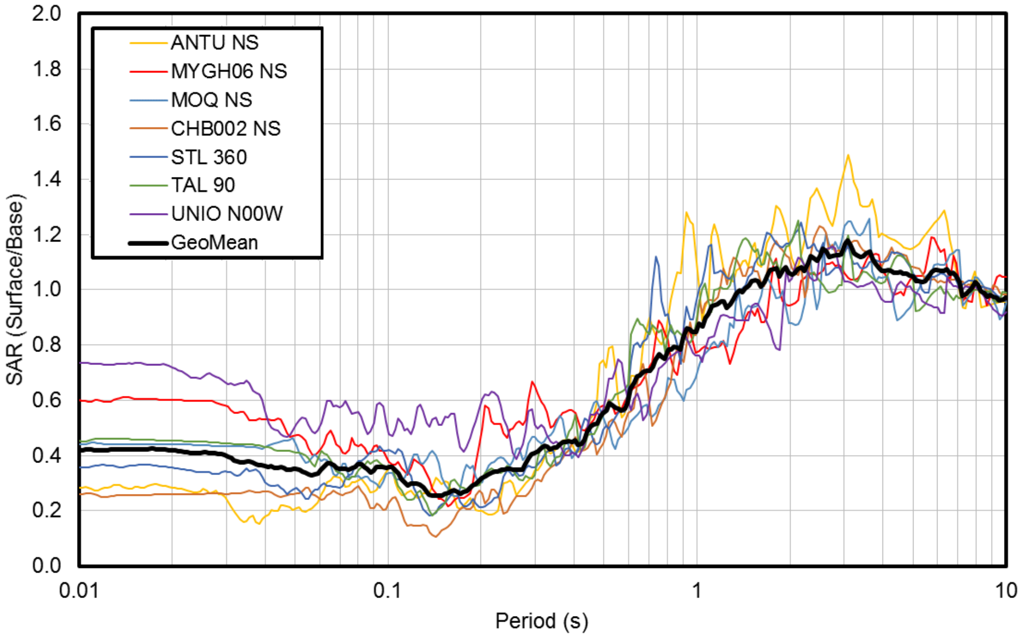

Figure 4-14: Spectral amplification ratios (SAR) for the nonliquefied, level ground case (top) and liquefied case with α=0.1 (bottom) at the Astoria site (ground motions scaled to the MCEr target spectrum)

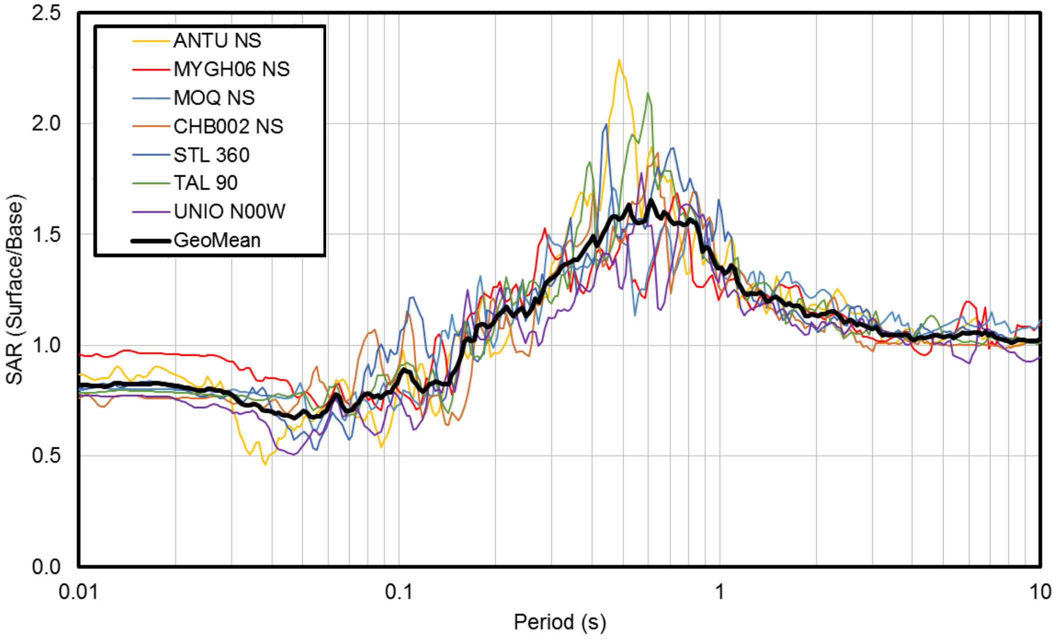

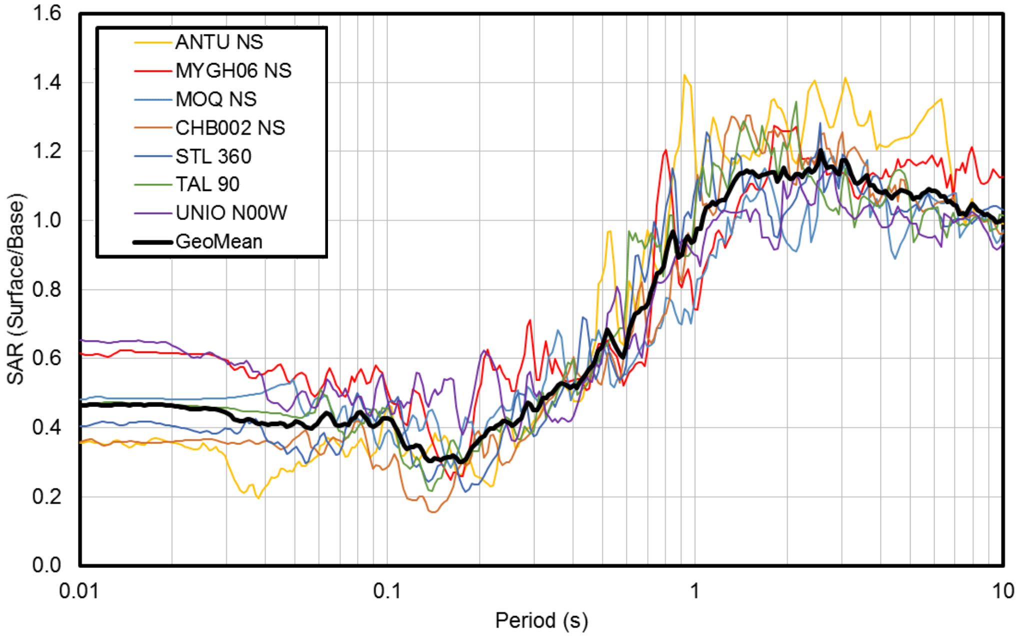

Figure 4-15: Spectral amplification ratios (SAR) for the nonliquefied, level ground case (top) and liquefied case with α=0.1 (bottom) at the Astoria site (ground motions scaled to the AASHTO target spectrum)

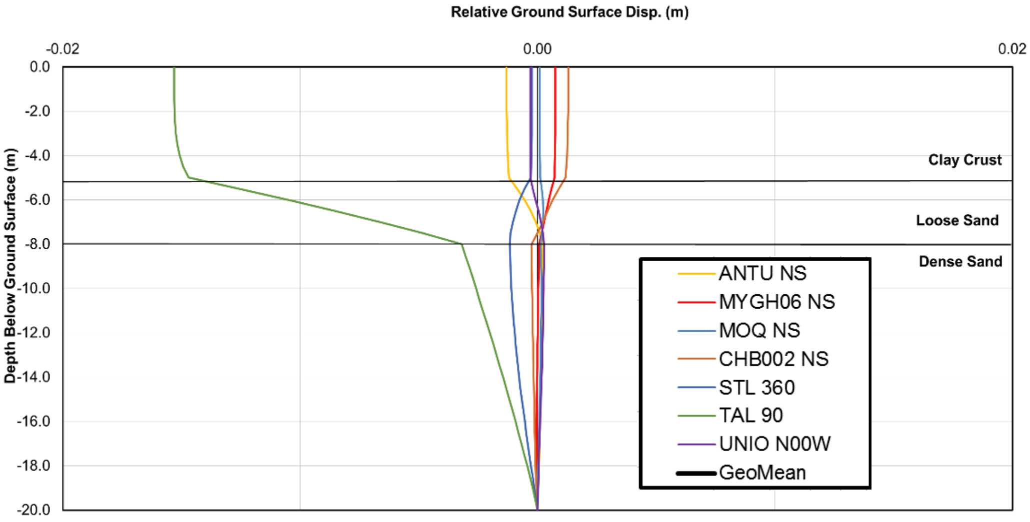

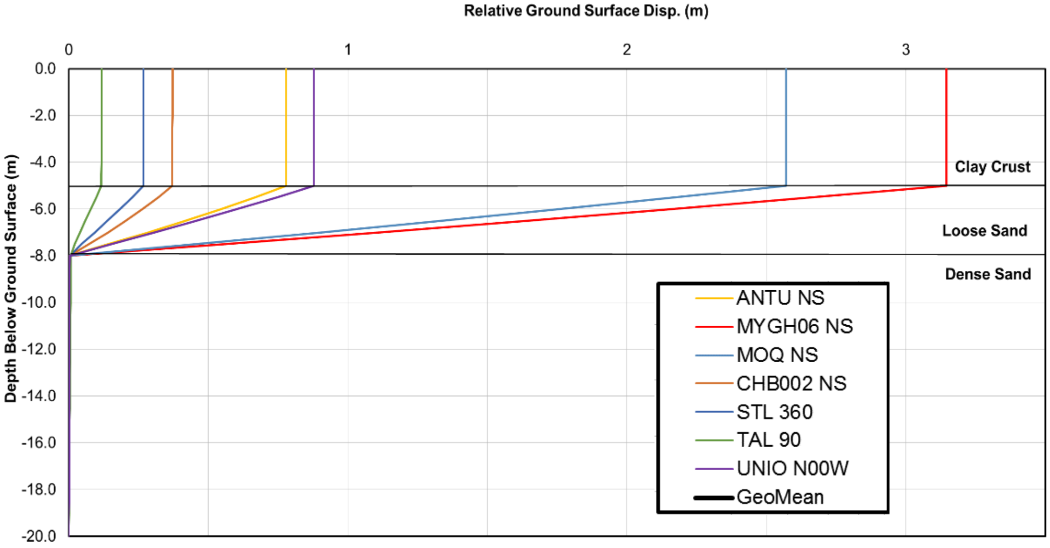

Figure 4-16: Relative soil displacement profiles from NDA for the Portland site with the seven ground motions matched to the AASHTO target spectrum in nonliquefied case on level ground (top) and liquefied case with α=0.1(bottom)

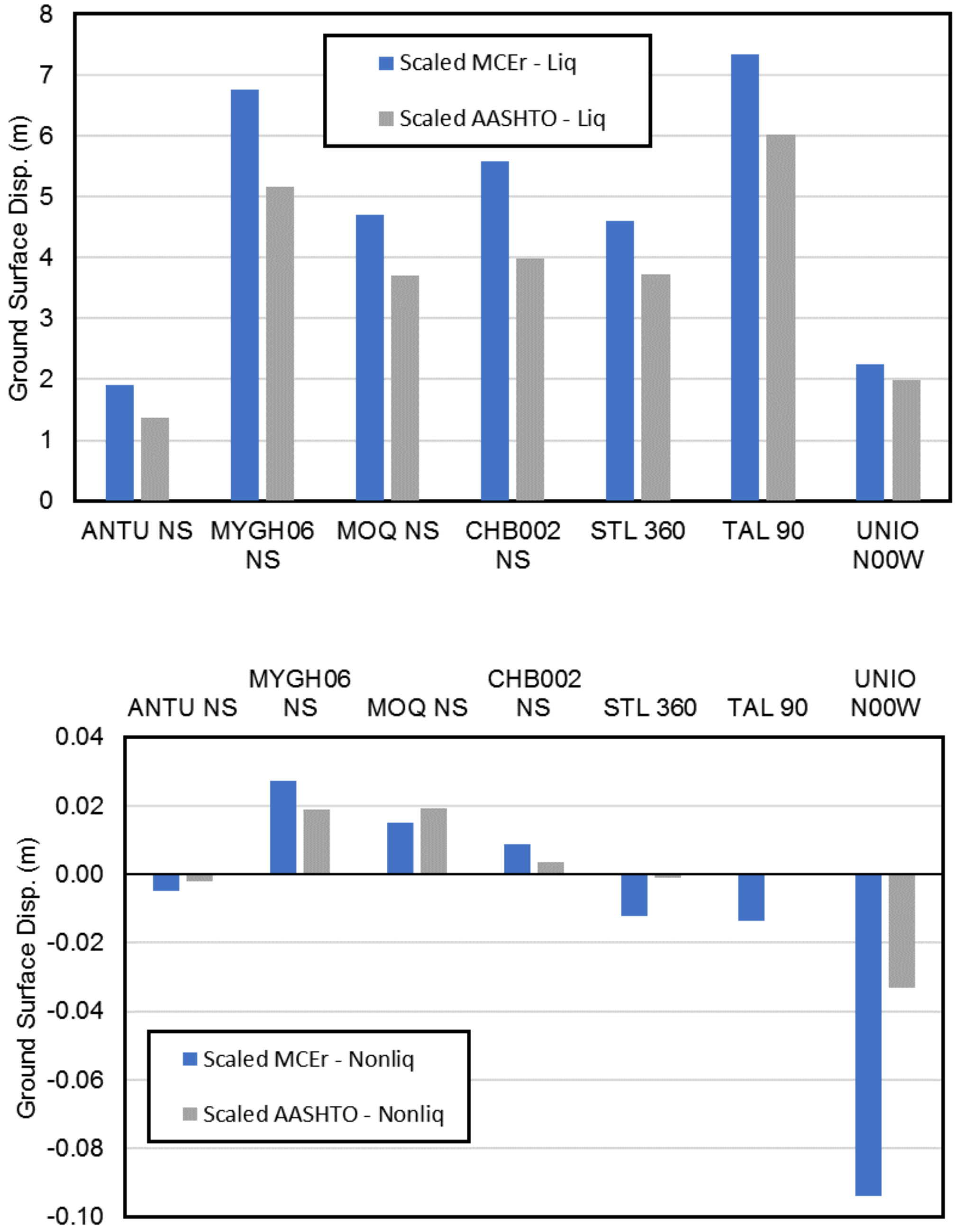

Figure 4-17: Relative ground surface soil displacements at the end of ground motion from NDA for the Astoria site in liquefied case with α=0.1(top) and nonliquefied case on level ground (bottom)

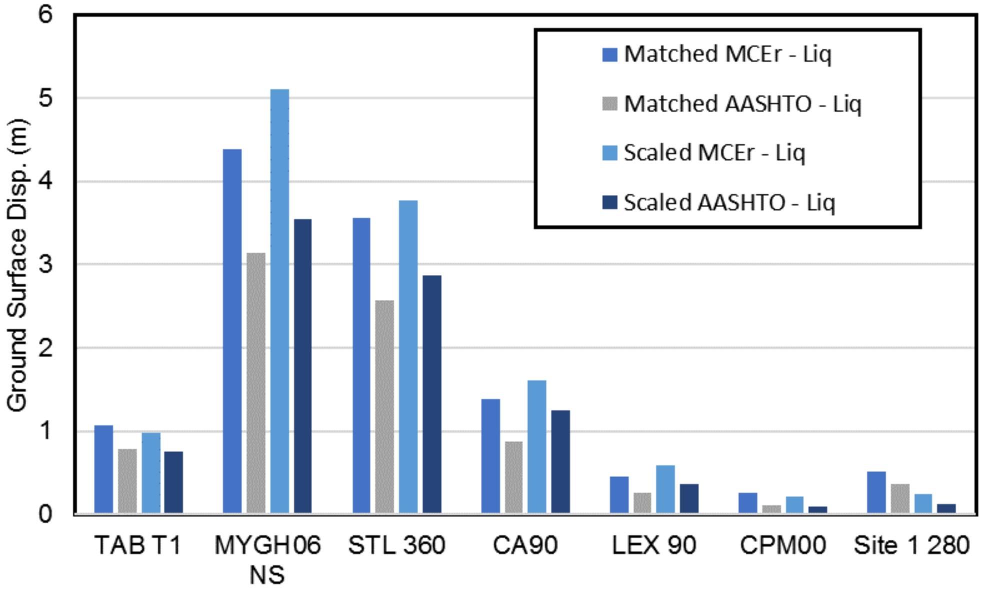

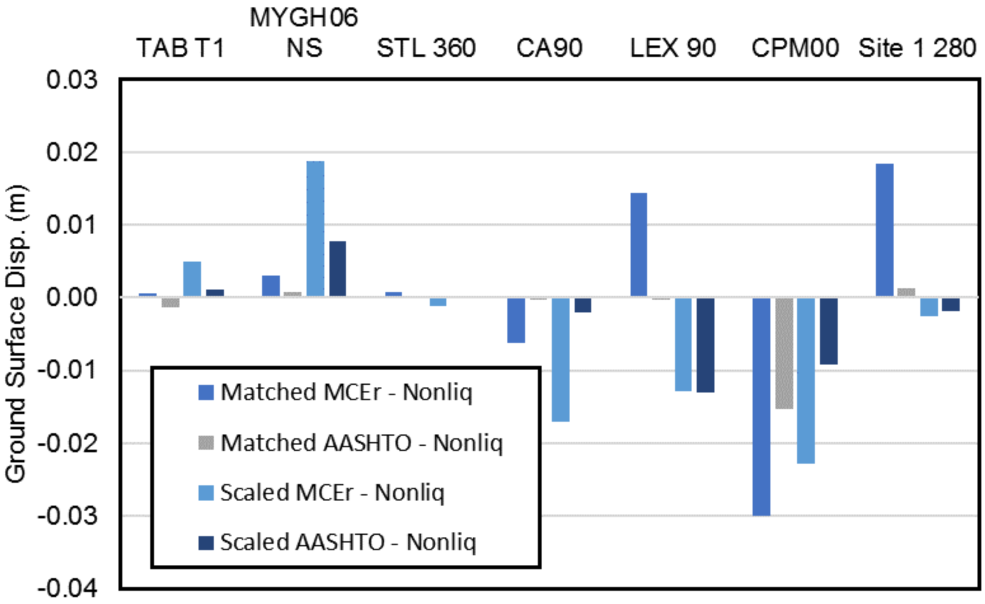

Figure 4-18: Relative ground surface soil displacements at the end of ground motion from NDA for the Portland in liquefied case with α=0.1(top) and nonliquefied case on level ground (bottom)

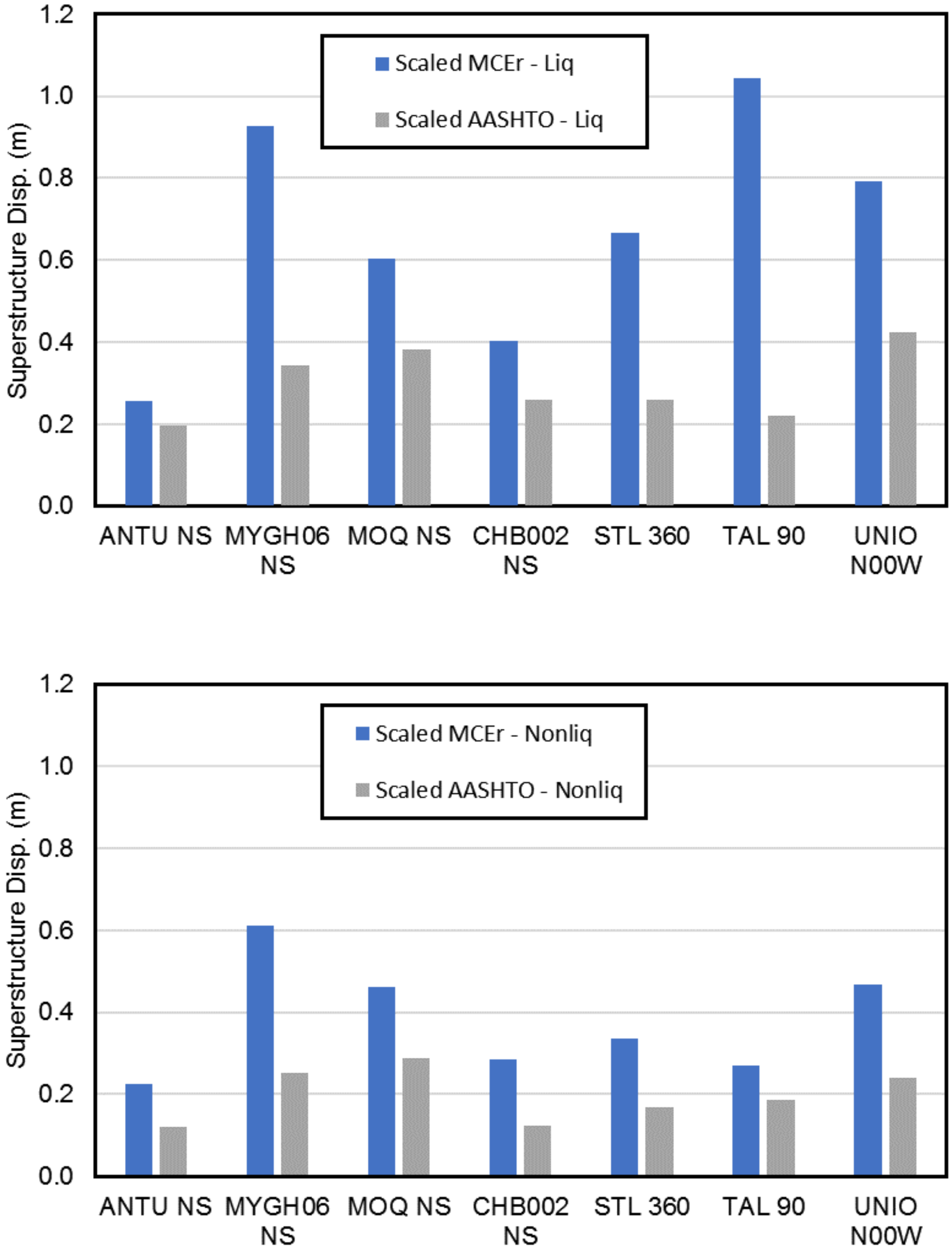

Figure 4-19: Maximum relative superstructure displacement from NDA for the Astoria site in liquefied case with α=0.1(top) and nonliquefied case on level ground (bottom)

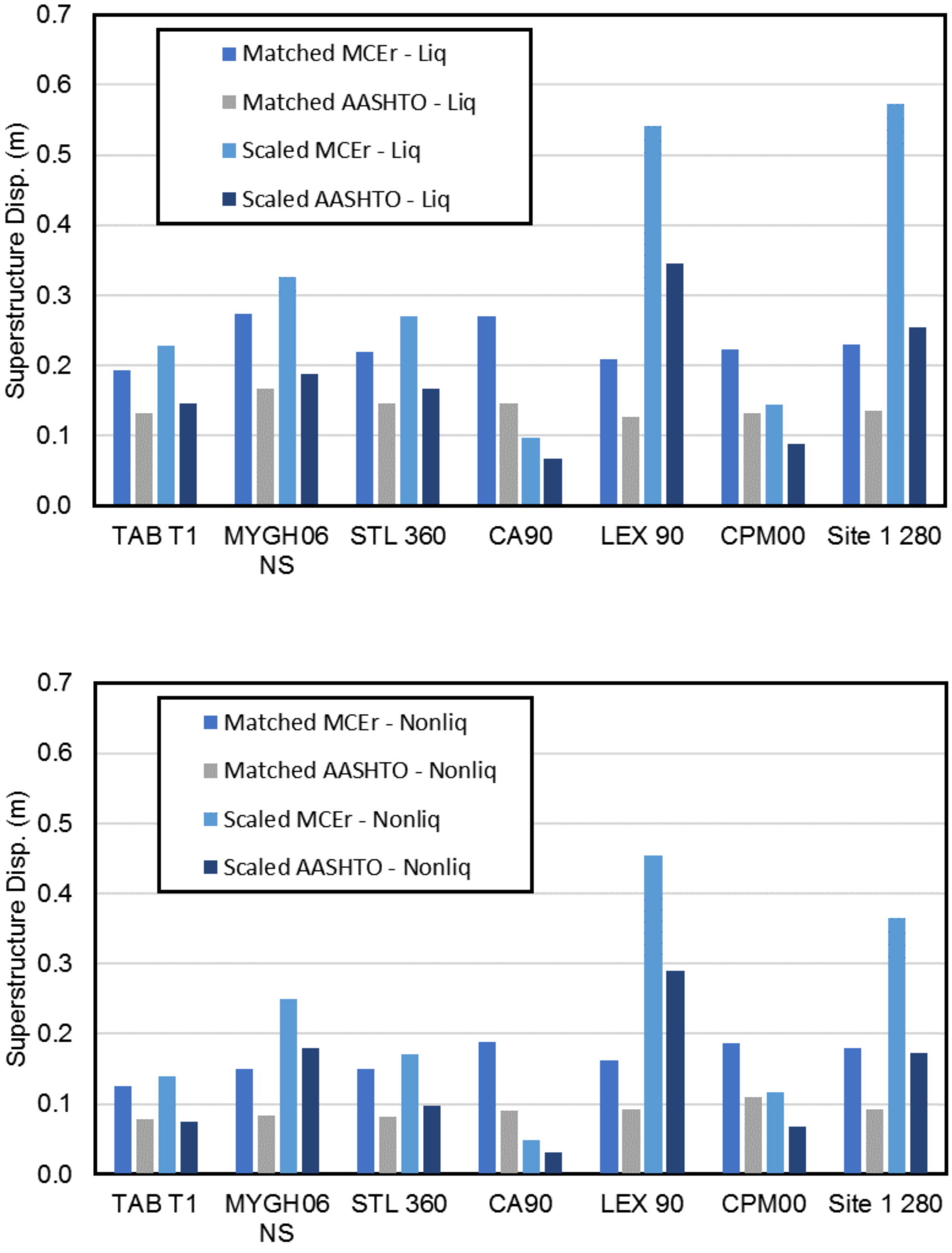

Figure 4-20: Maximum relative superstructure displacement from NDA for the Portland site in liquefied case with α=0.1(top) and nonliquefied case on level ground (bottom)

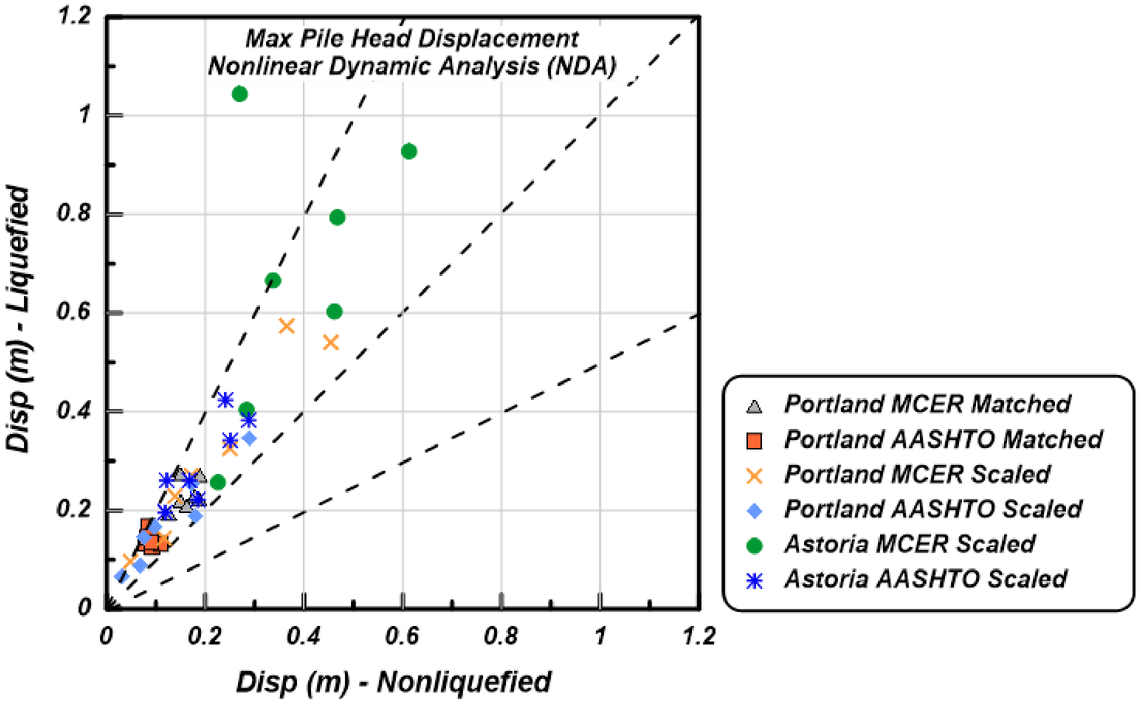

Figure 4-21: Comparison of maximum pile head displacements in liquefied sloped-ground conditions versus nonliquefied level-ground conditions from nonlinear dynamic analyses (NDA)

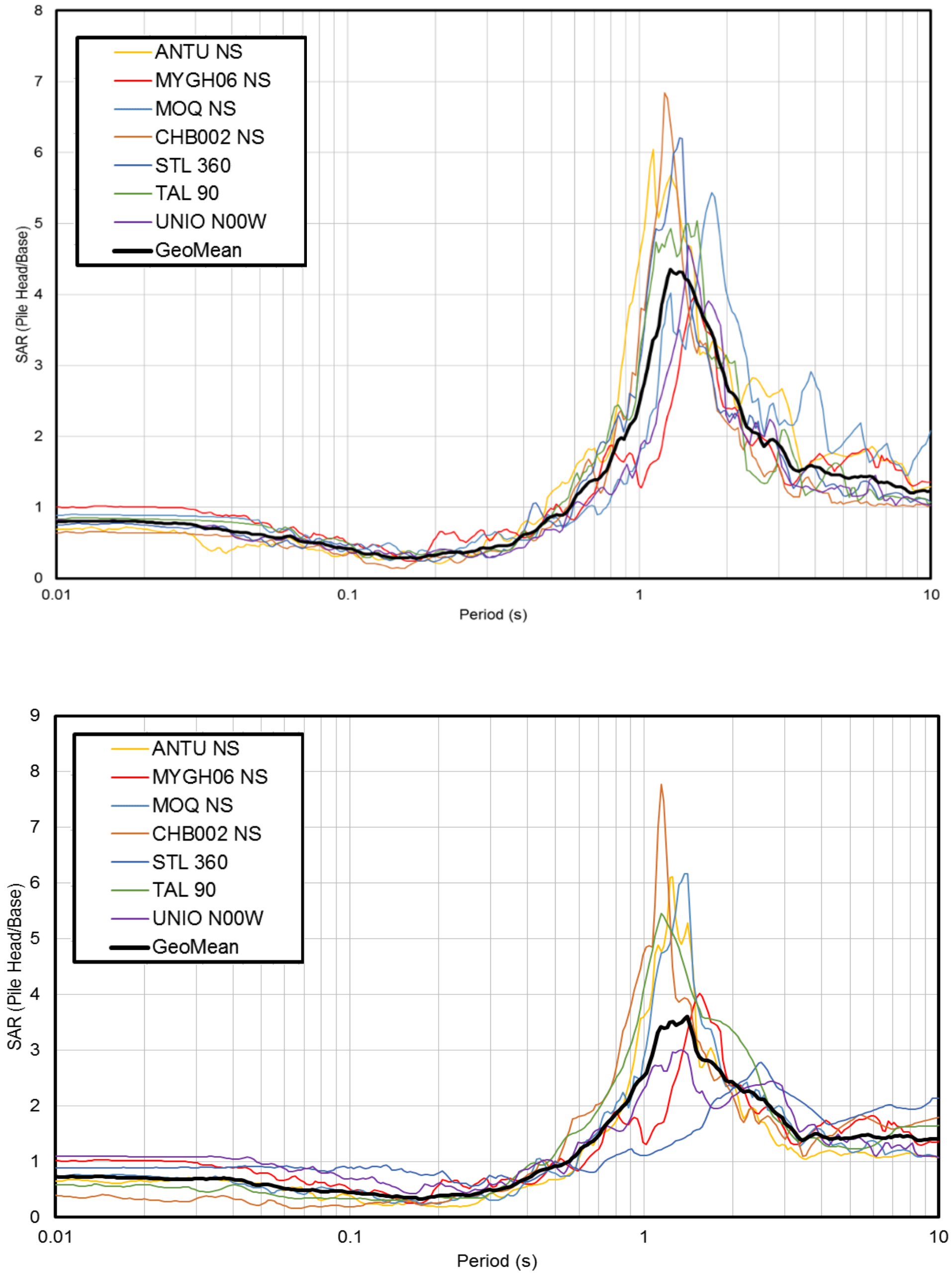

Figure 4-22: Spectral amplification ratios (SAR) for the pile head (i.e. superstructure) in the nonliquefied level-ground case for the Astoria site with the ground motions scaled to the AASHTO target spectrum (top) and for the Astoria site with ground motions scaled to the MCEr target spectrum (bottom)

5 EQUIVALENT STATIC ANALYSIS (ESA)

5.1 Background

The Caltrans/ODOT equivalent static analysis (ESA) method consists of, first, performing a pushover analysis for nonliquefied conditions to get the inertial demands, and then performing pushover analysis for liquefied conditions, combining inertial and kinematic demands. This chapter covers the steps involved in performing the Caltrans/ODOT ESA and discusses the accuracy of the method. Once the relative accuracy of the Caltrans/ODOT ESA method was evaluated, the NDA results were used to propose an improved ESA method.

5.2 ESA model

The ESA was conducted using the program LPILE (2016). LPILE allows for the analysis of laterally loaded piles by using p-y curves to account for nonlinear load transfer between the pile and soil. It is expected that the recommendations contained herein would be equally applicable to other programs that utilize the p-y method of laterally-loaded pile analysis. It should be noted, though, that a few features of LPILE proved to be especially useful for this analysis, namely the ability to impose soil displacements on the end-nodes of the p-y springs and to define the moment-curvature response of the pile under consideration.

5.2.1 Input Parameters

Figure 5-1 shows the soil profile used in the ESA. It consisted of the same strata that were present in the NDA: a 5-meter thick clay crust, overlying a 3-meter thick loose sand, overlying a 12-meter thick dense sand layer. The pile head extended 5-meters above the ground surface, just as it did in the FE model. The soft clay p-y curves were used for the clay layer, while the API p-y curves were used for the loose and dense sand layers (LPILE 2016). The various soil and p-y curve parameters are shown in Figure 5-1.

The 2-meter diameter RC pile was modelled in LPILE by defining its moment-curvature behavior. The behavior was computed from a section analysis of the RC pile used in the FE model and is shown in Figure 4-6.

5.2.2 Pushover comparison

Since the NDA results serve as a point of comparison for the ESA results, the pushover response of the system should exhibit similitude regardless of the analysis method. Using the previously discussed p-y curves and soil parameters, along with the user defined moment-curvature behavior, a pushover curve for the RC pile was developed in LPILE. This curve was compared against the pushover curve of the same RC pile used in the OpenSees FE model. A comparison of the two pushover curves for the nonliquefied condition is shown in Figure 5-2; the two curves showed good agreement.

5.3 ESA Procedure

5.3.1 Nonliquefied conditions

Performing the ESA for nonliquefied condition consists of the following steps: (1) Perform pushover analysis with nonliquefied (regular) p-y springs. (2) Estimate the equivalent lateral stiffness and the natural period of the soil-pile system. Caltrans recommends using the first-rebar-yield point to calculate the equivalent stiffness. However, Khosravifar and Boulanger (2012) found that 75% of the ultimate pushover force ($F_{ult)}$ better represents the equivalent stiffness; therefore, this method was used in this study. (3) Find the elastic inertia using the elastic design spectrum (5% damping) developed for the ground-surface in the nonliquefied condition. (4) Use the R-μ-T relationships to convert elastic inertial demands to inelastic demands. Equal-displacement assumption can be applied for long-period structure (ATC-32 1996). Figure 5-3 shows the comparison of the maximum pile head displacements obtained from NDA and those estimated from ESA, both in the nonliquefied condition. This figure shows that the ESA adequately estimates the pile demands in nonliquefied conditions. The residuals between the ESA and NDA results have a standard deviation of 0.15, assuming a log-normal distribution.

5.3.2 Liquefied conditions

The Caltrans/ODOT method (Caltrans 2012 and Ashford et al. 2012) outlines ESA procedures to estimate pile demands due to liquefaction-induced lateral spreading. The method consists of three primary steps: (1) Estimate kinematic demands by calculating liquefaction-induced lateral spreading displacements. (2) Estimate the inertial load in liquefied conditions that coincides with the kinematic demands by taking 50% of the maximum inertial load in nonliquefied conditions. (3) Combine 100% of kinematic demands and 50% of inertia in ESA.

5.3.2.1 Estimate Liquefaction Induced Lateral Spreading

The soil displacements were estimated using the simplified procedures by Idriss and Boulanger (2008). The factor of safety (FOS) against liquefaction in the loose sand layer was found to be 0.1 and 0.15 for the AASHTO and MCER seismic demands at both sites, respectively, indicating that liquefaction will trigger under design level shaking. The free-field lateral spreading displacements were estimated as 1.5 meters for both levels of seismic demands using the simplified LDI method. While the Caltrans/ODOT method allows designers to take advantage of pile-pinning effects to reduce the soil displacements within embankments, the slope in this study was assumed to be infinite and pile-pinning effects were not considered. The soil displacement profile was assumed constant through the clay crust and linearly reduced to zero through the liquefied layer. The calculated pile head displacement due to the lateral spreading only (i.e. kinematic demand) was 0.04 meters. The ratio of the lateral spreading induced bending moment to the plastic moment of the RC section was MLS/Mp = 30% (Mp = 30 MN.m).

5.3.2.2 Estimate Inertial Load in Liquefied Conditions

The elastic inertial loads in nonliquefied conditions were multiplied by 50% per the Caltrans/ODOT guideline to account for two main effects: 1) the change in site response due to liquefaction, and 2) the portion of inertia that is likely to coincide with the kinematic loads during the critical cycle. The critical cycle is defined here as the loading cycle during which the pile head displacement is maximum.

5.3.2.3 Combine Kinematic and Inertial Demands in a Pushover Analysis for Liquefied Conditions

The pushover analysis was performed by, first, modifying the p-y curves in the liquefied layer. The p-multiplier in the loose liquefiable layer in this study was calculated as 0.05 per Caltrans (2012). The p-multipliers were linearly increased to 1.0 at a distance equal to one pile diameter (2 m) above and below the liquefying layer to account for the weakening effects of the liquefying layer on the overlying and underlying nonliquefied layers (McGann et al. 2011). Second, the lateral spreading displacements were applied to the end-nodes of p-y springs (kinematic demand). Finally, 50% of the inertial load was applied at pile head. The pushover curve in the liquefied conditions is shown on Figure 5-4. The pushover curve in the nonliquefied condition is shown for comparison.

5.4 Comparison of ESA and NDA results

Figure 5-5 shows the accuracy of the Caltrans/ODOT method in estimating pile demands by comparing pile head displacements estimated from ESA with those computed from NDA. For cases where the inertial load in liquefied conditions (50% of inertia in nonliquefied conditions) was smaller than the ultimate pushover load (i.e. 1290 kN), the Caltrans/ODOT method slightly underestimated pile demands. This is evident from the data points plotted below the 1:1 line on Figure 5-5. However, those cases where the inertial load exceeded the ultimate pushover load (inelastic piles) could not be analysed. This is because the application of inertia in the Caltrans/ODOT method is load-based. These cases are all plotted at 1 meter on Figure 5-5 for plotting purposes. While most design codes prohibit inelastic deformations in piles under the ground (e.g. ODOT GDM 2014), this performance criterion is costly and sometimes impossible to achieve. This is especially true in cases where a thick non-liquefiable crust overlies a liquefiable layer. In the next section, a new ESA method is proposed to estimate inelastic demands in piles, specifically for long-duration earthquakes.

5.4.1 Proposed ESA method

5.4.1.1 Extension of the ESA to Inelastic Demands

As described in the previous section, the application of the Caltrans/ODOT method is limited to elastic piles, i.e. cases where 50% of inertia is smaller than the ultimate pushover force in liquefied conditions. To extend the ESA to inelastic piles, a similar approach to the one used in the nonliquefied conditions was adopted in this study and its effectiveness was evaluated against NDA results. The initial stiffness of the liquefied pushover curve was linearized using the point corresponding to 75% of the ultimate pushover force, from which an elastic displacement demands are calculated. The elastic displacement demands were then converted to inelastic displacement demands following the equal-displacement assumption for long-period structures (ATC-32 1996). This process is shown in Figure 5-6 and formulated in Equation 1:

$$\Delta_{liq} = \Delta_{LS} + \frac{(\text{multiplier}) \times (\text{elastic inertia in nonliq. case})}{(\text{initial linear stiffness of pushover curve})} \qquad (1)$$

where ΔLiq is the pile head displacement in the liquefied condition due to the combination of lateral spreading and inertial demands, and ΔLS is the pile head displacement due to kinematic demands only. The multiplier in the equation above denotes the fraction of inertia that should be combined with kinematic demands. This multiplier is equal to 50% in the Caltrans/ODOT method and 60%/75% in the proposed ESA method as described in the next section.

5.4.1.2 The Choice of Inertia Multiplier

As described earlier, the Caltrans/ODOT method combines 100% of kinematics with 50% of inertia. The inertia multipliers were back-calculated from the NDA results using Equation 1 and are plotted on Figure 5-7. The figure shows the dependence of inertia multiplier to the ground motion duration ($D_{5\text{-}95}$). The geometric mean of the back-calculated multipliers was approximately 60% for the crustal motions (with $D_{5\text{-}95} < 20$ sec) and 75% for the subduction motions (with $D_{5\text{-}95} > 20$ sec).

5.4.1.3 Proposed ESA

The proposed ESA method consists of the following steps: (1) Apply kinematic demands by imposing soil displacements to the end-nodes of p-y springs to get

ΔLS. Soil displacements can be estimated from simplified procedures, e.g. Idriss and Boulanger (2008). Modify the p-y springs in the liquefied layer, and adjacent layers, using p-multipliers obtained from Caltrans (2012). (2) Estimate the target displacement in the liquefied condition (ΔLiq) from Equation 1. (3) Perform ESA by combining inertia and kinematics as following:

- •100% Kinematic + 60% Inertial (for crustal earthquakes with short duration)
- •100% Kinematic + 75% Inertial (for subduction earthquakes with medium to long duration)

5.4.1.4 Comparison of Pile Demands Estimated using the Proposed ESA Method and the NDA Results

Figure 5-8 shows the comparison of estimated pile demands using the proposed ESA approach with those computed from the dynamic analyses (NDA). This comparison provides a measure of accuracy for the proposed ESA method. The primary improvement of the proposed ESA method over the Caltrans/ODOT method is the adoption of the equal-displacement approach to convert elastic demands to inelastic demands. While the ESA results compare reasonably well with the NDA results for displacements smaller than 0.4 meter, the ESA estimates are unconservative for displacements larger than 0.4 meter. The threshold of 0.4-meters corresponds to the ultimate pushover force in the liquefied condition, beyond which the pile behavior is inelastic (Figure 5-6). When the displacements are pushed beyond the peak (yield) point on the pushover curve, the pile response becomes very unstable. It is believed that the monotonic nature of the lateral spreading force (crust load) combined with large cyclic inertial loads could excessively, and irrecoverably, deform the pile beyond the yield displacement. Therefore, it is recommended to use the proposed ESA method only for cases where the estimated pile head displacement is smaller than the displacement corresponding to the ultimate pushover force in liquefied conditions (e.g. 0.4-meter in this study).

While the proposed ESA method becomes unconservative for displacements beyond the yield point, the method estimates pile demands reasonably well for elastic piles, including a number of cases that performed well in the NDA but could not be analyzed using the Caltrans/ODOT method (i.e. data points on Figure 5-5 plotted between 0.2 to 0.4 meter on the horizontal axis and at 1 meter on the vertical axis). Additionally, the proposed ESA method provides a means to identify deformations beyond which the pile response becomes unstable and potentially unconservative. For these cases, an equivalent static analysis (ESA) does not accurately predict the pile demands and nonlinear dynamic analysis (NDA) is required.

5.5 Tables and Figures

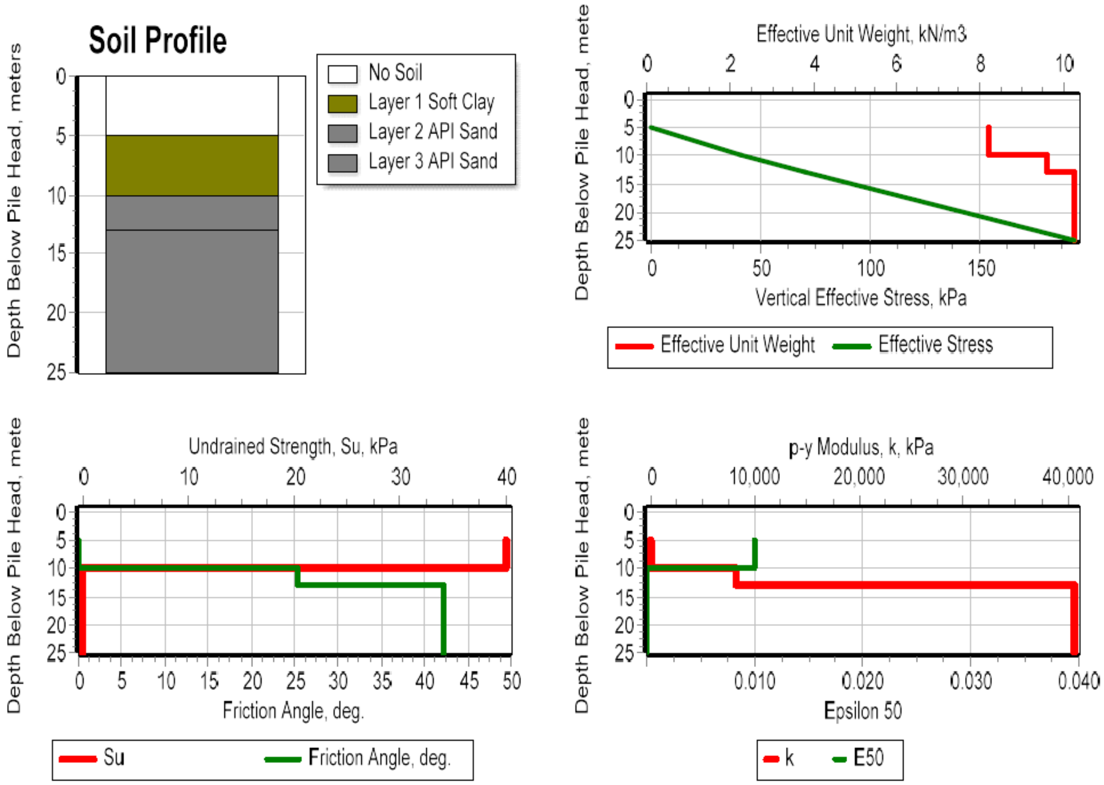

Figure 5-1: Soil profile and parameters used for the LPILE analysis

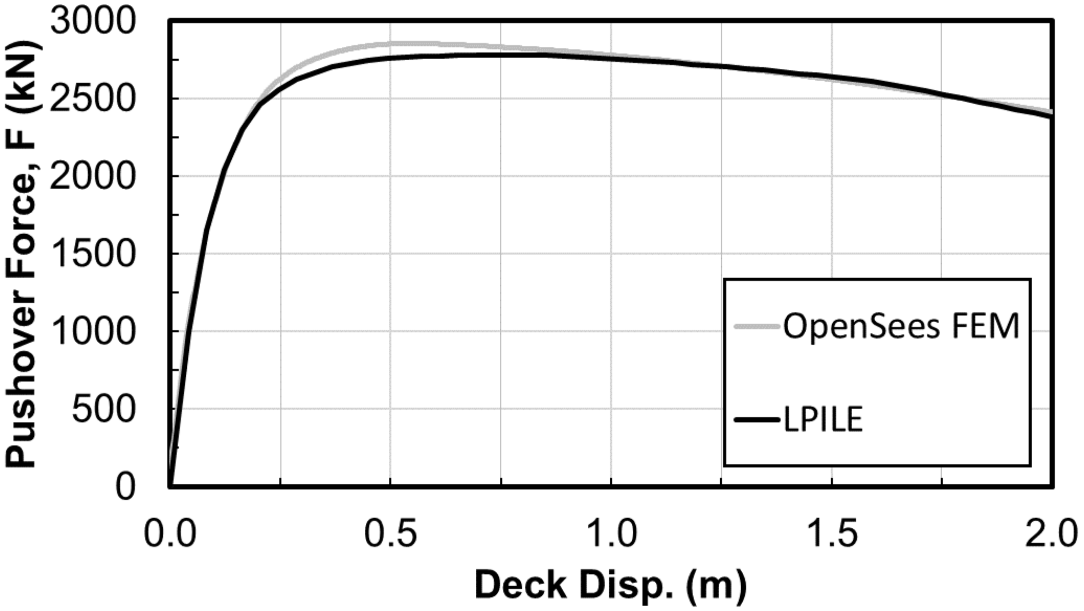

Figure 5-2: Comparison of pushover curves obtained from the LPILE analysis and the OpenSees FE model

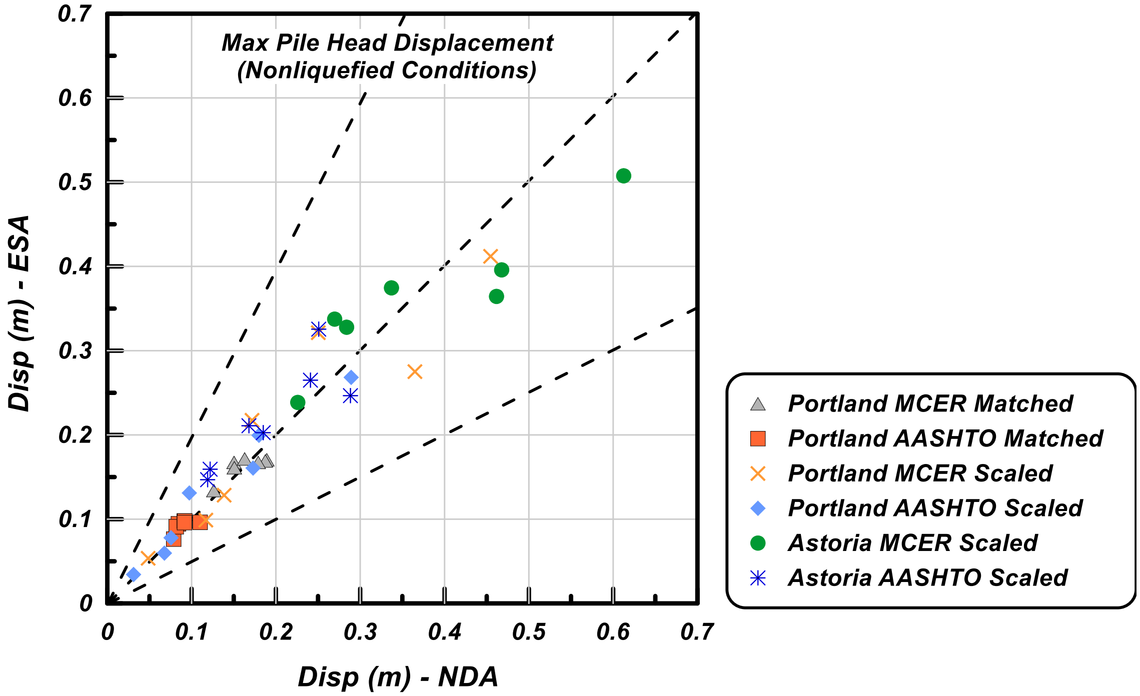

Figure 5-3: Comparison of maximum pile head displacements in nonliquefied conditions estimated from equivalent static analysis (ESA) and those computed from nonlinear dynamic analysis (NDA)

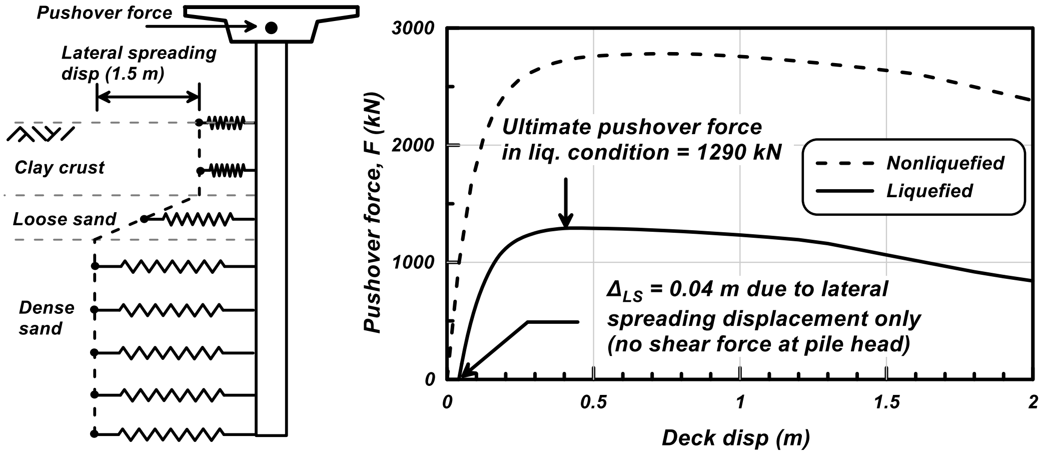

Figure 5-4: Pushover curve in liquefied and nonliquefied conditions

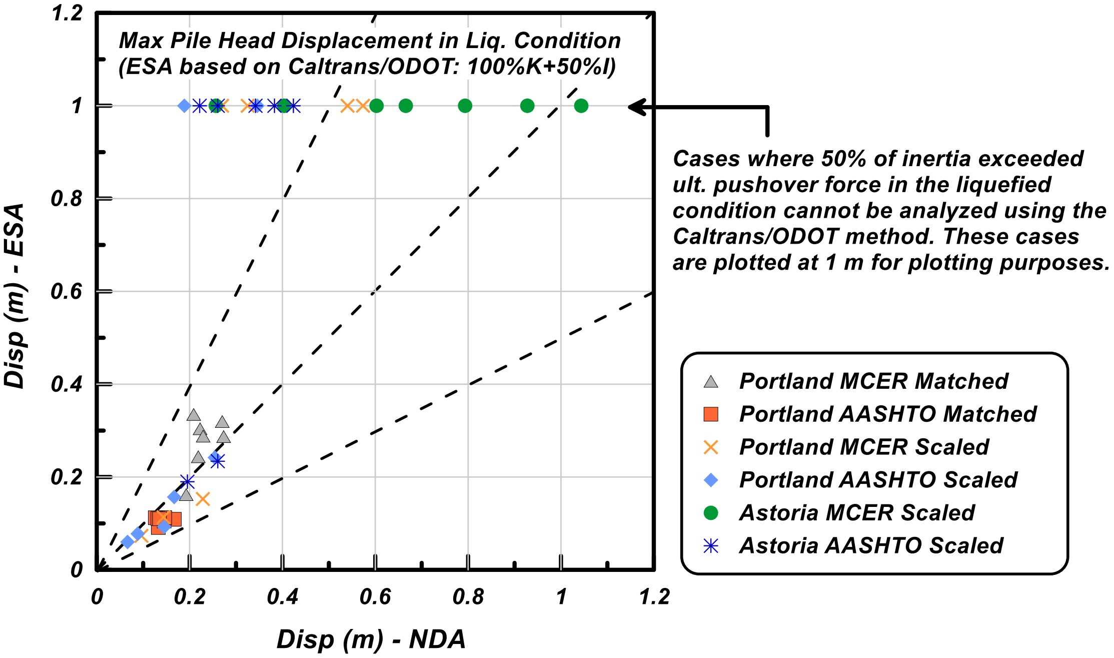

Figure 5-5:Comparison of the maximum pile head displacement in liquefied condition estimated from the Caltrans/ODOT equivalent static analysis (ESA) method (100% kinematic + 50% inertia) with the results of nonlinear dynamic analysis (NDA)

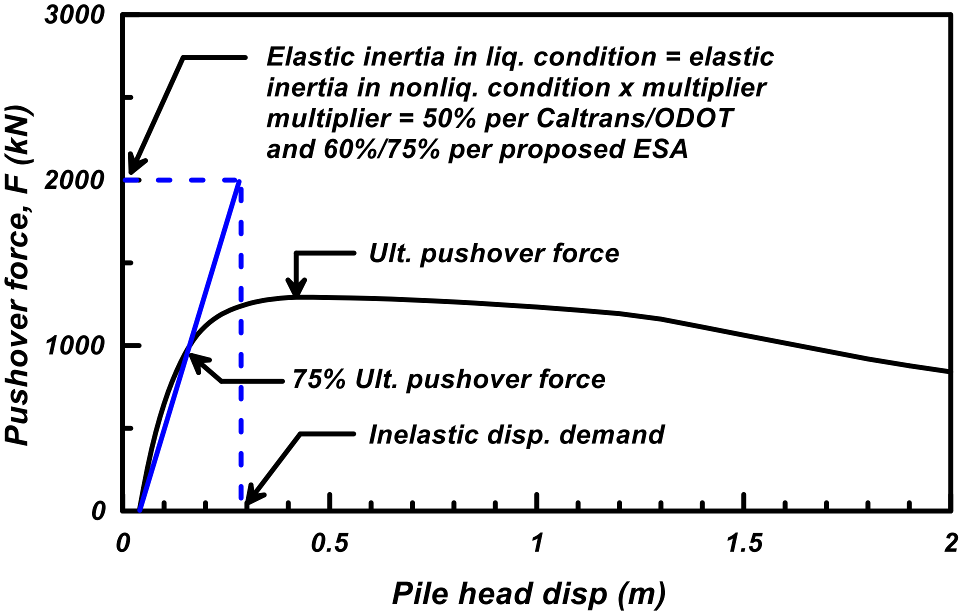

Figure 5-6: Estimating inelastic demands from liquefied pushover curve using the equal-displacement assumption for long-period structures

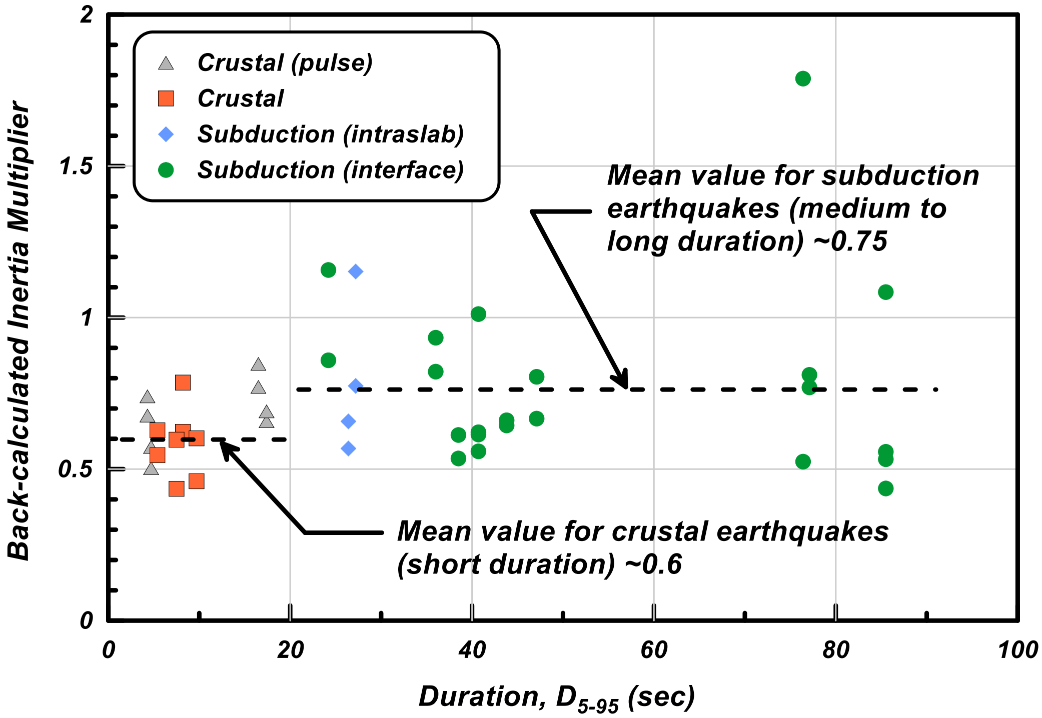

Figure 5-7: Dependence of the inertia multiplier (back-calculated from dynamic analyses) to ground motion duration ($D_{5\text{-}95}$) for subduction and shallow crustal earthquakes

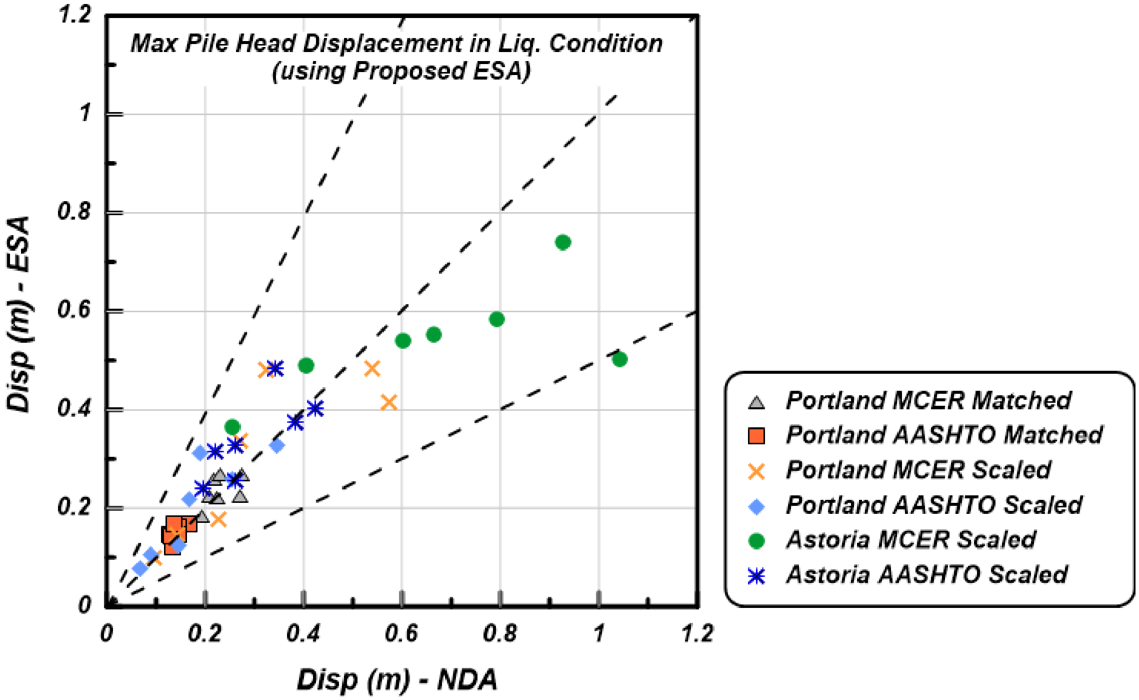

Figure 5-8: Comparison of the maximum pile head displacements estimated using the proposed equivalent static analysis (ESA) method with the nonlinear dynamic analysis (NDA) results.

6 CONCLUSIONS AND RECOMMENDATIONS FOR FUTURE WORK

6.1 Discussion

The back-calculated inertia multipliers that are shown in Figure 5-7 provide a quantifiable measure of how inelastic pile demands increase due to the combination of inertia and kinematics in long-duration earthquakes. Two cases are selected to illustrate the effects of motion duration on the inertia multiplier. Case A corresponds to 1992 Cape Mendocino EQ (CPM station) which is a crustal short-duration motion ($D_{5\text{-}95}$ = 5 sec). Case B corresponds to 2011 Tohoku EQ (MYGH06 station) which is a subduction long-duration motion ($D_{5\text{-}95}$ = 77 sec). Both motions were spectrally matched to MCER design spectra for the Portland site. Therefore, both motions have similar PGA (0.5 g) and similar spectral ordinates at the natural period of the structure (Sa(T =1.36 sec) = 0.28 g). As a result, both motions result in similar maximum inertial load (2260 kN in MYGH06 and 2350 kN in CPM) and similar maximum pile head displacements in the nonliquefied NDA (0.15 m in MYGH06 and 0.19 m in CPM). However, the maximum pile head displacement in liquefied conditions is larger in the case of MYGH06 (0.27 m) compared to CPM (0.22 m). This larger pile head displacement results in a larger inertia multiplier for MYGH06 compared to CPM

(80% vs. 60%, back-calculated from Equation 1 using ΔLS = 0.04 m). The larger inertia multiplier implies that some constructive interaction between inertial and kinematic loads increases pile demands, specifically in long-duration motions. This effect is shown in Figure 6-1 by comparing the moment-curvature response in the plastic hinge for CPM motion (short duration) and MYGH06 (long duration). This figure shows how the incremental yielding in pile amplifies inelastic demands during long-duration motions. The increased inelastic demand is accounted for in the proposed ESA method by increasing the inertia multiplier to 75%.

6.2 Conclusion

Effective-stress, nonlinear dynamic analyses (NDA) were performed for a large-diameter (2 meters) RC shaft in sloped liquefying ground. The NDA were performed for a suite of subduction and crustal earthquake motions covering a wide range of durations to evaluate how inertia and lateral-spreading loads combine in short vs. long duration earthquakes. The dynamic analyses included both nonliquefied conditions (without pore-water-pressure generation) and liquefied conditions (with pore-water-pressure generation and liquefaction-induced lateral spreading). The NDA results were used to evaluate current equivalent static analysis (ESA) method of Caltrans/ODOT and develop a new ESA method.

The NDA results showed that pile demands increase in liquefied conditions compared to nonliquefied conditions due to the interaction of inertia (from superstructure) and kinematics (from liquefaction-induced lateral spreading). Comparing pile demands estimated from ESA recommended by Caltrans/ODOT with those computed from NDA showed that the guidelines by Caltrans/ODOT (100% kinematic combined with 50% inertia) slightly underestimates demands for piles that remain elastic (where 50% of inertia is less than the ultimate pushover force in liquefied conditions). A new ESA method was developed to extend the application of the Caltrans/ODOT method to inelastic piles. The inertia multiplier was back-calculated from the NDA results and new multipliers were proposed: 100% Kinematic + 60% Inertia for crustal earthquakes and 100% Kinematic + 75% Inertia for subduction earthquakes. The proposed ESA compared reasonably well against the NDA results for elastic piles. It also made possible to estimate demands in piles that performed well in the dynamic analyses but could not be analyzed using Caltrans/ODOT method (i.e. inelastic piles that remained below F_{ult} on the liquefied pushover curve). However, it was observed that the pile demands became unpredictable for cases where the pile head displacement exceeded the displacement corresponding to the ultimate pushover force in liquefied conditions. Nonlinear dynamic analysis is required for these cases to adequately estimate pile demands.

6.3 Future Research

The relatively small sample of ground motions used in this study make it difficult to provide a statistically meaningful assessment regarding the performance of the revised ESA method. For this reason, a more robust set of ground motions, both short duration and long duration, should be gathered and analyzed to validate the trends observed in this study. Furthermore, the use of spectrally matched or spectrally-compatible ground motions may be preferred to better isolate the effects of strong-motion duration.

The design method proposed in this paper is based on a single soil/pile model and does not address the sensitivity of the results to the assumed pile type and soil stratigraphy. The applicability of the method could be widened based on the results of parametric analyses that consider various cases of pile geometry, superstructure mass, and soil stratigraphy covering a range of possible scenarios encountered in practice. The pile head fixity can also be varied as part of the parametric study to determine whether the pile demands can be enveloped by considering both, freed and fixed-head conditions.

6.4 Figures and Tables

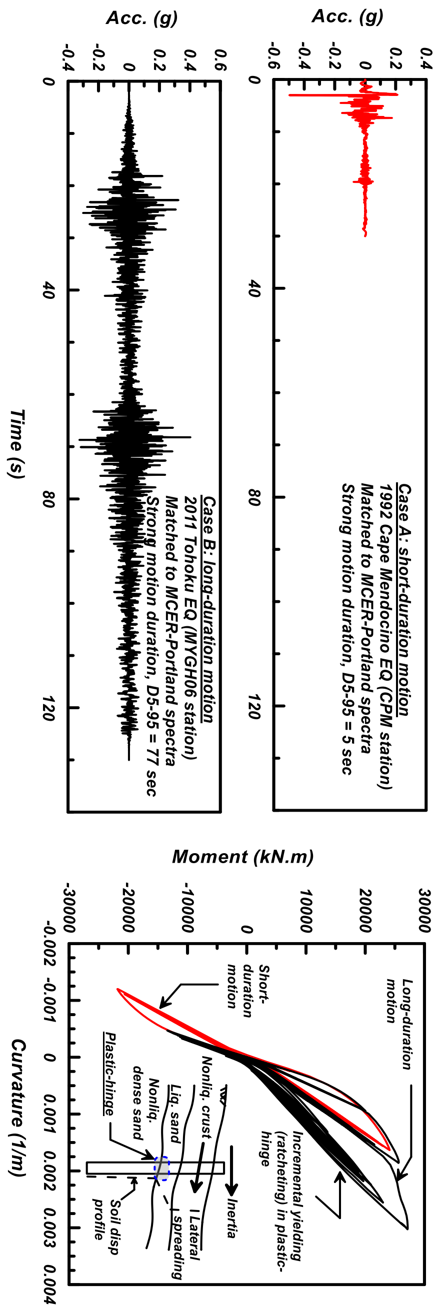

Figure 6-1: Comparison of moment-curvature behavior in the plastic hinge for a long and short duration motions both spectrally matched to the MCER design spectrum developed for the Portland site

7 REFERENCES

AASHTO (2014). “Guide Specifications for LRFD Seismic Bridge Design.” Second Edition with 2014 Interim, AASHTO, Washington, D.C.Al Atik L.., Abrahamson N.A. (2010) An Improved Method for Nonstationary Spectral Matching. Earthquake Spectra: August 2010, Vol. 26, No. 3, pp. 601-617.

American Petroleum Institute (2000). “Recommended Practice for Planning, Designing, and Constructing Fixed Offshore Platforms.” API recommended practice 2A-WSD (RP 2AWSD), 21st Edition, API.

ASCE/COPRI 61-14 (2014). “Seismic Design of Piers and Wharves, prepared by the ASCE Standards Comm. on Seismic Design of Piers and Wharves.” ASCE, Reston, VA.

Ashford, S.A., Scott, M.H., and Rayamajhi, D., (2012). “Reducing Seismic Risk to Highway Mobility: Assessment and Design Examples for Pile Foundations Affected by Lateral Spreading”, ODOT Report.

Boulanger, R.W., Chang, D., Brandenberg, S.J., Armstrong, R.J., and Kutter, B.L. (2007). “Seismic design of pile foundations for liquefaction effects.” 4th International Conference on Earthquake Geotechnical Engineering, The Netherlands, 277-302.

Bozorgnia, Y., Abrahamson, N. A., Atik, L. A., Ancheta, T. D., Atkinson, G. M., Baker, J. W., ... & Darragh, R. (2014). NGA-West2 research project. Earthquake Spectra, 30(3), 973-987.

Brandenberg, S.J., Zhao, M., Boulanger, R.W., and Wilson, D.W. (2013). “p-y Plasticity Model for Nonlinear Dynamic Analysis of Piles in Liquefiable Soil.” ASCE JGGE, 139(8), 1262-1274.

California Department of Transportation (Caltrans) (2012). “Guidelines for Foundation Loading and Deformation Due to Liquefaction Induced Lateral Spreading.” Sacramento, CA.

Cascadia Region Earthquake Workgroup (CREW) (2013). “Cascadia Subduction Zone Earthquakes: A Magnitude 9.0 Earthquake.” <http://www.crew.org/sites/default/files/cascadia_subduction_scenario_2013.pdf > (July 2,2017)

Franke, K. W., & Rollins, K. M. (2017).”Lateral Spread Displacement and Bridge Foundation Case Histories from the 1991 Magnitude 7.6 Earthquake near Limón, Costa Rica”. Journal of Geotechnical and Geoenvironmental Engineering, 143(6), 05017002

Fugro Consultants Inc., (2016), EZ-FRISK, “Software for Earthquake Ground Motion Estimation., User’s Manual

Idriss, I. M., and Boulanger, R. W., (2008). Soil liquefaction during earthquakes, Monograph MNO-12. Earthquake Engineering Research Institute, Oakland, CA, 261 pp.

Japanese Geotechnical Society (JGS), 1996. Special Issue on Geotechnical Aspects of the January 17, 1995, Hyogoken-Nambu Earthquake, Soils and Foundations, Tokyo.

Khosravifar, A., and Boulanger, R. W., (2010). Inelastic Response of Extended Pile Shafts in Laterally Spreading Ground during Earthquakes. Deep Foundation Institute J. 4, 2, 41-53.

Khosravifar, A., Boulanger, R.W., and Kunnath, S.K. (2014). “Effects of Liquefaction on Inelastic Demands of Bridge Pile Shafts.” Earthquake Spectra, 30 (4), pp, 1749-1773.

Makdisi, F., C.Y. Chang, Z. Wang and C. Mok (1991). Analysis of the Recorded Response of Lexington Dam During Various Levels of Ground Shaking. SMIP91 Seminar on Seismological and Engineering Implications of Recent Strong-Motion Data, p. 10-1 - 10-10.

Mazzoni, S., McKenna, F., Scott, M. H., and Fenves, G. L., (2009). Open system for earthquake engineering simulation user manual. University of California, Berkeley.

MCEER/ATC (2003) “Recommended LRFD Guidelines for the Seismic Design of Highway Bridges.” MCEER/ACT 49, Multidisciplinary Center for Earthquake Engineering/Applied Technology Council Joint Venture, University at Buffalo, Buffalo, NY.

McGann, C. R., Arduino, P., and Mackenzie-Helnwein, P., (2011). “Applicability of conventional p-y relations to the analysis of piles in laterally spreading soil.” J. Geotech. Geoenv. Eng. 137, 6, 557-567.

Mejia, L.H., and Dawson, E.M. (2006). “Earthquake Deconvolution for FLAC.” Proceedings of Fourth International FLAC Symposium on Numerical Modeling in Geomechanics, Madrid, Spain.

Niem, A.R., Niem, W.A. (2013). “Correlation of Exploration Wells Astoria Basin N.W. Oregon.” Oregon Department of Geology and Mineral Industries Oil and Gas Investigation (14).

Oregon Dept. of Transportation (2014). Geotechnical Design Manual. Tech. Services Branch, Salem, OR

Oregon Seismic Safety Policy Advisory Committee (OSSPAC) (2013) “The Oregon Resilience Plan Reducing Risk and Improving Recovery for the Next Cascadia Earthquake and Tsunami.” <http://www.oregon.gov/oem/Documents/Oregon_Resilience_Plan_Final.pdf> (July 1, 2017)

Petersen, M. D., Frankel, A.D., Harmsen, S.C., Mueller, C. S., Haller, K. M., Wheeler, R.L., Wesson, R.L., Zeng, Y., Boyd, O.S., Perkins, D.M., Luco, N., Field, E.H., Wills, C.J., and Rukstales, K.S.(2008) “Documentation for the 2008 Update of the United States National Seismic Hazard Maps: U.S. Geological Survey Open-File Report 2008–1128”, 61 p

Petersen, M.D., Moschetti, M.P., Powers, P.M., Mueller, C.S., Haller, K.M., Frankel, A.D., Zeng, Yuehua, Rezaeian, Sanaz, Harmsen, S.C., Boyd, O.S., Field, Ned, Chen, Rui, Rukstales, K.S., Luco, Nico, Wheeler, R.L., Williams, R.A., and Olsen, A.H., (2014) “Documentation for the 2014 update of the United States national seismic hazard maps: U.S. Geological Survey Open-File Report 2014–1091”, 243 p.,

Tokimatsu, K., Suzuki, H., Sato, M. (2005). “Effects of inertial and kinematic interaction on seismic behavior of pile with embedded foundation.” Soil Dyn. Earthquake Eng. 25, 753-762.

United States Census Bureau (2010) “Oregon:2010 Population and Housing Unit Counts.”<https://www.census.gov/prod/cen2010/cph-2-39.pdf> (July 2, 2017)

Washington Dept. of Transportation (WSDOT) (2015). “Geotech Design Manual.” M 46-03.11, May 2015

Wong, I. G., & Bott, J. D. (1995). A look back at Oregon’s earthquake history, 1841–1994. Oregon Geology, 57(6), 125-139.

Wong, I. G., Hemphill-Haley, M. A., Liberty, L. M., & Madin, I. P. (2001). The Portland Hills fault: an earthquake generator or just another old fault. Oregon Geology, 63(2), 39-50.

Yang, Z., Elgamal, A., and Parra, E., (2003). “Computational model for cyclic mobility and associated shear deformation.” J. Geotech. Geoenviron. Eng, 129, 12, 1119-1127.

Yang, Z., and Jeremic, B., 2002. Numerical analysis of pile behavior under lateral loads in layered elastic-plastic soils, Int. J. of Analytical Methods in Geomechanics 26, 1385–1406.